Epitaxial lead-free oxide layers for electrocaloric studies

Dissertation

submitted for the degree of:

Doktor der Ingenieurwissenschaften - Dr.-Ing.

presented to the

Faculty of Mechanical Science and Engineering at

the Technische Universität Dresden

by

Bruno Martins Magalhães, M.Sc.

born on 29.01.1990 in Lausanne, Switzerland

Submitted on 31.05.2022

Defended on 20.01.2023

First reviewer:

Prof. Dr. Kornelius Nielsch

Technische Universität Dresden

Second reviewer:

Prof. Dr. Kathrin Dörr

Martin-Luther-Universität Halle-Wittenberg

Third reviewer:

Prof. Dr. Alexander Michaelis

Technische Universität Dresden

Abstract

Solid-state cooling based on the electrocaloric effect might be a promising alternative to vapor-compressed refrigeration, not only for its increased efficiency but also for its role in preventing the emission of hazardous gases. The electrocaloric effect (ECE) refers to the reversible adiabatic temperature change that occurs in polar materials when an external electric field is applied or varied. In ferroelectric materials, the ECE is particularly pronounced at the transition temperature between the ferroelectric and paraelectric phases. It was shown recently that ferroelectric thin films in general exhibit excellent electrocaloric properties due to their capacity to withstand high electric fields, which typically results in an increase in the adiabatic temperature change. Therefore, the major aim of this thesis was to study environmentally friendly lead-free compounds for their feasibility as electrocaloric active layers in epitaxial film architectures prepared by pulsed laser deposition.

Reports in literature on bulk materials suggest that $Na_{0.5}Bi_{0.5}TiO_3$ (NBTO) compounds may be suitable for electrocaloric cooling. Therefore, the growth of epitaxial NBTO-based thin films was studied, which helps to study the correlation between composition, microstructure, and functional properties of this material. Epitaxial films were deposited on different single crystalline substrates applying a thin epitaxial $La_{0.5}Sr_{0.5}CoO_3$ layer as the bottom electrode for subsequent electric measurements. Structural investigation by X-ray diffraction revealed an undisturbed epitaxial growth on $LaAlO_3$, whereas a significantly smaller temperature window for epitaxy was found on $YAlO_3$. The differences might be explained by the lattice misfit resulting in a higher defect density of the intermediate buffer layer on $YAlO_3$. For all samples, a columnar structure with additional pores was found leading to substantial surface roughness. Dielectric measurements revealed significantly decreased permittivity values and increased losses at elevated temperatures if compared to bulk samples. While polarization loops at -100 °C indicated a distinct ferroelectric behavior, ambient temperature data revealed significant resistive contributions due to high leakage currents. As

a result, it was not possible to determine the electrocaloric properties for all NBTO-based thin films deposited with the indirect method.

In the second part of the thesis, the correlation between structural properties and the electrocaloric effect was investigated in lead-free epitaxial $Ba_{1-x}Sr_xTiO_3$ (BSTO) thin films. Here, BSTO thin films with Sr contents ranging from $x = 0$ to $x = 0.3$ were deposited on $SrRuO_3$ buffered $SrTiO_3$ single crystalline substrates. X-ray diffraction analysis verified a pure epitaxial growth for all Sr concentrations and film thicknesses indicating a larger tetragonal distortion if compared to the bulk material. Dense layers with a low surface roughness were found in microstructural studies. Temperature and frequency-dependent dielectric measurements indicate a diffuse phase transition for all samples, where thicker films showed larger permittivity values. The temperature of maximum permittivity decreases as Sr concentration increases. Polarization curves demonstrate a relaxor-like behavior, particularly above room-temperature. The adiabatic temperature change due to the ECE was determined with the indirect method showing $|\Delta T|$ values of up to 2.9 K for an electric field change of 750 kV cm^{-1}.

Kurzfassung

Festkörper-basierte Kühlprozesse basierend auf dem elektrokalorischen Effektes sind auf Grund der höheren Effizienz und der Vermeidung umweltschädlicher Prozessgase eine vielversprechende Alternative zu klassischen Kompressionskältemaschinen . Der elektrokalorische Effekt ist dabei eine reversible adiabatische Temperaturänderung, die in polaren Materialien auftritt, wenn ein äußeres elektrisches Feld angelegt und geändert wird. In ferroelektrischen Materialien ist dieser Effekt in der Nähe der Übergangstemperatur zwischen ferro- und paraelektrischer Phase besonders ausgeprägt. In den letzten Jahren wurde dabei gezeigt, dass ferroelektrische Dünnschichten sehr gute elektrokalorische Eigenschaften aufweisen, da hohe elektrische Feldern angelegt werden können, was in der Regel zu einem Anstieg der adiabatischen Temperaturänderung führt. Zentrales Ziel dieser Arbeit war es deshalb, umweltfreundliche Bleifreie Materialien hinsichtlich ihrer Eignung als elektrokalorisch aktive Schicht in epitaktischen Schichtarchitekturen zu untersuchen, die durch gepulste Laserdeposition hergestellt werden.

Ergebnisse an Massivmaterialien deuten darauf hin, dass $Na_{0.5}Bi_{0.5}TiO_3$ (NBTO)-Verbindungen für die elektrokalorische Kühlung geeignet sein könnten. Deshalb wurde das epitaktische Wachstum von NBTO-Dünnschichten untersucht, um eine mögliche Korrelation zwischen Zusammensetzung, Mikrostruktur und funktionellen Eigenschaften herzustellen. Die epitaktischen Schichten wurden auf unterschiedlichen einkristallinen Substraten hergestellt, wobei ein dünner epitaktischer $La_{0.5}Sr_{0.5}CoO_3$ Puffer verwendet wurde, der später als untere Elektrode für elektrische Messungen diente. Strukturuntersuchung mittels Röntgenbeugung zeigten auf $LaAlO_3$ Substraten ein ungestörtes epitaktisches Wachstum, während auf $YAlO_3$ ein deutlich kleineres Temperaturfenster für Epitaxie gefunden wurde. Dieser Unterschied kann durch die größere Gitterfehlpassung zum $YAlO_3$ erklärt werden, die zu einer Akkumulation von Defekten in der Pufferschicht führt. Für alle Schichten wurde eine kolumnare Struktur und eine klar erkennbare Porösität beobachtet, die zu einer deutlichen Oberflächenrauheit führten. Im Vergleich zu Massivproben zeigten dielektrische Messungen oberhalb von Raumtemperatur geringere

Dielektrizitätskonstanten und höhere Verluste. Mit Polarisationsmessungen bei -100 °C konnte ein klares ferroelektrisches Verhalten nachgewiesen werden, während höhere Leckströme und ein daraus resultierendes resistives Verhalten bei Umgebungstemperatur beobachtet wurden. Aus diesem Grund war es nicht möglich, die elektrokalorischen Eigenschaften von NBTO-basierten Dünnschichten mit Hilfe der indirekten Methode zu bestimmen.

Im zweiten Teil der Arbeit wurde der Zusammenhang zwischen den strukturellen Eigenschaften und dem elektrokalorischen Effekt an bleifreien epitaktischen $Ba_{1-x}Sr_xTiO_3$ (BSTO)-Dünnschichten untersucht. Dabei wurden BSTO-Schichten mit Sr-Gehalten von $x = 0$ bis $x = 0,3$ auf $SrRuO_3$ gepufferten $SrTiO_3$ Einkristallsubstraten abgeschieden. Die Röntgenstrukturanalyse bestätigte das epitaktische Wachstum für alle Sr-Konzentrationen und Schichtdicken, wobei eine zusätzliche tetragonale Verzerrung im Vergleich zum Massivmaterial beobachtet wurde. Mikrostrukturelle Untersuchungen zeigten dichte Schichten mit einer geringen Oberflächenrauheit. Temperatur- und frequenzabhängige Messungen der dielektrischen Eigenschaften weisen auf einen diffusen Phasenübergang hin, wobei dickere Schichten höhere Permittivitätswerte aufwiesen. Die Temperatur der maximalen Permittivität nimmt dabei mit steigender Sr-Konzentration ab. Polarisationsmessungen zeigten insbesondere oberhalb von Raumtemperatur ein relaxorähnliches Verhalten. Die adiabatische Temperaturänderung $|\Delta T|$ durch den ECE wurde indirekt bestimmt und erreichte Werte von 2.9 K bei einer Feldänderung von 750 kV cm^{-1}.

Contents

vi

Table of Figures

List of Tables

List of abbreviations

AFM	Atomic force microscopy
bCE	Barocaloric effect
BTO	$BaTiO_3$
CP	Critical point
eCE	Elastocaloric effect
ECE	Electrocaloric effect
FIB	Focused ion beam
LAO	$LaAlO_3$
LSCO	$La_{0.5}Sr_{0.5}CoO_3$
mCE	Mechanocaloric effect
MCE	Magnetocaloric effect
MPB	Morphotropic phase boundary
NBTO	$Na_{0.5}Bi_{0.5}TiO_3$
NBSBTO	$Na_{0.38}Bi_{0.38}Sr_{0.18}Ba_{0.06}TiO_3$
NBTO 5/10/5	$Na_{0.5}Bi_{0.5}TiO_3$ + 5 mol % Bi_2O_3 + 10 mol % Na_2CO_3 + 5 mol % Mn_2O_3
NBSBTO 5/10	$Na_{0.38}Bi_{0.38}Sr_{0.18}Ba_{0.06}TiO_3$ + 5 mol % Bi_2O_3 + 10 mol % Na_2Co_3
PLD	Pulsed laser deposition
PMN-PT	$Pb(Mg_{1/3}Nb_{2/3})O_3$-$PbTiO_3$
PNR	Polar nano regions
RSM	Reciprocal space map
SRO	$SrRuO_3$
STO	$SrTiO_3$

TB	Measurement configuration between upper and lower electrode (top-bottom)
TT	Measurement configuration between top and top electrode (top-top)
XRD	X-ray diffraction
YAO	$YAlO_3$

List of Symbols

A	Area of the top electrode
a, c	Lattice parameters
C	Curie constant
C_{PC}	Capacity of plate capacitor
c	Specific heat
d_{FL}	Layer thickness of ferroelectric layer
E	Electric field strength
E_C	Coercive field
f_{DEP}	Deposition frequency
P	Polarization
P_R	Remanent polarization
P_S	Saturation polarization
pO_2	Oxygen background pressure
Q	Isothermal heat
Q_x, Q_z	Coordinates in reciprocal space mapping
R_p	Parallel resistance
S	Entropy
T	Temperature
T_B	Burns temperature
T_C	Curie temperature
T_{CW}	Curie-Weiss temperature
T_d	Depolarization temperature

T_{DEP} Deposition temperature

T_f Freezing temperature

T_m Temperature of maximum permittivity

V Voltage

ω Laser energy density

ΔE Change in electrical field strength

ΔQ Isothermal heat change

$|\Delta S|$ Isothermal change in entropy

$|\Delta T|$ Adiabatic temperature change

$|\Delta T/\Delta E|$ Electrocaloric strength

ε Permittivity

ε_0 Permittivity in vacuum

ε_r Relative permittivity

ρ Specific heat capacity

ψ Tilt angle in the texture analysis

1. Introduction

Global warming is one of the most pressing issues in the twenty-first century with the year 2020 being the second warmest year on record [1]. This is linked to higher levels of greenhouse gases in the atmosphere, such as carbon dioxide (CO_2) and methane (CH_4) [2-5]. Refrigeration technology, which includes all types of cooling systems, air conditioning systems, and heat pumps, represents almost 20 % of world electricity consumption [6] and accounts for about 8 % of worldwide greenhouse gas emissions [7]. These emissions are caused by the direct release of greenhouse gases, mainly fluorinated substances, which are employed as refrigerants and, in some situations, have a thousand-fold larger global warming effect than CO_2 [8]. Significant effort has been invested in creating novel refrigeration processes in attempt to extend the advantages of artificial cooling while also limiting, eliminating, and hopefully reversing these environmentally devastating outcomes. Liquids and solids are excellent candidates for novel refrigeration techniques not only because their higher mass density results in a higher energy density, but also because they do not emit hazardous gases.

Numerous industries regard innovative cooling methods as a critical component of their system design. A case in point is superconductor-based technology, which necessitates extremely precise cryogenic temperature control. On the opposite end of the spectrum are the hybrid and electric vehicle industry, which is harmed by the excessive heat created by a vehicle's mechanical and electrical systems, hence limiting the electrical systems' efficiency, dependability, and cost. Another illustration is the microelectronics industry. Electronic miniaturization has garnered considerable attention in recent years as a result of the rising need for small, complicated, and lightweight devices that incorporate a significant number of electronic components, i.e., integrated circuits. Demands from throughout the industry for more efficient, versatile, and environmentally friendly refrigeration have pushed solid-state refrigerators to the forefront as possible solutions for a new generation of refrigeration systems [9].

Caloric cooling is a new type of solid-state cooling that has the potential to be a viable alternative to traditional compression refrigeration [9-11]. Caloric effects are described thermodynamically in terms of the fundamental Carnot cycle as the isothermal entropy changes $|\Delta S|$ and adiabatic temperature changes $|\Delta T|$ that a material endures in response to changes in an external field. Indeed, solid-state caloric effects are fundamentally similar to vapor compression: To exchange a large amount of heat, caloric effects are typically sought near first-order phase transitions [10-12], where the transition is driven cyclically forward and backward by suitable external fields such as magnetic, electric, or mechanical, resulting in magnetocaloric, electrocaloric (ECE), elastocaloric, and barocaloric effects [13, 14]. The ECE, like other caloric phenomena, happens as a result of a rearrangement of the inner structure of electrocaloric materials; particularly, if the transformation is adiabatic, the material's entropy decreases, resulting in an increase in the material's temperature [15]. The electrocaloric effect, first observed by Kobeko and Kurtschatov in 1930 in Rochelle salt [16], is a reversible phenomenon. Consequently, the opposite behavior (a decrease in the material's temperature) occurs when the electric field is removed adiabatically. The cyclic application and removal of the electric field, alternating with heat transfer to or from the electrocaloric material, provides life to the thermodynamic cycles at the base of electrocaloric cooling. Electrocaloric refrigeration is a relatively new technique among the caloric ones, having garnered significant interest from the scientific community only in the last decade, particularly for applications at room-temperature [15], owing to its potential and the environmentally friendly nature of its refrigerants [17]. The tipping point was the finding of the enormous electrocaloric effect in $PbZr_{0.95}Ti_{0.05}O_3$ [18], which resulted in a significantly higher adiabatic temperature shift than the ECE observed before in other materials [9].

Due to the toxicity of lead-containing materials, researchers have studied new eco-friendly materials for electrocaloric cooling [19]. Lead-free materials, such as $BaTiO_3$ (BTO) [20, 21], $Na_{0.5}Bi_{0.5}TiO_3$ (NBTO) [22], $Ba_{1-x}Sr_xTiO_3$ (BSTO) [23], $SrBi_2Ta_2O_9$ [24], P(VDF-TrFE) [25], and P(VDF-TrFE-CFE) [26], among others are being investigated for use as lead-free alternatives.

2

The present work utilizes NBTO and BSTO thin films to further examine the material system's promising features and to obtain a deeper knowledge of the underlying physical processes, which is critical for the future development of electrocaloric materials. Epitaxial layer growth is used to achieve a well-defined structure and hence a better understanding of the link between microstructure, ferroelectric, and electrocaloric characteristics.

Pulsed laser deposition has been established for the fabrication of epitaxial thin layers, as this approach permits stoichiometric layer development and is characterized by a fairly simple test setup. The difficulty in the deposition of oxide thin layers is to establish process parameters in such a manner that the development of the required perovskite structure is not accompanied by secondary phase growth. Chapter 3 of this dissertation describes the experimental setup for the deposition and the study methods utilized to characterize the deposited thin films.

The impact of deposition settings and composition on the structural characteristics of NBTO-based thin films are discussed in Chapter 4. The growth conditions for epitaxial growth were improved, and the resultant thin films were characterized using a variety of methods. The electrical properties of materials generated using optimal deposition conditions are then tested, and their usefulness for ECE is concluded.

Chapter 5 discusses the effect of the composition of BSTO-based thin films on their structural and electrical characteristics. As with Chapter 4, the produced thin films were characterized using a variety of techniques and their electrical characteristics were determined. Based on the indirect method, the electrocaloric properties of this material are reported.

The findings of this work are summarized in Chapter 6.

The results of this research study have been published in two peer-reviewed scientific publications:

Magalhaes B., Engelhardt S., Molin C., Gebhardt S.E., Nielsch K., Hühne R. Structural and Electric Properties of Epitaxial $Na_{0.5}Bi_{0.5}TiO_3$-Based Thin Films. *Coatings*. 2021;11(6):651.

Magalhaes B., Engelhardt S., Molin C., Gebhardt S.E., Nielsch K., Hühne R. Electrocaloric temperature changes in epitaxial $Ba_{1-x}Sr_xTiO_3$ films. *Journal of Alloys and Compounds*. 2022;891:162041.

2. Theoretical background

This chapter discusses the theoretical foundations of the electrocaloric effect and the electrocaloric cooling cycle with its key aspects. Additionally, it analyzes relevant contributions to the field of solid-state cooling, examines the electrocaloric materials and their properties, and acknowledges the ongoing research on the electrocaloric effect.

2.1. Electrocaloric effect

The electrocaloric effect is the change in isothermal entropy $|\Delta S|$ and adiabatic temperature $|\Delta T|$ that occurs when a polar material is exposed to an external electric field, E [9, 11, 12, 27]. This effect may be demonstrated experimentally, for example, by doing a direct temperature measurement in which an electrical voltage, V, is applied as a function of time in a capacitor-like setup, generating an electrical field in the material. Figure 2.1 (a) shows a schematic representation of an ECE profile as a function of time (adapted from [11]), and (b) illustrates a direct measurement on a multilayer capacitor made of $BaTiO_3$ using a scanning thermal microscope [28].
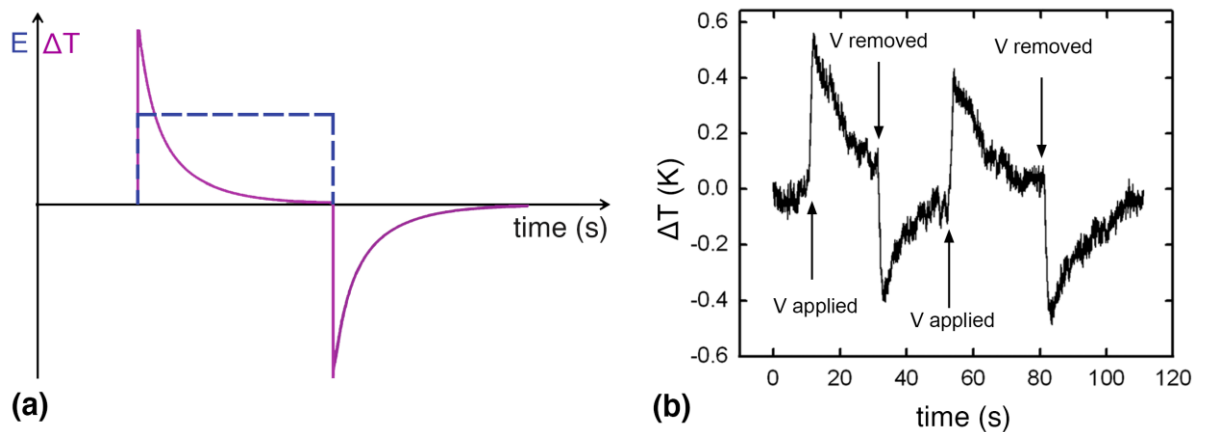
Figure 2.1 - Direct measurement of the ECE: a) Schematic representation of an ECE profile as a function of time measured directly under near adiabatic conditions (adapted from [11]); (b) Adiabatic temperature change $|\Delta T|$ of a $BaTiO_3$-based ceramic multilayer chip capacitor using a scanning thermal microscope [28].

When an electrical voltage is applied, the sample's temperature instantly rises, and when the voltage is withdrawn, the sample rapidly cools. This phenomenon occurs as a result of changes in the system's entropy produced by the external electric field. The starting temperature is reset after a few seconds due to heat exchange with the surroundings. A system's entropy includes contributions from polar and thermal subsystems. When an electric field is applied to a polarizable material, it causes the dipoles to align along the direction of the field, resulting in a decrease in dipole entropy. Because the change in total entropy must be zero under adiabatic circumstances, a rise in thermal entropy contribution occurs concurrently, increasing the lattice vibrations and the material's temperature. In the absence of an external field, the order of the dipoles diminishes, and the material's temperature falls.

Considered to be a highly viable option to vapor compression refrigeration and integrated circuit thermal management, the ECE has not always been viewed positively. It was observed for the first time in Rochelle Salt [12, 16] and quantified by Hautzenlaub in 1943 [29]. Although only a small electrocaloric temperature change was detected, these studies sparked research in the field of electrocaloric cooling, with a particular emphasis on the creation of new materials with increased cooling capability. In particular, Karchevskii discovered that the maximum electrocaloric performance occurs around phase transitions [30]. Ferroelectric materials were therefore identified as the best electrocaloric materials among all pyroelectric compounds. In 1977, Raghebaugh tested a cryogenic electrocaloric device [31], which was the very first concept for an electrocaloric refrigerator. It used $SrTiO_3$ ceramics with an electrocaloric temperature change of about 0.3 K. Meanwhile, the prospect of other electrocaloric cooling applications began to emerge, most notably for room-temperature operation. In this regard, an antiferroelectric $Pb(Zr_{0.455}Sn_{0.455}Ti_{0.09})O_3$ ceramic [32] has been proposed for room-temperature cooling applications due to its electrocaloric temperature change of ~ 1.6 K. Due to the fact that the phase transition temperature and electrocaloric impact of lead scandium tantalate, $PbSc_{0.5}Ta_{0.5}O_3$, could be modified by processing, the system gained substantial interest in room-temperature electrocaloric cooling. In a

multilayer structure, this system demonstrated a noteworthy electrocaloric temperature shift of ~ 2.4 K [33].

Nonetheless, the fact that bulk materials exhibit a negligible electrocaloric effect in comparison to their magnetic and thermoelectric counterparts resulted in only a small number of research groups devoting their efforts to the development of electrocaloric refrigeration, limiting their application to commercial refrigeration devices. This view of electrocaloric materials would shift dramatically in 2006 when a "giant" electrocaloric temperature change of ~ 12 K was indirectly measured in $PbZr_{0.95}Ti_{0.05}O_3$ thin films at the antiferroelectric-paraelectric phase transition at 225 °C [18]. The phenomenon was explained by the ability to apply a stronger electric field in thin films if compared to bulk. Two years later, a paper was published on the significant electrocaloric effect (up to 12 °C) seen at 70 °C in thin films of polyvinylidene fluoride-trifluoroethylene [P(VDF-TrFE)] [34]. These two publications laid the groundwork for renewed interest in electrocaloric research, resulting in a new and exciting age for electrocaloric cooling. Since 1970, a total of 5051 scientific publications [35] have been published. Nonetheless, approximately 92 % of these studies were published since 2000 (figure 2.2). The vast majority of these are concerned with the creation of novel ferroelectric thin films with enhanced electrocaloric effects at ambient temperature. Recent research has also shown the existence of a "negative electrocaloric effect," in which the sign of the temperature change is inverted. This was initially determined in an indirect manner using relaxor $Na_{0.5}Bi_{0.5}TiO_3$–$BaTiO_3$ ceramics. The phenomenon has been linked to the observation of a relaxor effect between the ferroelectric and antiferroelectric phases [36]. The coexistence of a positive and a negative electrocaloric action was later demonstrated in relaxor $70PbMg_{1/3}Nb_{2/3}O_3$-$30PbTiO_3$ single crystals across different phases of the phase diagram [37]. Negative electrocaloric effect is connected with free energy changes generated by an electric field, according to the paper above mentioned. Since then, avenues of study have been proposed to better understand the reversal sign of some materials' electrocaloric reaction and its potential for use in cooling devices [37, 38].
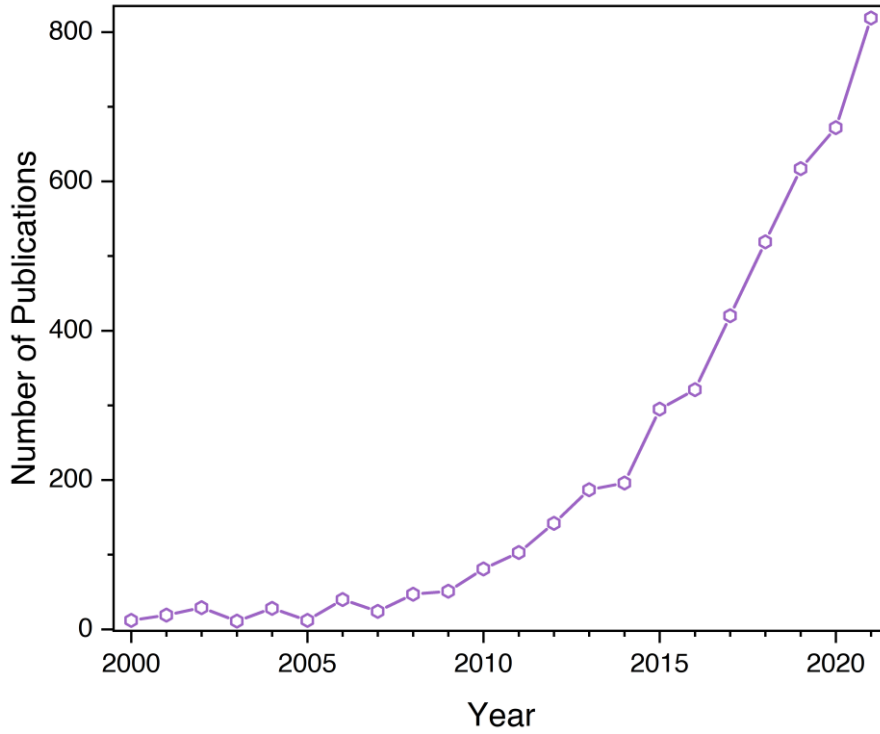
Figure 2.2 - Number of yearly publications on ECE from 2000 to 2021 [35].

Notwithstanding such rapid advancements in the field of electrocaloric materials, several concerns have been raised about the accuracy of electrocaloric effect measurements in thin films. ECE measurements in thin films are frequently determined from pyroelectric coefficient measurements rather than direct electrocaloric measurements, which introduces inaccuracies due to the assumptions used to relate the two effects. Additionally, direct measurements of the ECE are difficult due to the film's low heat capacity, deviations from adiabatic conditions, and heat transmission to temperature measuring instruments, substrates, and connections. However, a few attempts to directly quantify the electrocaloric effect in bulk and thin films were published [39], suggesting good agreement with indirect measurements.

2.2. Electrocaloric effect cooling cycle

The fundamental concept of an adiabatic cooling cycle is that entropy S, varies with both temperature T and applied electrical field E under adiabatic conditions. The application of an external electric field causes changes in the polarization of a dielectric material from a less ordered to a more ordered state

[40-42]. This results in a decrease in the entropy of the material and an increase in its temperature. As this process is reversible, the opposite happens when the electric field is removed. Entropy increases in this situation (due to the disordered structure of the dipoles in a dielectric substance) and the temperature of the material falls [12, 13, 15, 43]. A cooling cycle is generated by cyclically inducing this condition in a material by applying and removing an external electric field, including heat transfer to or from the system.

A number of publications describe the application of the ECE in a cooling circuit [6,10,11,19,31], which is schematically depicted in figure 2.3. Along with the Brayton cycle explained below, there are other variations, including Carnot, Ericsson, and Stirling cycles [44, 45].
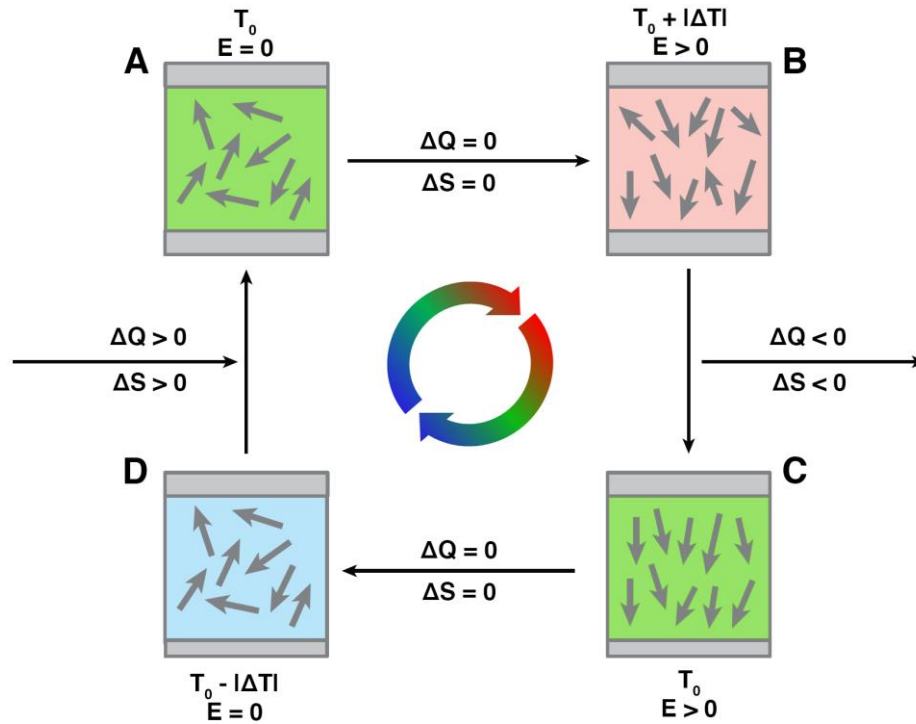
Figure 2.3 - Electrocaloric cooling cycle. Adapted from [12].

At the initial state (A), an external electric field (E) is applied to an electrocaloric material at T_0 under adiabatic conditions. This leads to state B, showing an improved alignment of dipoles and a subsequent decrease of the system entropy ($|\Delta S|$), which leads to an increase in the system temperature to $T_0 + |\Delta T|$ ($\Delta Q = 0$). From state B to state C, the heat is subsequentially transferred to a heat sink ($\Delta Q < 0$), further decreasing $|\Delta S|$ so that the system temperature

drops again to T_0. By removing the electric field under adiabatic conditions, the dipoles return to a more misaligned state increasing $|\Delta S|$, thus decreasing the temperature of the system to T_0 - $|\Delta T|$ (ΔQ = 0). The cooling cycle is complete when the system absorbs heat from a heat sink and returns to T_0 ($\Delta Q > 0$).

2.3. Comparison of different caloric effects

Caloric materials undergo reversible temperature changes, referred to as caloric effects when the applied driving field changes. The caloric effects are induced by electric, magnetic, and mechanical fields (electrocaloric (ECE), magnetocaloric (MCE), and mechanocaloric (mCE), respectively). These thermal changes are characterized as changes in adiabatic temperature $|\Delta T|$, isothermal entropy $|\Delta S|$, and isothermal heat Q. The first-order phase transition is widely recognized as the most advantageous for enhancing caloric response [46]. While the first-order transition produces larger caloric responses, it has significant disadvantages. Indeed, because the caloric peak around the first-order phase transition is sharp, it often results in a smaller working temperature range than the wide caloric peak associated with a second-order phase transition. Additionally, simultaneous hysteresis losses associated with the first-order-like character are harmful to caloric response, whereas there are no hysteresis losses connected with the second-order transition [10]. Table 2.1 shows some adiabatic temperature changes reported in the literature for the ECE, MCE, and mCE, which can be divided additionally into an elastocaloric effect (eCE) and a barocaloric effect (bCE).

Table 2.1 - Adiabatic $|\Delta S|$ and $|\Delta T|$ on different caloric effects.

Material	T (K)	$|\Delta S|$ (J K^{-1} kg^{-1})	$|\Delta T|$ (K)	Ref.
Magnetocaloric				
Gd	294	11	13	[47]
MnAs	317	34	13	[48]
$MnFeP_{0.45}As_{0.55}$	308	18	9.8	[49]
$Mn_{1.24}Fe_{0.71}P_{0.46}As_{0.54}$	320	12	3	[50]
$Ni_{52.6}Mn_{23.1}Ga_{24.3}$	300	18	12	[51]
Electrocaloric				
$Ba_{0.65}Sr_{0.35}Ti_{0.997}Mn_{0.003}O_3$	293	4.8	3.1	[52]
$PbZr_{0.95}Ti_{0.05}O_3$	499	8	12	[18]
0.93PMN-0.07PT	298	11	9	[53]
P(VDF-TrFE)	323	130	28	[54]
Elastocaloric				
$Fe_{68.8}Pd_{31.2}$	240	4.2	2	[55]
$Ni_{50.7}Ti_{49.3}$	295	8.5	11	[56]
$Cu_{64.6}Zn_{33.7}Sn_{1.7}$	296	15	12	[57]
$Cu_{69.6}Zn_{27.7}Sn_{2.7}$	308	22	14	[58]
NiTi	295	32	17	[59]
Barocaloric				
$Ni_{49.26}Mn_{36.08}In_{14.66}$	293	24	4.5	[60]
$Gd_5Si_2Ge_2$	270	11	1.1	[61]
$LaFe_{11.33}Co_{0.47}Si_{1.2}$	237	8.7	2.2	[62]

2.4. Electrocaloric materials

In an electrocaloric cooling cycle, the electrocaloric material is the key component since thermal energy is conducted in and out through the material, increasing and decreasing the temperature. Its cooling efficiency is dependent on its capacity to produce and reverse thermal energy. The functionality of an

electrocaloric refrigerator is governed by the properties of the electrocaloric materials. Based on their structural parameters, electrocaloric materials may be separated into three distinct groups: single crystals, polycrystalline ceramic materials, and polymers, which can be further divided based on their form and thickness (bulk, thick and thin films). The fundamental hurdle to the mechanical robustness of an electrocaloric material is its long-term exposure to relatively large changes in the electric field throughout the electrocaloric cooling cycle. This leads to high tensions in the interior structure, which produces an electromechanical breakdown.

Single crystals are materials with a homogeneous crystallographic structure (i.e. with the absence of grain boundaries). Due to the crystallographic structure, the mechanical stability depends on the magnitude of the lattice changes under an electric field. If the change in the lattice is significant, it may result in a fracture of the crystal structure. The opposite can be seen for PMN-PT, where the changes in the unit cell are small, enabling the use of higher electric fields.

Polycrystalline ceramics materials, with electrocaloric characteristics, are inorganic materials that might be structured in bulk, thick, and thin films. Even though the material's composition is the same, higher electric fields can be applied to a thick or thin film rather than the bulk form. This is related to the distance between electrodes, as larger voltages are required for bulk for the same magnitude of the electric field, increasing the risk of electrical breakdown.

The polymers demonstrating an electrocaloric effect are all based on the polyvinylidene-fluoride P(VDF) copolymers that, without the presence of an electric field, are crystallized in a non-polar state, which is connected to the lowest energy configuration. During the polymerization process, various flaws might be intentionally inserted in form of the following monomers: trifluororthylene (TrFE), vinylidene difluoride (VDF), and chlorofluoroethylene (CFE). Different electrocaloric answers might be detected, depending on the kind and the quantity of the defects induced, and the polymers are all organized in thick or thin layers.

One of the most critical factors to examine when developing electrocaloric materials is the link between the ECE and the change in entropy and polarization

due to the applied electric field. For a significant ECE, an external electric field must generate a substantial entropy shift related to the polarization change. These criteria are ideally met when the electrocaloric material is slightly above its ferroelectric transition, which allows for significant polarization changes. At the transition temperature, the ECE is greatest, and it progressively fades as the system enters the paraelectric state. Additionally, a strong ECE can be induced by structural rearrangements that result in substantial entropy shifts. As an example, Shebanovs et al. found that a substantial structural rearrangement occurs at the phase transition of $PbSc_{1/2}Ta_{1/2}O_3$ leading to a large change in entropy and cell volume. This resulted in a $|\Delta T|$ of 2.3 K, at 138 kV cm^{-1}, in the Curie temperature range of $T_C \pm 5$ K [33]. However, because cooling cycles cannot be established within such a small temperature range, more studies have focused on systems having a diffuse ferroelectric transition, such as disordered crystals and relaxor ferroelectrics. Thus, the selection of an electrocaloric material should take into account the properties of the material, such as structure, order of phase transition, dielectric properties, morphotropic phase boundaries, conductivity, and electric breakdown strength. Several of these properties are discussed in further detail below.

2.4.1.   Electrical and thermal hysteresis

The difference between a real electrocaloric refrigeration cycle from an ideal reversible Carnot cycle is due to multiple irreversible processes (thermal and electrical hysteresis) inherent in the electrocaloric material or thermodynamic device (losses during heat exchange). Thermal hysteresis is frequently found near a first-order phase transition in ferroelectric materials, which experiences a discontinuous polarization change. Simultaneously, the "glassy" nature of relaxors caused by polar nano-regions at low temperatures results in a non-ergodic response, which is manifested in the electrocaloric performance as a significant thermal hysteresis. Experiments on $93PbMg_{1/3}Nb_{2/3}O_3$-$7PbTiO_3$ thin films showed substantial thermal hysteresis. While the ECE cannot be precisely defined in the absence of thermal equilibrium, a $|\Delta T|$ can still be obtained [53].

Ferroelectric materials, on the other hand, display considerable electrical hysteresis. Electric hysteresis occurs when an applied electric field is varied.

When a sufficiently strong field is applied, the domains align with the field direction, resulting in polarization saturation. Certain domains revert to their original state when the field strength is decreased. Nonetheless, not all the domains are reverted, thus even at zero electrical field, the polarization remains higher than zero. This means that the electric field must be reversed to obtain zero polarization.

2.4.2.　Order of phase transition

All materials exhibiting an adiabatic temperature change based on the ECE may be classified according to the nature of the phase transition from the ferroelectric to the paraelectric state, i.e. as first or second-order phase transition. In both circumstances, the electrocaloric material undergoes a phase transition at the Curie temperature (T_C). It should be noted that T_C is the temperature at which the electrocaloric impact is most prominent in terms of isothermal entropy change and adiabatic temperature changes [15, 63].

If the polarization in dependence on temperature exhibits a discontinuity, the transition is defined as first-order (figure 2.4 (a)). Due to the coexistence of two phases in equilibrium and the resulting presence of latent heat, this type of transition is not immediate. Indeed, applying an electric field to a material with a first-order phase transition can cause the material to shift from paraelectric to ferroelectric behavior. Additionally, the existence of latent heat during the phase transition suggests that heat is dissipated throughout the polarization process, which affects the electrocaloric material's final temperature. As a result, thermal hysteresis exists. While first-order transition materials exhibit large adiabatic temperature fluctuations (around the Curie temperature), the ECE is localized in a narrow temperature range. The difference in polarization between the first-order phase transition and the second-order phase transition is shown in figure 2.4:

(a)   Temperature   (b)   Temperature
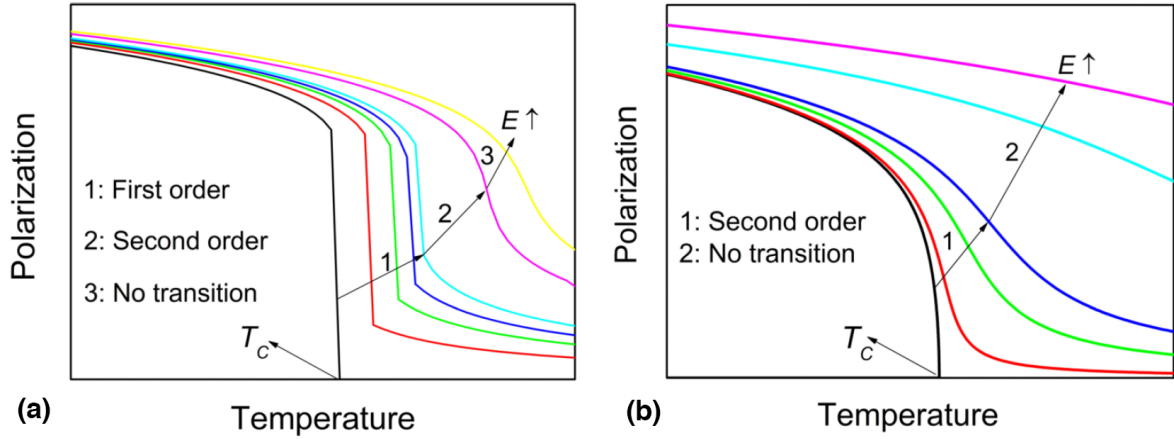
Figure 2.4 - Schematic dependence of the polarization on temperature for different applied electric fields for a: (a) first-order phase transition and (b) second-order phase transition [10].

In an electrocaloric material, a second-order phase transition occurs when the polarization changes continuously. Due to the continuity of the polarization and the absence of latent heat in the phase transition, second-order phase transition materials exhibit no thermal hysteresis. As a result, the adiabatic temperature change is close to instantaneous, and second-order phase transitions display no visible volume changes. On the other hand, the electrocaloric effect demonstrated by second-order materials has smaller peaks than those observed in first-order phase transitions (with an equivalent intensity change in the electric field), but it is more uniform throughout a wide temperature range. [18, 63].

2.4.3.   Morphotropic phase boundaries and critical points

One strategy to increase the ECE is to operate in areas of the phase diagram near critical points (CPs), which have lower energy barriers for switching between phases. Due to the coexistence of many polar phases near the CP, entropy is enhanced in this area [64]. This results in an increase in ECE [64], as Qian et al. demonstrated in Zr-doped $BaTiO_3$ close to the critical point [65]. Additionally, an invariant critical point has been demonstrated in materials having a morphotropic phase boundary (MPB), where the number of possible polar phases in the composition-temperature-electric field phase diagram is maximized. In a binary phase diagram, an MPB is a roughly perpendicular line

that divides two structural phases, such as tetragonal and rhombohedral. Some of the greatest ECE performances yet reported have been discovered in Pb-containing compounds that are near their MPB, such as PMN-30PT [39]. The ECE has also been observed for several lead-free materials with compositions close to the CP, such as Sr-doped NBTO-BTO [66, 67]. $Na_{0.5}Ba_{0.5}TiO_3$ (NBTO) has been reported to form solid solutions with a variety of ferroelectric materials, including BTO or $KNbO_3$, and many MPBs have been reported [68, 69]. The NBTO-BTO phase diagram indicates an MPB at 6 % BTO, with coexisting rhombohedral, tetragonal, and cubic phases [68]. Near this composition, NBTO-BTO exhibits the best electromechanical properties, including polarization and piezoelectric coefficient, with NBTO-06BTO being investigated for electrocaloric cooling [70].

2.4.4.　Dielectric strength

When the electric field strength is increased, the dipole entropy and the associated ECE temperature changes increase until they reach a saturation point. This condition exists when all dipoles along the field are perfectly aligned. Saturation is not possible in bulk materials because, below the required field strength, an electric breakdown occurs [71]. This suggests that the ECE temperature change is significantly limited by the dielectric strength of the material. This electromechanical breakdown results from defects in the structure [71, 72]. In general, the dielectric strength for layers increases with decreasing layer thickness [73]. If the dielectric strength could be greatly enhanced, a considerable rise in the ECE temperature change may be achieved.

2.4.5.　Conductivity

ECE materials must have an extremely low conductivity. Any increase in conductivity results in an increase in leakage current and hence in Joule heating. With rising field strength, the Joule heat effect becomes more prominent. Such a system gets warmer rather than cooler during a cooling cycle and with an alternating field, which may be rather evident in a cyclic fluctuation of the electric field. The Joule heating increases the apparent EC heating effect, which can be

quantified by comparing the observed ECE when the electric field is applied to the measured ECE when the electric field is withdrawn.

2.5. Anisotropy of the electrocaloric effect

According to Maxwell's laws, the ECE is a tensor property, which implies that it is orientation and direction-dependent [74]. Sebald et al. [75] conducted an experiment on PMN-PT 75/25 crystals cut in the [001], [110], and [111] directions. The electrocaloric effect is substantially stronger in the [111] crystal than in other crystals or a random-oriented grain ceramic sample. Marathe et al. [76] have shown that BTO exhibits significant anisotropy. For temperatures greater than the paraelectric-to-ferroelectric phase transition temperature, the temperature dependency is consistent across all field directions ([001], [011], and [111]). Nonetheless, its amplitude is direction-dependent and is greatest when electric fields are applied in the [001] direction. $|\Delta T|$ demonstrates a substantial difference for distinct field directions in the temperature zones around the ferroelectric-ferroelectric (orthorhombic and rhombohedral) transition. By taking anisotropy into account, the electrocaloric response may be optimized more effectively.

2.6. Ferroelectricity and ferroelectric materials

Pronounced electrocaloric effects were observed primarily in ferroelectric materials [9, 10, 12, 14, 22, 43, 77-79]. Ferroelectricity is a type of polar dielectric in which the polarization may be altered between two or more stable states when an electric field is applied [80, 81]. Valasek [82] discovered in 1920 that an electric field could be used to modify the polarization of Rochelle salt. Since then, it was increasingly understood that ferroelectrics represent a class of materials that exhibit not only the piezoelectric and pyroelectric effects but also other inherent features [80, 83-89]. The structural phase transition of the majority of ferroelectric materials occurs when they shift from a high-temperature paraelectric phase to a low-temperature ferroelectric phase.

The Curie temperature (T_C) is used to mark this transition. The transition may occur abruptly (first-order) or continually (second-order). Above T_C, the permittivity follows the Curie-Weiss law:

$$\varepsilon = \frac{C}{T - T_{CW}} \tag{2.1}$$

where T_{CW} is the Curie-Weiss temperature ($T_0 \leq T_C$) and C is the material-specific Curie constant. A number of ferroelectric materials, for example, barium titanate, $BaTiO_3$ (BTO), undergo multiple phase transitions into subsequent ferroelectric phases. Only the temperature at which the first ferroelectric phase transition occurs is referred to as the Curie temperature. The transition to the ferroelectric phase typically results in significant anomalies in the material's dielectric, elastic, and thermal properties [90], as well as in changes in the crystal unit cell, resulting in spontaneous polarization and entropy. The transition from the paraelectric to the ferroelectric phase results in a shift in the center of charge of different ion sublattices. The BTO structure's cubic and tetragonal unit cells are schematically depicted in figure 2.5. Ba^{2+} is located on the A-site at the corners of the cubic unit cell, while Ti^{4+} is located on the B-site in the unit cell center. The O^{2-} anions are arranged at the unit cell's face centers and form BO_6 octahedra [90]. The development of spontaneous polarization in BTO is attributed to a shift of the Ti^{4+} and O^{2-} ions relative to the Ba^{2+} ion at the origin. The resulting electric dipole moment is the spontaneous polarization, P_S. The onset of spontaneous polarization is accompanied by changes in the unit cell's size. The unit cell becomes tetragonally deformed during the transition from the paraelectric to the ferroelectric phase at $T_C = 130 \ °C$. The related P_S is perpendicular to the crystal's c-axis.
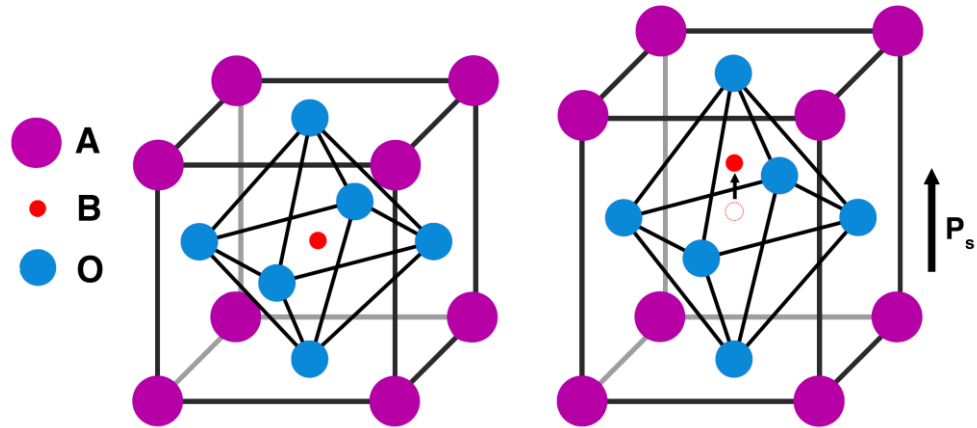
Figure 2.5 - Cubic and tetragonal unit cell of the perovskite structure.

Due to the symmetry of the cubic unit cells, the spontaneous polarization occurs with equal probability along any direction (including positive and negative) thus, in the tetragonal structure, there are six possible orientations for P_S. The directions in which the spontaneous polarization emerges are determined by the sample's electrostatic and mechanical boundary conditions [74, 89, 91]. Ferroelectric domains are portions of the crystal with evenly aligned P_S. The domain wall is the boundary between two domains. Matthias and Von Hippel [92] observed domains and domain walls, as well as the effect of temperature and electric fields on domain formation. They demonstrated that the domain structure is visible below the Curie temperature and that the domain size changes in response to external electric fields.

Ferroelectric domains limit the electrostatic energy associated with depolarizing fields and the elastic energy associated with mechanical restrictions to which the ferroelectric material is exposed throughout the paraelectric–ferroelectric phase transition [90, 91, 93, 94]. At T_C, the spontaneous polarization begins, and a surface charge is formed. This charge on the surface generates an electric field, referred to as a depolarizing field E_D, that is perpendicular to P_S. When there is an inhomogeneous distribution of spontaneous polarization or when the direction of polarization changes at grain boundaries, the formation of the depolarizing field occurs.

Domain boundaries can be moved in either a reversible or irreversible manner. Reversible domain wall displacements occur when domain walls move

around a local energy minimum, whereas irreversible domain wall displacements occur when domain walls leap between local energy minimum separated by a potential barrier [80]. When the applied electric field is small, the polarization increases linearly (figure 2.6 (a), (1 → 2). However, the applied electric field is not sufficiently strong to switch the domains that are not oriented along the electric field direction. With increasing electrical field, these domains begin to polarize along the field direction (2 → 3) and restore a linear change in polarization from 3 → 4. When the field strength decreases, certain domains switch back, although the polarization remains nonzero at zero field (4 → 5). To achieve a condition of zero polarization, the field must be reversed (5 → 6). Increases in the negative direction of the field will result in a new alignment of dipoles and saturation (6 → 7). After that, the field strength is lowered to zero and the cycle is completed. The remanent polarization, P_R, is the value of polarization at zero field (point 5).
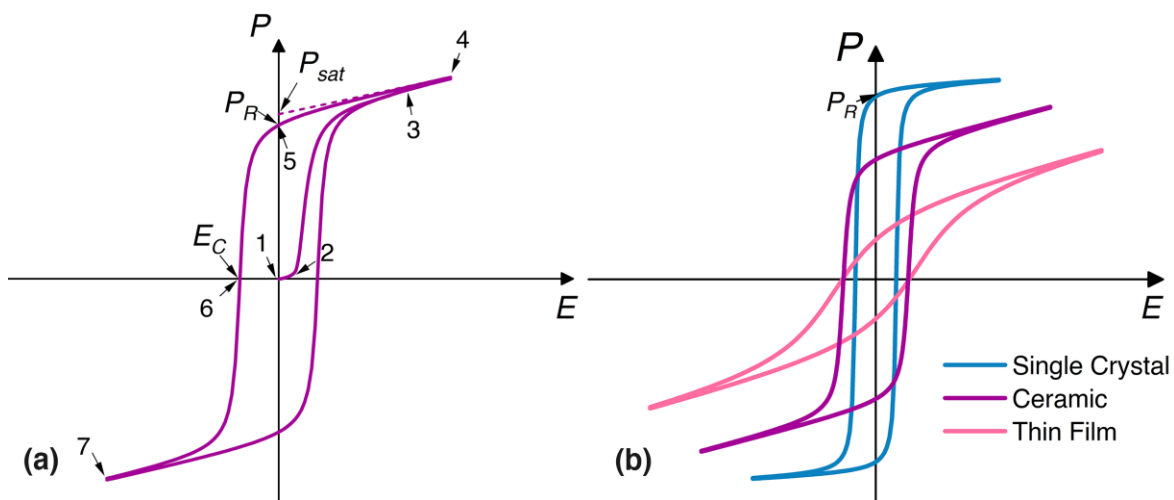
Figure 2.6 - Polarization-electric field hysteresis loop of a ferroelectric material: (a) Schematic ferroelectric $P(E)$ hysteresis loop; (b) Schematic $P(E)$ hysteresis loops for single crystals, ceramics, and thin films.

Some domain walls will back-switch when the field is lowered. As a result, with zero electric field (E), there is a non-zero macroscopic polarization, the remanent polarization (P_R). To restore the polarization to zero, an electric field in the opposite direction must be applied. The coercive field (E_C) is the field at which the polarization returns to zero (6). The observed hysteresis in the $P(E)$ curve is thus the result of reversible and irreversible domain wall displacement. The increased field strength in this direction results in the reorientation of the domains

and ultimately approaches saturation (7). The *P(E)* loop is completed by reducing the field strength to zero and then increasing it in the reverse direction.

Thin film ferroelectrics grown on substrates can impose significant stresses, meaning that the characteristics of ferroelectric thin films can frequently differ significantly from those of their bulk parent material. The hysteresis of the *P(E)* relationship in ferroelectrics shows that polarization is affected not only by the applied field but also by the history. As can be seen in figure 2.6 (b), the maximum feasible polarization for various ferroelectrics is greatest for single crystals and least for thin films. The evident discrepancy may be explained by the fact that in polycrystalline ceramics, intergranular interactions contribute to strain restrictions on polarization switching. Each polycrystalline ceramic is composed of several grains, each of which has a number of domains aligned in different crystal structure directions. As domains inside a grain attempt to switch orientations, they are restricted by neighboring grains with different orientations, i. e., due to the fact that the polarization vector is bound to the unit cell, it cannot be easily aligned in polycrystalline materials given the fact that rotation of the crystal structure in single grains is not possible. In thin films, the substrate interface further restricts the ferroelectric materials' poling ability because an applied electric field does not cause dimensional changes in a substrate [95]. Optimal *P(E)* hysteresis loops are symmetric with regard to their origin, which means that $|E_{C1}| = |E_{C2}|$ and $|P_{R1}| = |P_{R2}|$. Many factors can influence the coercive field, spontaneous and remanent polarization, and loop form, including the thickness of the film, the existence of charged defects, mechanical stresses, preparation conditions, and thermal treatment.

2.7. Relaxor ferroelectrics

Ferroelectric materials are frequently characterized by their high dielectric permittivity [96]. For a conventional ferroelectric material, the permittivity reaches its sharp maximum value at T_C, which corresponds to the ferroelectric to paraelectric phase transition temperature (figure 2.7 (a)) [97]. However, some materials show different behavior with a significantly broadened peak. Additionally, the temperature at which the permittivity reaches its maximum (T_m)

shifts to higher temperatures with increasing measurement frequency. Such ferroelectrics, named relaxor ferroelectrics, have garnered considerable attention in recent years due to their enigmatic and exceptional dielectric characteristics [84, 98-105], which remain poorly understood. As already mentioned, the temperature of maximum permittivity displays a broad peak, exhibiting a frequency-dependent characteristic [43, 78, 80, 106]. Another property of relaxors is their temperature dependency on polarization. Above T_m, the polarization of relaxors maintains finite values at relatively high temperatures due to the preservation of nanoscale polar domains far above T_m [107]. To help visualize the distinctions between standard and relaxor ferroelectrics, figure 2.7 (a) to (c) compares permittivity, polarization hysteresis, and spontaneous polarization.
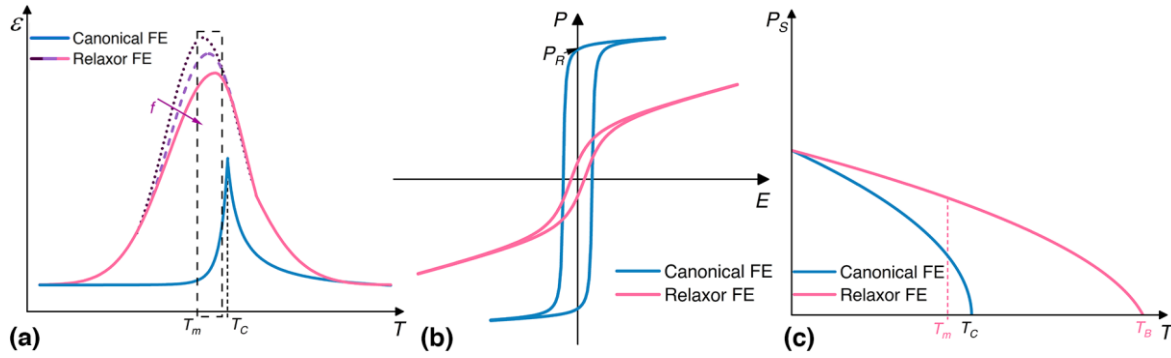
Figure 2.7 - Permittivity, and polarization of canonical ferroelectrics and relaxor ferroelectrics: (a) Comparison of the temperature dependence of permittivity; (b) Polarization hysteresis; (c) Illustration of the variation of the spontaneous polarization by function of the temperature of both classic ferroelectric and a relaxor ferroelectric.

The $P(E)$ hysteresis loop in figure 2.7 (b) is a characteristic of ferroelectrics operating at a low temperature in the ferroelectric phase. The substantial remnant polarization, P_R, demonstrates the ferroelectric phenomenon's cooperative character. In comparison, a relaxor features what is known as a thin, s-shaped loop. When sufficiently strong electric fields are applied, the relaxor's nanodomains may be orientated in the direction of the field, resulting in significant polarization; however, when the field is removed, the majority of these domains revert to their random orientations, resulting in a low P_R as seen in the figure. A ferroelectric's saturation and remanent polarizations diminish with increasing temperature and completely disappear at T_C. The vanishing of polarization at T_C

22

is continuous for second-order phase transitions (figure 2.7 (c)) but discontinuous for first-order phase transitions. Above T_C, there are no polar domains. By contrast, the field-induced polarization of a relaxor diminishes gradually through the dynamic transition temperature T_m and preserves finite values for higher temperatures, owing to the persistence of nanoscale polar domains well above T_m. Despite much research, the structural basis for the relaxor ferroelectrics' unique physical characteristics remains unknown. Numerous review papers provide an in-depth examination of the complicated issue and discuss the numerous models [100, 108-113]. All known models presuppose a disordered occupancy of crystallographically equivalent lattice sites and the presence of polar nanoscale regions (PNRs) [110].
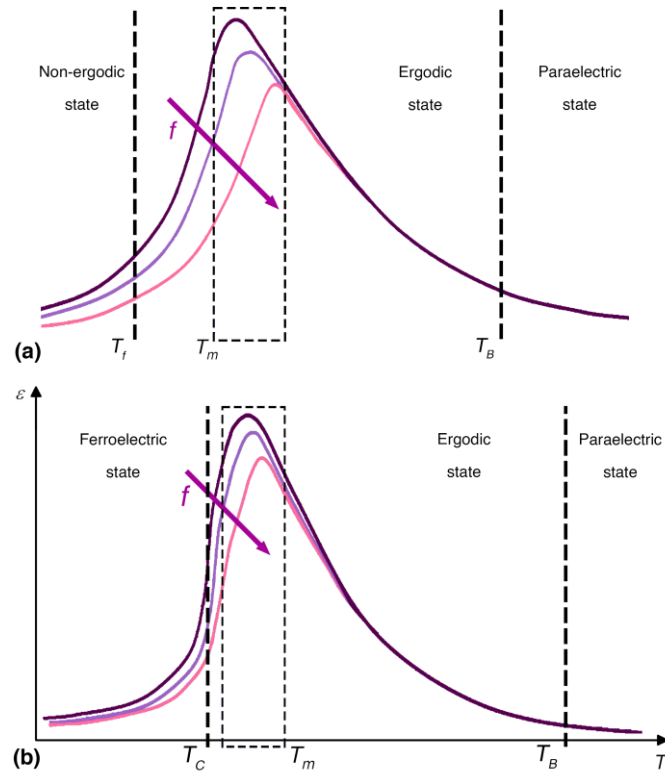
Figure 2.8 - Structure and dielectric properties change with temperature in compositionally disordered perovskites: (a) canonical relaxors with non-ergodic to ergodic transitions; (b) relaxors that undergo a transition from the ferroelectric phase to the ergodic state.

Figure 2.8 (a) illustrates the states and temperatures associated with relaxor ferroelectrics. In almost all perovskite ferroelectrics, PNRs are detected

in the nonpolarized, paraelectric phases. The nucleation of the PNRs begins at the Burns temperature (T_B) and the system transitions to an ergodic state in which PNRs with differently orientated dipole moments are formed. Above T_B, the PNRs vanish, and the crystal becomes regular and paraelectric. The shift to the ergodic state is not a structural phase transition, because the crystal structure remains cubic on both the mesoscopic and macroscopic scales. However, as the physical properties change considerably due to the PNRs, it is typically considered a separate phase in addition to the paraelectric state [110]. PNRs are susceptible to temperature changes and are mobile in the area of T_B. For canonical relaxors, the dipole fluctuations decrease and the PNRs become randomly scattered at the freezing temperature (T_f), implying that their relaxation period becomes infinitely long with reduced mobility. The significant frequency dependency below the temperature of maximum permittivity (T_m) is due to the dipole oscillations in the PNRs being slowed down. The resulting dipolar glass-like state [114-116], in which total polarization is canceled in the absence of an external field, exhibits a number of features in common with the non-ergodic states of a dipole or spin glasses [100]. Relaxors can also undergo a spontaneous transition from the ergodic to the ferroelectric phase in a temperature-dependent manner. Figure 2.8 (b) illustrates this behavior graphically. This demonstrates a diffuse phase transition with T_C being frequency dependent. Accordingly, there may be an abrupt transition at T_C.
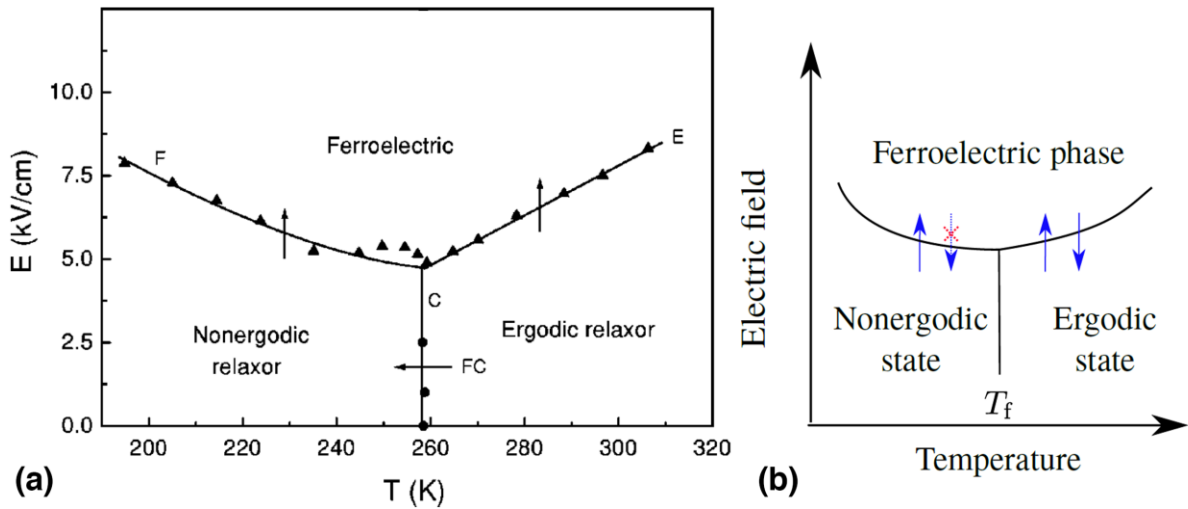
Figure 2.9 - Electric field-temperature phase diagram of 9/65/35 PLZT ceramics: (a) Reversibility and irreversibility of phase transitions [122]; (b) Adaptation of (a) by Ma [121].

Unlike dipolar glasses, canonical relaxors may be induced into a ferroelectric phase by applying a sufficiently strong electric field [117, 118]. This is because relaxors are composed of tiny, randomly oriented polar nanoregions [115, 119, 120] that link to the electric field due to their comparatively high dipole moments, which is a critical distinction from dipole glasses. Figure 2.9 (a) and (b) illustrates this fact for a canonical relaxor. The shift from the non-ergodic to the ferroelectric phase is irreversible, i.e., the ferroelectric phase does not revert to the non-ergodic condition even after the external field is removed [121, 122]. For low-bias field strengths, a temperature shift can transition the non-ergodic state to the ergodic state and vice versa. Relaxors' state shifts and $E(T)$ phase diagram is also dependent on the mechanism by which the ferroelectric phase is achieved [123].

2.8. Characterization of the electrocaloric effect

The electrocaloric effect (ECE) is defined as the adiabatic and reversible change in the temperature of a material in the presence of an applied electric field. Such measurements must be made as a function of temperature in order to get insight into not only the size of the ECE but also its temperature dependency, which are critical qualities for cooling applications. ECE characterization is often classified into two categories: Indirect measurements, and direct measurements.

Direct methods are primarily based on the measurement of the adiabatic temperature change ($|\Delta T|$) with devices such as modified calorimetric equipment [124-130], differential calorimeters [43, 131-135], integrated micro thermometers [136], thermocouples [137], infrared sensors [28, 124, 131, 132], and thermal scanning microscopy [28, 132, 138, 139]. Despite extensive research and development of prototypes for direct measurement of ECE, non-adiabatic situations exist in which the film loses heat to the substrate at a faster rate than the time constant associated with the application (or removal) of the electric field, making a direct determination of electrocaloric temperature change in thin films exceedingly difficult. Due to these inherent measurement problems, the bulk of work to date has relied on the indirect method to quantify the magnitude of the ECE.

The indirect method is based on the determination of the electric polarization $P(T, E)$ as a function of the temperature T and electric field E. The entropy (S) or temperature change ($|\Delta T|$) that the ECE may produce in a suitable material can be determined indirectly. To do this, one can use the Maxwell thermodynamic relationship between the entropy S and the dielectric polarization P:

$$\left(\frac{\partial P}{\partial T}\right)_E = \left(\frac{\partial S}{\partial E}\right)_T \qquad (2.2)$$

From temperature and field-dependent polarization data, the isothermal entropy change ΔS may be calculated:

$$\Delta S = \int_{E_1}^{E_2} \left(\frac{\partial P}{\partial T}\right)_E dE \qquad (2.3)$$

Under adiabatic conditions, the reversible electrocaloric temperature change ΔT is caused by a change in the external electric field $E = E_2 - E_1$.

$$\Delta T = \int_{E_1}^{E_2} \frac{T}{c(E,T)\rho} \left(\frac{\partial P}{\partial T}\right)_E dE \qquad (2.4)$$

The terms $c(E, T)$ and ρ refer to the field and temperature-dependent specific heat capacity and mass density, respectively. In reality, the temperature

change is frequently calculated as follows, assuming that $c(E, T)$ is only temperature dependent, i.e., zero field $c(0)$ and $\Delta T \ll T$:

$$\Delta T = \frac{-T\Delta S}{c}$$
(2.5)

The indirect method is considerably more often employed than the direct method, as it is typically difficult to ensure that the sample is adequately insulated from the environment [11]. Under real-world conditions, a heat exchange occurs between the electrocaloric substance and the surrounding environment. As a result, the temperature of an electrocaloric sample returns after a field-induced temperature change to its starting value after a period of time (figure 2.1 (a) and (b)). To obtain nearly adiabatic conditions, it is required for the heat exchange with the environment to be considerably slower than the field change and thermal measurement. This is a tough criterion for a thin film to satisfy because of its tight thermal connection to the substrate. As an example, Kutnjak et al. showed that, if a 10 K electrocaloric temperature change was produced in a 500 nm thick PbLaZrTiO$_3$ layer on a 0.5 mm thick Si substrate, after 10 ms just a few mK were measured on the layer surface [132].

In recent years, a debate has erupted on the general applicability and accuracy of the indirect method. In particular, equation 2.4 is derived from the Maxwell equation which in turn is only reliable for reversible processes. Therefore, the indirect technique is in principle inapplicable to materials/processes having a high degree of irreversibility (non-ergodic systems), such as relaxor ferroelectrics, antiferroelectrics, and processes involving first-order phase transitions in general, and is hence strictly true only for stress-free systems in thermal equilibrium [71]. However, in actual material systems, other physical processes might cause deviations from these ideal circumstances, resulting in an erroneous ECE determination. Among these are the domain structure [11, 71], thin film stress [140-143], non-ergodic systems [128, 144, 145], and temperature and field dependency of the specific heat [11, 146, 147].

Despite its drawbacks, the indirect approach is an essential practical technique for determining the ECE in thin layers in a simple and rapid manner

[71]. Although the indirect technique does not yield completely accurate parameters, it can be used to approximate the real electrocaloric characteristics.

2.9. Properties of $Na_{0.5}Bi_{0.5}TiO_3$-based ferroelectrics

NBTO was identified by Smolenskii et al. in 1961 [148], and it is considered one of the most promising basic materials capable of replacing lead-containing compounds [149]. NBTO is an environmentally friendly relaxor ferroelectric with piezoelectric properties equivalent to those of conventional ferroelectrics but presenting a broad temperature range closer to the Curie temperature of 320 °C [150-153]. NBTO has a rhombohedral structure with a lattice parameter of 3.88 Å at room-temperature [154]. NBTO changes to the tetragonal phase at 340 °C, followed by the cubic phase at 540 °C [155]. Adding to the fact that relaxor materials have a higher number of degrees of freedom, it is expected to achieve an electrocaloric effect that is even greater than that of conventional ferroelectrics [39, 156].

Due to the 73 kV.cm^{-1} coercive field [155], the high conductivity, and the depolarization temperature (T_d) of around 185 °C [157, 158], which is lower than the Curie temperature, NBTO's applicability at elevated temperatures is limited. Numerous studies have established that the doping of NBTO allows to compensate for these deficiencies. Due to the peculiar fact that both Bi^{3+} and Na^+ occupy the A sites of the ABO_3 lattice [159], NBTO doping is more effective at the A site. $BaTiO_3$ is a common dopant in systems using NBTO. The impact of $BaTiO_3$ on NBTO was examined by Tadashi et al. [160]. The phase diagram is found in figure 2.10 (a). Between a concentration of 5 mol % and a concentration of 6 mol %, a morphotropic phase boundary was identified between the rhombohedral and tetragonal phases.
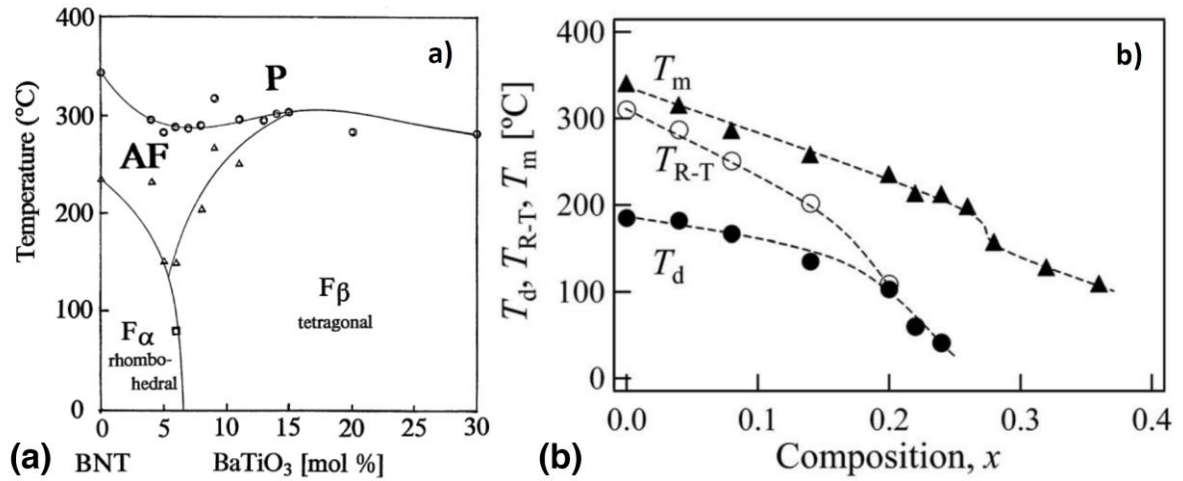
Figure 2.10 - Concentration-induced phase transition of NBTO: (a) BaTiO$_3$ [160]; (b) SrTiO$_3$ [158].

Strontium (Sr) is another frequently used dopant. At room-temperature, Sr-doped NBTO exhibits a rhombohedral structure at a concentration of $x = 0.26$ [68] and a pseudo-cubic tetragonal structure at $x \geq 0.28$. From Hiruma et al. [158], figure 2.10 (b), illustrates a phase diagram of NBTO-STO. As the strontium concentration increases, the phase transition temperature decreases. The presence of an antiferroelectric phase between the ferroelectric and paraelectric phases was demonstrated using hysteresis measurements. Table 2.2 highlights selected |ΔT| values of NBTO that have been reported in the literature.

Table 2.2 - Electrocaloric effect in NBTO-based materials

Materials	T (K)	$\lvert\Delta S\rvert$ J K^{-1} kg^{-1}	$\lvert\Delta T\rvert$ (K)	$\lvert\Delta E\rvert$ kV cm^{-1}	Method	Ref.
Bulk						
$Na_{0.5}Bi_{0.5}TiO_3$	413	0.44	-0.33	50	Indirect	[36]
0.92NBTO-0.08BTO	373	0.27	0.2	40	Indirect	[36]
NBTO-0.06BTO-0.02STO	399	-	1.07	40	Indirect	[66]
NBT-0.06BTO-0.18STO$_3$	344	-	0.75	40	Indirect	[66]
NBTO-0.06BTO-0.22STO	318	-	0.66	40	Indirect	[66]
0.82NBTO-0.18KBTO	433	-	0.73	22	Direct	[161]
0.94NBTO-0.06BTO	408	-	1.5	50	Direct	[162]
0.94NBTO-0.06BTO	373	2.2	1.5	50	Indirect	[70]
0.9NBTO-0.05KBTO-0.05BTO	363	1.47	0.99	50	Indirect	[70]
NBTO	393	-	0.15	20	Direct	[163]
0.94NBTO-0.06KNbO$_3$	349		1.73	70	Indirect	[164]
0.82NBTO-0.18KBTO	353	1.62	1.06	50	Indirect	[70]
0.94NBTO-0.06KNbO$_3$	398		1.5	70	Direct	[165]
0.93NBTO-0.07KNbO$_3$	348		0.8	55	Direct	[165]
0.75NBTO-0.25STO	333	2.52	1.64	50	Indirect	[157]
0.86NBTO-0.06BTO-0.04SBTO	333		0.6	60	Direct	[166]
0.8NBTO-0.2STO	401		0.75	35	Indirect	[167]
$Na_{0.5}Bi_{0.49}Nd_{0.01})TiO_3$	356	0.95	0.69	50	Indirect	[168]
$Na_{0.5}Bi_{0.49}Nd_{0.01}Ti_{0.99}Nb_{0.01}O_3$	381	1.02	0.81	50	Indirect	[168]
0.92NBTO-0.06BTO-0.02SZO	298		0.37	60	Direct	[169]

As previously discussed, doped NBTO-based materials show a general decrease in phase transition temperature. As the electrocaloric properties are higher at the phase transition temperature of a material, this temperature reduction enables a larger $|\Delta T|$ near ambient temperature. However, it is crucial to realize that even a slight change in dopant concentration might result in a decrease in $|\Delta T|$.

To the best of my knowledge, no work has been published on the electrocaloric temperature change in NBTO-based thin films.

2.10. Barium Strontium Titanate

Barium strontium titanate ($Ba_{1-x}Sr_xTiO_3$, BSTO) is a solid solution of barium titanate ($BaTiO_3$ or BTO) and strontium titanate ($SrTiO_3$ or STO). While $BaTiO_3$ and $SrTiO_3$ are both simple perovskite oxides, BSTO is typically called a complex perovskite oxide due to the presence of both Ba^{2+} and Sr^{2+} in the ABO_3 crystal structure [170]. The material possesses outstanding dielectric and ferroelectric properties and is frequently employed in dynamic random access memory [171], pyroelectric infrared detectors [172, 173], and multilayer ceramic capacitors [174]. Additionally, barium strontium titanate has a high pyroelectric coefficient. Due to the fact that the ECE is the inverse of the pyroelectric effect, a high pyroelectric coefficient implies a high ECE.
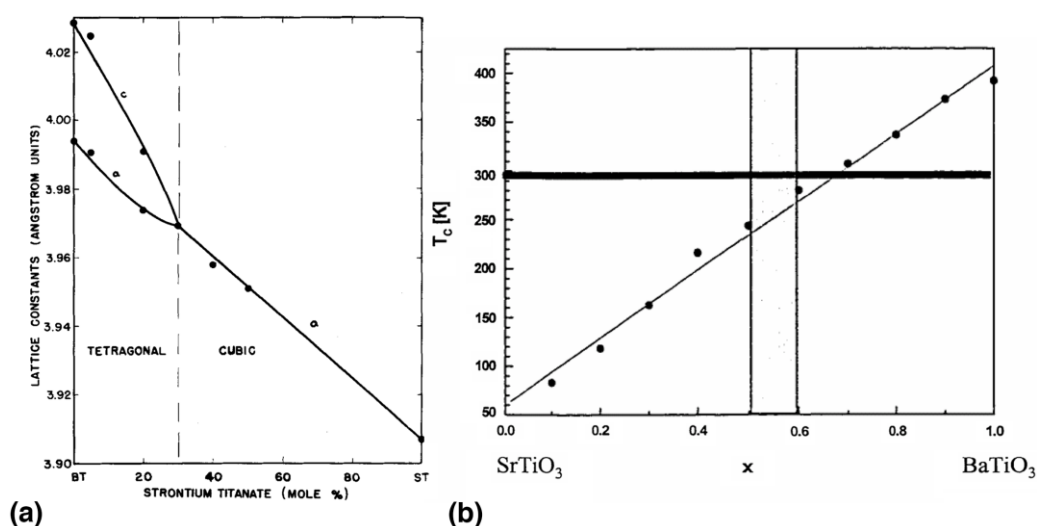
Figure 2.11 - Phase transition of BSTO: (a) crystal structure of BSTO as function of Ba to Sr ratio [170]; (b) ferroelectric phase temperature as a function of the ratio between Ba and Sr [154].

Figure 2.11 (a) shows the lattice parameters of BSTO as a function of the Sr content at room-temperature [175]. BSTO features a tetragonal unit cell similar to pure BTO when $x < 0.3$ and a cubic unit cell when $x \geq 0.3$. As seen in figure 2.11 (b), the paraelectric to ferroelectric transition temperature is nearly a linear function of the Ba to Sr ratio, decreasing with increasing Sr content, and for $x = 0.3$ the ferroelectric transition occurs around ambient temperature, which might be advantageous for cooling devices [176-178]. Additionally, since barium strontium titanate ceramic is free of lead and other heavy metals, it contributes to environmental protection. Table 2.3 summarizes some of the $|\Delta T|$ values in BSTO that have been identified in the literature.

Table 2.3 - Electrocaloric effect in BSTO-based materials.

Materials	T (K)	Thickness (nm)	$\|\Delta T\|$ (K)	ΔE (kV cm^{-1})	Method	Ref.
Bulk						
$Ba_{0.8}Sr_{0.2}TiO_3$	349	-	0.39	20	Indirect	[179]
$Ba_{0.7}Sr_{0.3}TiO_3$	303	-	0.36	20	Indirect	[179]
$Ba_{0.8}Sr_{0.2}TiO_3$	347	-	0.15	10	Indirect	[179]
$Ba_{0.7}Sr_{0.3}TiO_3$	299	-	0.18	10	Indirect	[179]
$Ba_{0.7}Sr_{0.3}TiO_3$	306	-	0.16	10	Direct	[179]
$Ba_{0.65}Sr_{0.35}TiO_3$	298	-	0.18	10	Direct	[179]
$Ba_{0.65}Sr_{0.35}TiO_3$	303	-	2.1	90	Indirect	[52]
$Ba_{0.95}Sr_{0.05}TiO_3$	395	-	0.53	30	Indirect	[27]
$Ba_{0.85}Sr_{0.15}TiO_3$	365	-	0.4	30	Indirect	[27]
$Ba_{0.75}Sr_{0.25}TiO_3$	330	-	0.35	30	Indirect	[27]
$Ba_{0.65}Sr_{0.35}TiO_3$	315	-	0.41	30	Indirect	[27]
$Ba_{0.95}Sr_{0.05}TiO_3$	383	-	1.32	30	Direct	[27]
$Ba_{0.85}Sr_{0.15}TiO_3$	353	-	1.52	30	Direct	[27]

Ba$_{0.75}$Sr$_{0.25}$TiO$_3$	322	-	1.65	30	Direct	[27]
Ba$_{0.65}$Sr$_{0.35}$TiO$_3$	292	-	1.8	30	Direct	[27]
Ba$_{0.9}$Sr$_{0.1}$TiO$_3$	360	-	0.61	33	Indirect	[180]
Ba$_{0.8}$Sr$_{0.2}$TiO$_3$	344	-	1.67	50	Indirect	[181]
Ba$_{0.8}$Sr$_{0.2}$TiO$_3$	338	-	0.83	33	Indirect	[180]
Ba$_{0.7}$Sr$_{0.3}$TiO$_3$	313	-	0.67	33	Indirect	[180]
Films						
Ba$_{0.5}$Sr$_{0.5}$TiO$_3$	250	-	17	500	Simulation	[182]
Ba$_{0.9}$Sr$_{0.1}$TiO$_3$	350	300	1.9	350	Indirect	[178]
Ba$_{0.8}$Sr$_{0.2}$TiO$_3$	314	300	1.75	350	Indirect	[178]
Ba$_{0.7}$Sr$_{0.3}$TiO$_3$	278	300	1.56	350	Indirect	[178]
Ba$_{0.3}$Sr$_{0.7}$TiO$_3$	302	570	1.6	509	Indirect	[183]
Ba$_{0.3}$Sr$_{0.7}$TiO$_3$	310	570	1.4	333	Indirect	[183]
Ba$_{0.3}$Sr$_{0.7}$TiO$_3$	315	570	0.8	158	Indirect	[183]

BSTO is a promising material for electrocaloric studies, with a low electric field saturation and a phase transition that can be shifted close to room-temperature with the variation of Sr content, which is favorable for cooling applications.

3. Research Methods

This chapter describes the experimental aspects of the deposition process and electrical characterization. Standard methods for structural and morphological characterization, such as atomic force microscopy and x-ray diffractometry, are not discussed in this section.

3.1. Sample preparation

Pulsed laser deposition (PLD) was used to deposit NBTO and BSTO-based thin films. A laser beam with a wavelength of 248 nm and a pulse duration of 20 ns is shot from an external KrF excimer laser (Coherent LPX 305i and LAMBDA Physik COMPEX 102, respectively). The laser beam path is made up of diaphragms and attenuators that focus and steer the laser beam to achieve a uniform energy distribution. Guided by mirrors and lenses, the laser beam reaches the deposition chamber, where a focused laser beam area of 3 mm^2 hits the target material. When the laser beam enters the chamber, it passes via a lens and the chamber entry window, reducing the laser intensity by around 10 %. The laser's energy is measured with a sensor outside the deposition chamber and adjusted to the correct value for usage in the deposition. The laser energy density (ω) is computed by taking into account the laser energy loss as it enters the chamber as well as the area of the concentrated laser beam on the target surface. The laser beam enters the chamber and collides with the target substance. A small portion of the surface material is vaporized and ejected, generating an ablation plume of atoms, electrons, ions, and molecules perpendicular to the target material's surface [184-187].
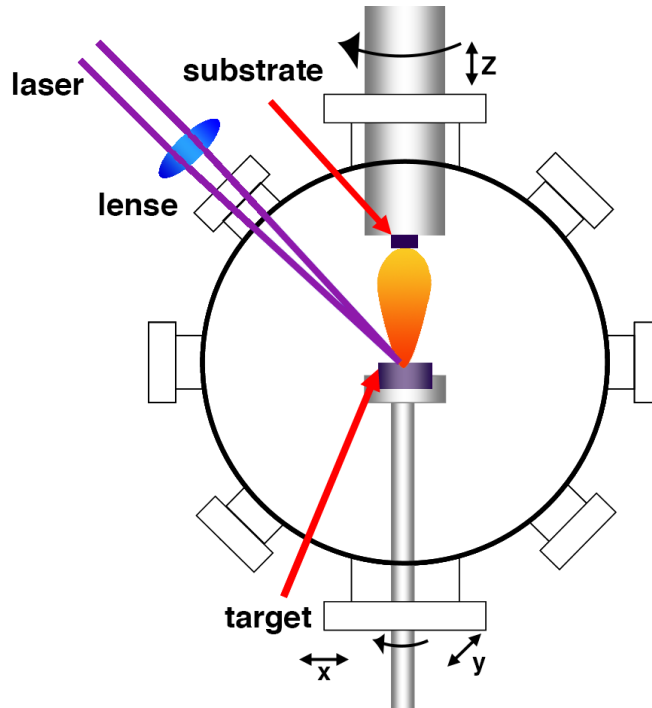
Figure 3.1 - Schematic representation of a pulsed laser deposition (PLD) system.

The extracted material is then deposited as a film on a substrate. The ceramic targets, which have a diameter of 25 mm and a thickness of 5 mm, were made at Fraunhofer IKTS Dresden. The target holder is designed to rotate around its axis and move in the x and y axes to improve the uniformity of the deposition process. Another notable feature is its revolver-like construction, which allows for the support of several targets for the sequential deposition of different layers. During deposition, the target holder is 50 mm away from the target surface, parallel to it, and spins around its axis. Two halogen bulbs are located in the sample container as the heat source. A thermocouple is placed near the substrate to control the deposition temperature (T_{DEP}). For the deposition, a constant oxygen background pressure is set with a controlled oxygen inflow. In the same environment, the samples are heated, coated, and then cooled. An illustration of a PLD system is shown in figure 3.1.

3.2. Sample setup and deposition parameters

Two distinct PLD systems were used to deposit ferroelectric thin films based on NBTO and BSTO. A simple HV system was used for the deposition of NBTO whereas a more sophisticated UHV system was used for the BSTO deposition. The deposition of NBTO-based thin films was carried out following data from the literature [150, 151, 188]. The epitaxial growth of NBTO-based thin films on YAO (a_{YAO} = 3.71 Å), LAO (a_{LAO} = 3.79 Å), and STO (a_{STO} = 3.91 Å) (PDF 00-005-0634) single crystal substrates were evaluated in terms of deposition temperature. At room-temperature, the mismatch between each substrate and NBTO (a_{NBTO} = 3.89 Å) (PDF 01-083-4744) is -4.85 %, -2.6 %, and 0.5 %, respectively, allowing for heteroepitaxial film growth due to the lattice mismatch being less than 5 % [189]. After determining the optimal substrate and deposition temperature, the oxygen background pressure (pO_2), deposition frequency (f_{DEP}), and laser energy density (ω) were adjusted to obtain the optimal deposition parameters. By contrast, the BSTO-based thin films ($a_{BSTO\ x\ =\ 0.3}$ = 3.97 Å (PDF 04-015-0378)) were deposited on STO substrates, with a mismatch of -1.4 %, using the deposition conditions previously described by Engelhardt, et al. [190].

Each substrate measures 10 x 10 mm and is 1 mm thick, with a [001] direction parallel to the surface. Prior to deposition, the substrates are cleaned for three minutes with ultrasound in an acetone bath, soaked in isopropanol, and dried with an argon gas flow. The samples are configured in the manner of a capacitor, with a buffer layer deposited on top of the substrate, followed by a ferroelectric layer and a top electrode for subsequent electrical characterization. Figure 3.2 depicts the samples' schematic structure.
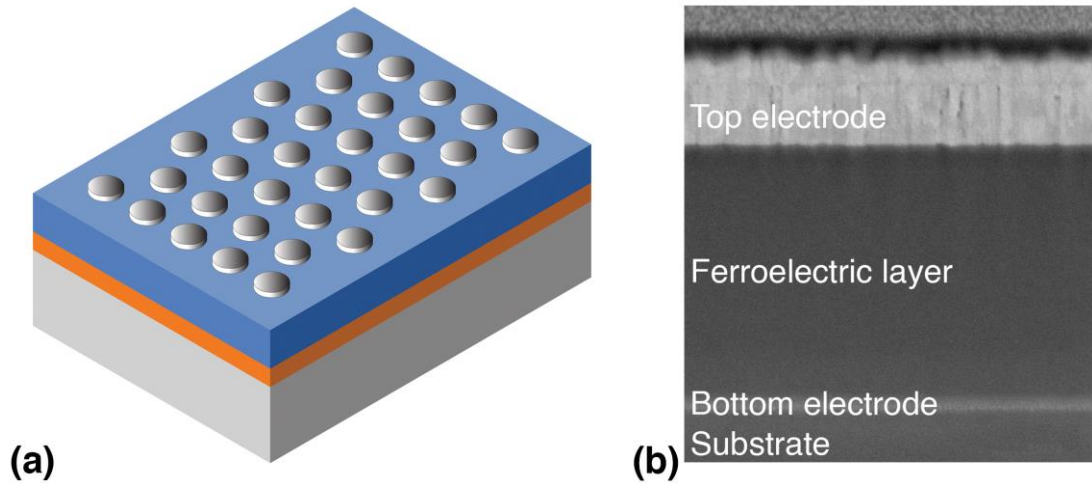
Figure 3.2 - Representation of the sample setup: (a) Schematic representation; (b) Cross-section SEM representing the same sample setup.

NBTO-based thin films were deposited on $La_{0.5}Sr_{0.5}CoO_3$ (LSCO) layer that served as bottom electrode. LSCO has a lattice parameter, of 3.805 Å (PDF 00-036-1394) which gives a lattice mismatch to the LAO substrate of -0.4 %. The BSTO layers were deposited on a buffer layer composed of $SrRuO_3$ (SRO), which has an orthorhombic lattice and can be described as a pseudo-cubic perovskite structure with a minor distortion of the unit cell [191], and a a_{SRO} = 3.910 Å (PDF 04-012-166), resulting in a lattice mismatch of -0.1 % concerning the STO substrate. Both the LSCO and SRO buffer layer acts as an electrode for characterizing the NBTO and BSTO. The deposition conditions of both NBTO and BSTO samples are displayed in the table below:

Table 3.1: Deposition parameters of the bottom electrode and ferroelectric layer for the NBTO and BSTO based thin films samples.

	NBTO		BSTO	
	Bottom electrode	Ferroelectric layer	Bottom electrode	Ferroelectric layer
Deposition temperature, T_{Dep} (°C)	550	550 600 650	750	900
Oxygen background, pO_2 (mbar)	0.3	0.3	0.01	0.01
Laser fluence (J cm^{-2})	1.5	1.5	1.0	1.0
Frequency (Hz)	10	10	5	5

The electrical characterization of the samples requires the use of electrodes above and below the ferroelectric layers. Figure 3.2 illustrates the layer structure utilized. A plate capacitor-like device (figure 3.2 (a)) is utilized with the ferroelectric layer as the dielectric between the bottom and top electrodes. In the case of the NBTO samples, the bottom electrode consists of an, approximately, 20 nm thick LSCO layer. For the BSTO samples, the bottom electrode is made up of a SRO buffer layer, with an approximate thickness of 25 nm. For subsequent access and analysis of the bottom electrode, the LSCO buffer layers were deposited, cooled down, and removed from vacuum. Consequentially, about 1/3 of the sample was covered with a mask, prior to the NBTO deposition. Derived from the work of Engelhardt [192], where the SRO layer was deposited on a separate substrate holder than a $BaZr_xTi_{1-x}O_3$ layer, which allowed a subsequent analysis of a portion of the bottom electrode, in this work, the BSTO layers were deposited immediately after, on the same substrate holder. As a result, the samples were kept in vacuum throughout the deposition process. For both materials, the upper electrodes are made of platinum contacts with a diameter of 200 μm that were deposited using magnetron sputtering and shaped using a lift-off technique. Following the deposition of the top electrodes, the samples were exposed to air at 350 °C for one hour to decrease residual conductivity and dielectric losses [193, 194]. Additionally, BSTO samples were sequentially made in which SRO layers were deposited as a top electrode without

interfering with the vacuum. After photolithography and ion etching, the top SRO layer was sculpted to obtain the structure illustrated in figure 3.2. Due to the layer structure, the ideal plate capacitor equations may be as follows:

$$C_{\|PC} = \varepsilon_0 \cdot \varepsilon_r \cdot \frac{A}{d_{FL}};$$ (3.1)

In this equation, $C_{\|PC}$ indicates the capacitance, ε_0 the permittivity in vacuum, ε_r denotes the relative permittivity of the material, A the area of the top electrode, and d_{FL} is the thickness of the ferroelectric layer.

3.3. Measurement of the polarization hysteresis

Radiant Technologies Precision Multiferroic tester was used to determine the leakage current and the polarization hysteresis of the NBTO and BSTO thin films. Polarization is determined using a process that involves measuring and integrating the incoming or emitted electrical charge. The following fundamental equations apply [195, 196]:

$$D = \varepsilon_0 \cdot \varepsilon_r \cdot E = \varepsilon_0 \cdot E + P = \frac{Q}{A} = \frac{\int I(t)dt}{A};$$ (3.2)

The polarization term refers to the component of the displacement flux density D that is material specific. The displacement current $I(t)$ is obtained using a transimpedance amplifier, the circuit for which is illustrated in figure 3.3. The total excitation voltage (V_{ext}) decreases across the ferroelectric layer (FL) since the input signal is constantly compared against the connection to ground (virtual ground) in the inverting operational amplifier [195]. The measured current is proportional to the voltage drop (V_R) across the reference resistor (R_{ref}).
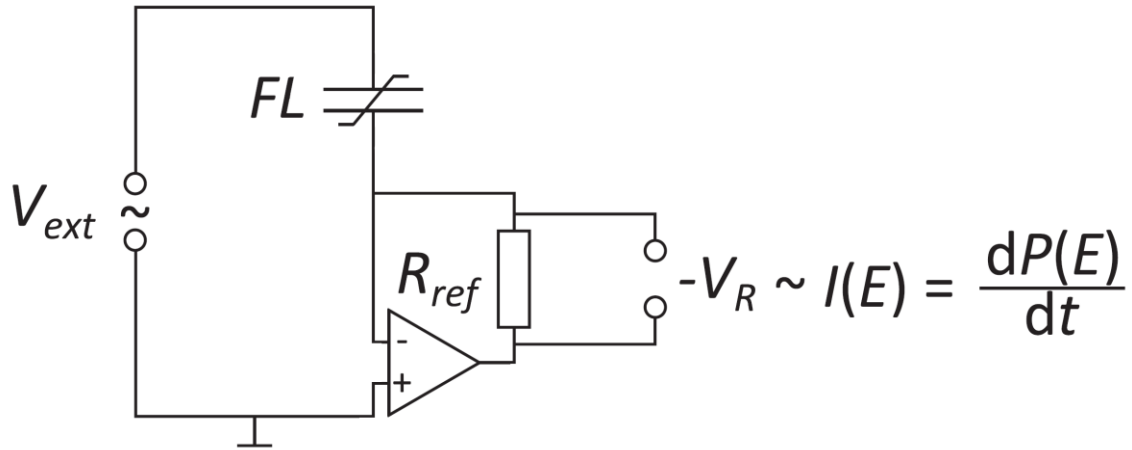
Figure 3.3 - Circuit of a transimpedance amplifier with virtual ground. Adapted from [195].

A double-bipolar voltage profile is utilized to determine the polarization hysteresis at room-temperature, as illustrated in figure 3.4. The voltage is gradually increased to a given V_{max}, then reduced to zero, and then modulated in the negative range until $V = 0$ is attained once more. This initial period (black line in figure 3.4 (a)) is utilized to determine the beginning condition of the sample. In the second phase (red line), the voltage follows the same curve, while measuring the polarization at each voltage step. Figure. 2.6 illustrates the result of such a measurement on a ferroelectric sample. When the applied electric field exceeds the coercive field, the hysteresis loop comprises polarization contributions due to ferroelectric switching processes. On the other hand, switching processes become inconsequential when just the upper positive branch of the hysteresis loop is addressed (dashed red segment in figure 3.4 (a)). Thus, the ECE for removing the external electric field may be calculated using the polarization values of this section of the hysteresis loop.
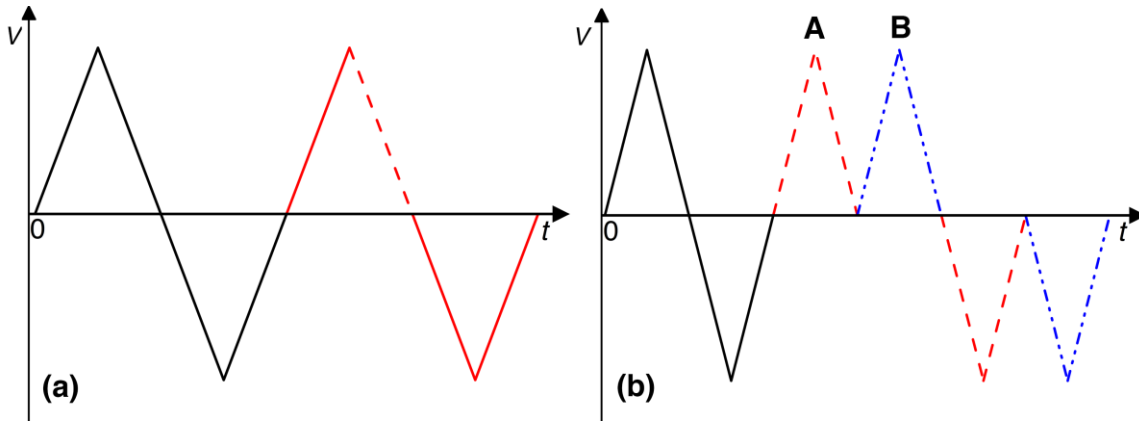
Figure 3.4 - Voltage profile used for hysteresis measurements: (a) Double bipolar voltage profile for hysteresis measurement; (b) Excitation voltage profile for temperature-dependent *P(E)* hysteresis measurements as a function of time. Illustration based on [78].

For the temperature-dependent *P(E)* data, which are utilized to infer the ECE indirectly via equation (2.4), a modified excitation profile provided by Crossley [78] and illustrated in figure 3.4 (b) is used. To begin, the layer is defined by applying a bipolar voltage signal, which leaves the sample with negative polarity. The voltage is then driven twice from zero to $+V_{max}$ and back to zero, followed by a repetition of the same for the negative voltage range. From the segments produced in this manner, a primary and a secondary hysteresis loop can be constructed. The primary hysteresis loop (red dashed line) produces the same result as the double-bipolar voltage profile displayed in figure 3.4 (a). The secondary hysteresis loop (dash-dotted blue line) can be utilized to investigate the ECE's response to an external field. Additionally, the revised waveform gave information regarding parasitic losses in the measuring circuit. Apart from fatigue, irreversible hysteresis, and considerable departure from isothermal conditions, there is no polarization mechanism that may result in a difference in the value of *P* at positions A and B in figure 3.4 (b). Without regard for the preceding, every measurable difference δP (see Crossley, figure 2.6, [78]) must be related to electrical losses. When the loss portion of the circuit is modeled as an analogous parallel resistance R_P (see Crossley, figure 2.3, [78]), the net parasitic charge flowing between locations A and B is provided by *Q = AδP*, and therefore $R_P = 1/Q \int_A^B V \, dt$. The time-resolved spurious contribution of R_P to the observed

42

polarization over the whole waveform may thus be calculated as $P(t) = [1/AR_P] \int_0^t V \, dt$ and subtracted from the measured data.

3.3.1. Measurement configuration

The amplitude and voltage dependences of the leakage current are heavily influenced by the electrode-ferroelectric contact [197]. Thin films with an oxide electrode / ferroelectric / metal structure might be understood as Schottky diodes with opposing connections [197-199]. As a result, leakage currents are always limited by the Schottky contact, which operates in reverse.
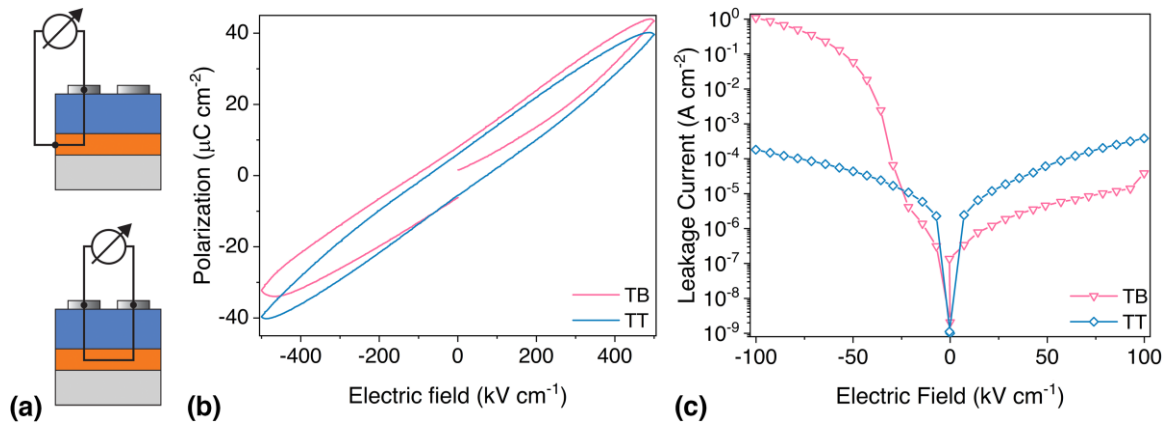
Figure 3.5 - The top-bottom (TB) measurement setup compared to the top-top measurement configuration (TT): (a) Illustration of the measurement setups schematically; (b) Polarization values as a function of field strength for a NBTO thin film sample with Pt top electrodes; (c) Static leakage current density as a function of the electric field for a BSTO sample.

The measuring signal is commonly applied to the top and lower electrodes. This measurement setup is referred to as top-bottom (TB). For comparison purposes, a top-top (TT) configuration was also measured and both configurations are schematically depicted in figure 3.5 (a). When characterizing the samples, the bottom electrode is grounded, and the Pt electrode is excited using an excitation profile. Thus, whether the field strength is either positive or negative, the Schottky contact at the bottom electrode / ferroelectric layer or ferroelectric layer / Pt interface dominates the leakage current. Figures 3.5 (b) illustrates the hysteresis loop of a NBTO thin film measured in the TB and TT configuration. While there is a closed hysteresis loop for the TT configuration, in

the case of the TB configuration, the hysteresis loop is tight in the positive field strength range, whereas it manifests a distinct increase in the negative field strength range. This expansion increases with increasing field strengths and is caused by the influence of a leakage current. Static leakage current measurements, on a BSTO sample (Fig. 3.5 (c)), demonstrates that the leakage current density achieves much greater values in the negative field strength range than in the positive field strength region. Thus, for positive and negative field strengths, there is a diode-like behavior with reverse and forward directions. The significant leakage currents observed in the negative field strength range in figure 3.5 (c) are therefore associated with the ferroelectric / Pt interface and imply that the matching Schottky barrier becomes permeable in the reverse direction even at low field strengths.

3.4. Indirect measurement of the electrocaloric effect

The process for assessing the electrocaloric characteristics of the ferroelectric thin film is illustrated below. Hysteresis loops are monitored at various temperatures in order to determine the *P(E, T)* connection. It is typically initiated at the highest temperature and reduced in 10 K increments as it cools. The cooling rate is set to 5 K per min and is maintained for one minute after reaching the desired temperature. Figure 3.6 (a) illustrates five *P(E)* observations of a temperature series ranging from 150 to −150 °C. After subtracting the R_P correction, the higher positive branch of the primary hysteresis loop is used for further evaluation. The *P(E)* loops are used to obtain the polarization values for discrete field strengths as a function of temperature. Due to the fact that the specific *E* values of the individual data points in the various *P(E)* measurements vary according to the measuring device employed, the data must be adapted. A polynomial of fourth degree is employed in this case. The fit's findings are depicted in figure 3.6 (b) for a range of five temperatures. This enables the evaluation of all hysteresis branches at precisely defined field strengths and the interpolation of the *P (E, T)* connections. After that, the *P(E, T)* dependences are fitted in order to calculate the derivative $(\partial P / \partial T)_E (T)$.
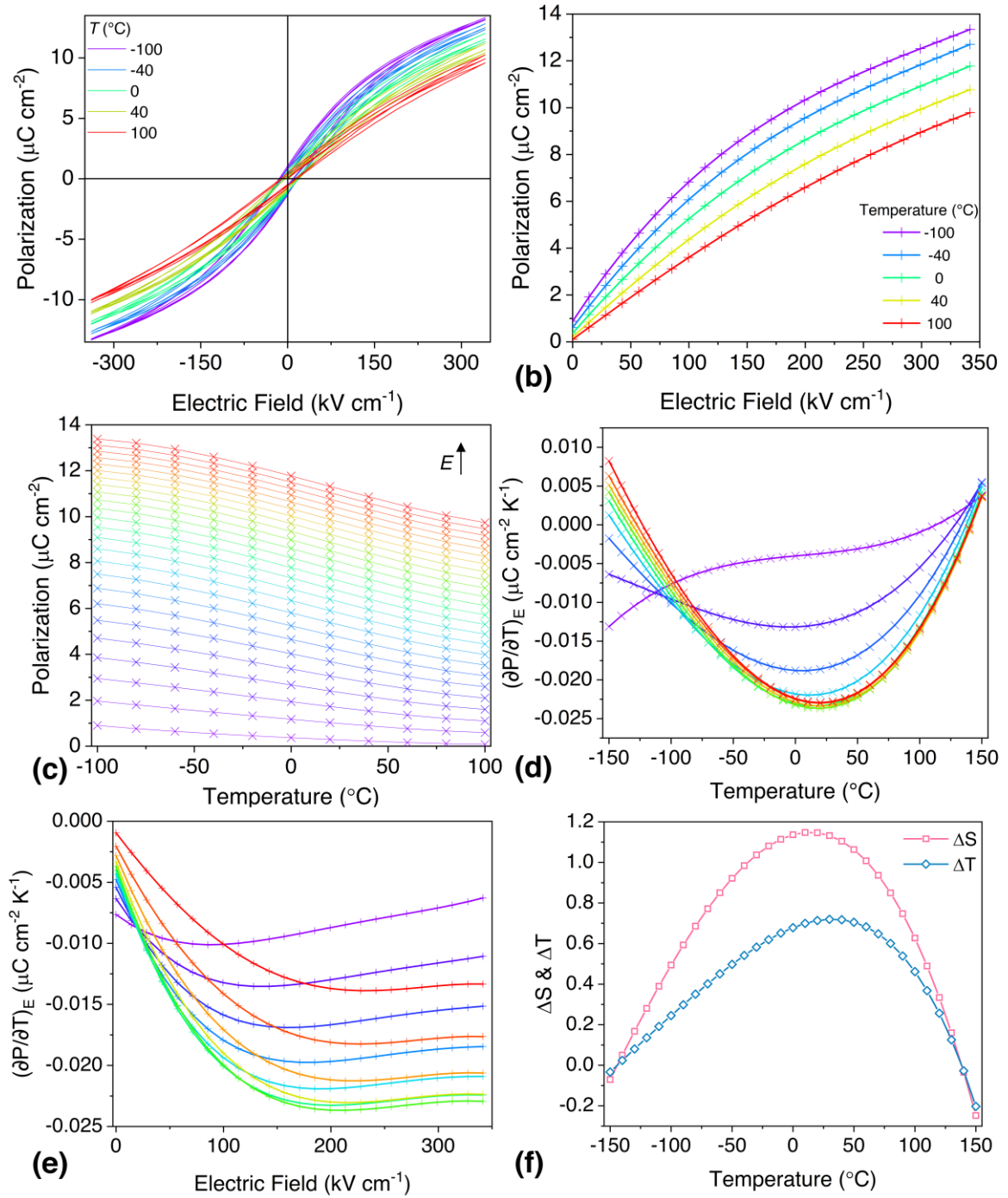
Figure 3.6 - Standard data evaluation for the indirect method of determining the adiabatic temperature change |Δ*T*|: (a) Hysteresis loops for *P(E)* at various temperatures. (b) The upper positive branches of the *P(E)* hysteresis loops, shown for different temperatures. (c) Relationship between *P(T)* and for various field strengths. (d) $(\delta P / \delta T)_E$ as a function of temperature and field strength. $(\delta P / \delta T)_E$ values were determined at various temperatures and are displayed in (e). (e) Fit of the $(\delta P / \delta T)_E$ values. (f) |Δ*S*| and |Δ*T*| as a function of the initial temperature *T* for varying magnitudes of field strength variations.

Figure 3.6 (c) shows the adjustments for the various field strengths. Figure 3.6 (d) illustrates the derivation of the $(\partial P/\partial T)_E(T)$ functions. This is used to determine the $(\partial P/\partial T)_E$ values at specified temperatures. This results in the $(\partial P/\partial T)_T(E)$ dependencies, which are depicted in figure 3.6 (e). To calculate $|\Delta S|$, the integral in equation (2.3) is determined using the $(\partial P/\partial T)_T(E)$ relationships which are additionally fitted with a polynomial of fourth degree and the antiderivatives are produced. The $|\Delta T|$ values computed using equation (2.4) are plotted in figure 3.6 (f) as a function of the initial temperature for various E_1 values (E_2 is zero for all curves).

The equation for determining the electrocaloric temperature change (equation 2.4) incorporates the temperature and field-dependent specific heat $c(E, T)$. The specific heat is considered to have a relatively mild temperature dependency and its field dependence is ignored. As shown by Hatta et al. [200, 201], ferroelectric materials, such as BTO, exhibit a significant peak in their specific heat capacity $c(E = 0, T = T_c)$ at the Curie temperature. Strukov et al. [202] determined a rising specific heat capacity of 2.1 J cm^{-3} K^{-1} to 3.1 J cm^{-3} K^{-1} on a range of temperatures varying from -100 °C to 150 °C after examining polycrystalline BTO layers with layer thicknesses ranging from 20 nm to 1.1 µm and observing an increasingly diffuse anomaly of the specific heat. Sawai et al. [203] measured the specific heat capacity of bulk $Ba_{1-x}Sr_xTiO_3$ ($x = 0.2$) in a temperature range starting at -120 °C to 75 °C. The specific heat capacity can be seen in figure 3.7.
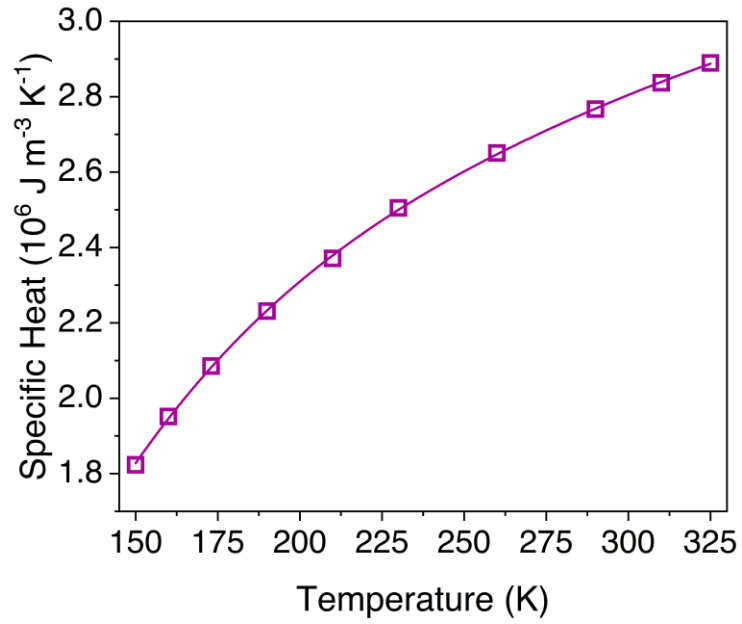
Figure 3.7 - Specific heat regarding temperature for *x* = 0.2 of BSTO.

In the vicinity of the Curie temperature, the *c* maximum becomes significantly broader [147]. Given that the specific heat in epitaxial thin films is already defined by a diffuse curve at *E* = 0, it is expected that disregarding the field dependence of the specific heat is substantially less critical for thin layers with diffuse transformation behavior than it is for samples with an abrupt phase transition.

4. Structural and electrical properties of Na$_{0.5}$Bi$_{0.5}$TiO$_3$-based thin films

The study of dielectric and ferroelectric properties of epitaxial NBTO-based thin films as well as the subsequent characterization of the ECE by the indirect method requires dense layers with smooth interfaces. In the following chapter, the efforts to realize such epitaxial NBTO film architectures on different substrates using optimized deposition temperatures are summarized. Afterward, the growth of NBTO layers doped with BaTiO$_3$ and SrTiO$_3$, MnO$_2$, and an excess of Bi$_2$O$_3$ and Na$_2$CO$_3$ are discussed. Here, we choose a composition, which revealed good electrocaloric properties close to room-temperature as bulk material [66].

4.1. Na$_{0.5}$Bi$_{0.5}$TiO$_3$-based materials

The crystal structure of the NBTO-based targets employed for subsequent deposition was first determined using x-ray diffraction. Figure 4.1 shows the measured patterns.
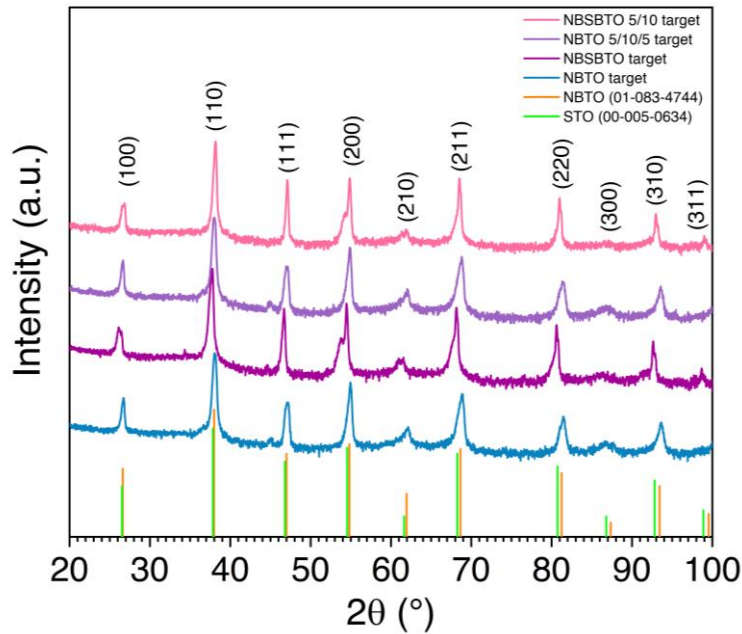
Figure 4.1 - XRD scans of the NBTO-based targets used in this work. The lines are taken from the ICDD PDF-4 database.

For the purpose of comparison, the reference lines corresponding to pure NBTO in accordance with PDF 01-083-4744 and to STO according to PDF 00-005-0634 are also shown in the figure. The following table defines the abbreviations used in the following:

Table 4.1 - Definition of the used abbreviations.

| Abbreviation	Target composition
NBTO	$Na_{0.5}Bi_{0.5}TiO_3$
NBSBTO	$Na_{0.38}Bi_{0.38}Sr_{0.18}Ba_{0.06}TiO_3$
NBTO 5/10/5	$Na_{0.5}Bi_{0.5}TiO_3$ + 5 mol % Bi_2O_3 + 10 mol % Na_2CO_3 + 5 mol % Mn_2O_3
NBSBTO 5/10	$Na_{0.38}Bi_{0.38}Sr_{0.18}Ba_{0.06}TiO_3$ + 5 mol % Bi_2O_3 + 10 mol % Na_2Co_3

The XRD pattern can be indexed with a pseudo-cubic perovskite structure for the NBTO and the NBTO 5/10/5 target. Additional peaks are visible for the NBSBTO and NBSBTO 5/10 target (most obvious close to the (200) peak), which might be either the result of a secondary phase (most likely due unreacted STO) or an indication of a tetragonal structure, which was reported for BTO-doped NBTO (compare for example PDF 00-036-0735). The pure NBTO material has a pseudo-cubic structure with a lattice parameter of 3.89 ± 0.01 Å, whereas a slightly larger value of 3.90 ± 0.01 Å was determined for the NBSBTO target. With the addition of an excess of 5 mol % Bi_2O_3, 10 mol % of Na_2CO_3, and 5 mol % Mn_2O_3, the lattice parameter for the NBTO 5/10/5 target is reduced to 3.88 ± 0.01 Å. By contrast, the NBSBTO 5/10 target, has the same lattice parameter as the NBSBTO target with a value of 3.90 ± 0.01 Å. In general, these differences are quite small and might be the result of a variation in stoichiometry. In particular, a Na excess might increase the lattice parameter, while Mn reduces it. The last effect is probably due to B-site replacement (Mn^{4+} in Ti^{4+} places, due to Mn^{4+} having a smaller ionic radius (0.53 Å) [204] than Ti^{4+} (0.605 Å) [204]). The reduction in the lattice parameter has also been attributed to a decrease in oxygen vacancies [205-207].

4.2. Structural properties of $Na_{0.5}Bi_{0.5}TiO_3$-based thin films

4.2.1. Epitaxial $Na_{0.5}Bi_{0.5}TiO_3$ thin films

The structure, morphology, and electrical characteristics of epitaxial thin films based on $Na_{0.5}Bi_{0.5}TiO_3$ were investigated in order to determine their potential for ECE. To begin, pure NBTO layers were grown on different substrates and optimized for epitaxial growth. Following structural characterization using XRD and AFM, their electrical properties were determined using measurements of the leakage current and polarization hysteresis. The results are summarized below.

Considering data from the literature [150, 188], different deposition parameters were varied to study the epitaxial growth of the NBTO-based thin films. The initial step was to evaluate the preparation on different single crystalline substrates. Therefore, pure NBTO films were deposited on LSCO-buffered LAO, YAO, and STO substrates at temperatures ranging from 550 to 650 °C. The XRD patterns mostly exhibit (00ℓ) peaks of the NBTO film, which are close to the subsequent (00ℓ) substrate peaks (see figure 4.2 (a) for films on LAO, YAO, and STO deposited at 550°C). Whereas these peaks are clearly discernible on LAO and YAO, the NBTO peaks are scarcely visible on the STO substrates due to the almost identical c-axis lattice parameters (3.89 Å and 3.905 Å for NBTO and STO, respectively; compare lines in figure 4.1). Therefore, more detailed studies were mostly conducted on the first two substrates. Reflections emerging from the LSCO buffer layer are also barely discernible in all XRD patterns due to the low film thickness of roughly 20 nm and partial overlap with the strong substrate peaks.
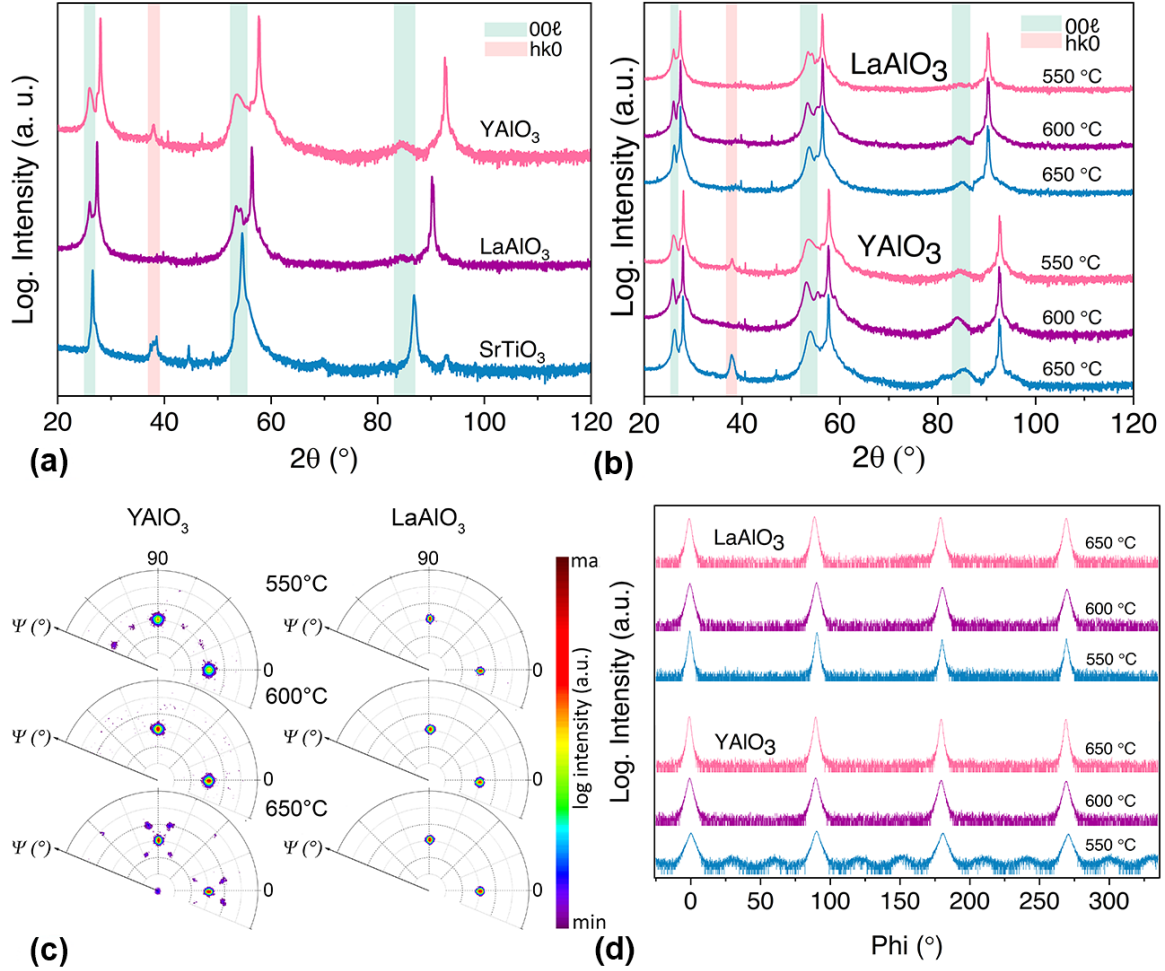
Figure 4.2 - Structural characterization of NBTO films: (a) XRD scans of the NBTO films deposited on a STO, LAO and YAO substrate at 550 °C using 5000 pulses, an oxygen background of 0.3 mbar and f = 10 Hz; (b) XRD scans showing the influence of the substrate and the deposition temperature on the growth of NBTO films with a thickness of about 150 nm; (c) Pole figure measurements of the (110) NBTO peak for films grown on YAO and LAO substrates at different deposition temperatures; (d) Phi-scans of the NBTO samples deposited on YAO and LAO at different temperatures.

The results for films deposited at different temperatures are summarized in figure. 4.2 (b). For the NBTO layer on YAO, only (00ℓ) peaks are apparent for a deposition temperature of 600°C implying an epitaxial growth, whereas an additional minor peak corresponding to a (110) crystal orientation is seen at a 2θ angle of about 37.9° for samples deposited at 550 and 650 °C, respectively (figure 4.2 (b)). In contrast, these misoriented peaks did not occur in the films on LAO for all temperatures, indicating epitaxial growth over a broad temperature range, corresponding to a low defect density on the NBTO layer. The out-of-plane lattice

parameters of the samples deposited on LAO and YAO substrates are substantially larger than those of the target material (a = 3.89 Å), but within the range of other groups' results [39], suggesting that the unit cell is distorted tetragonally.

The epitaxial growth between the NBTO layer and the single crystal substrates was studied as a function of temperature using pole figure measurements and phi-scans (figure 4.2 (c) and (d)). All (110) pole figures exhibit a fourfold symmetry with strong peaks at Ψ = 45°, suggesting that the orientation was in general transferred epitaxially from the single crystal to the NBTO thin film via the LSCO buffer layer. However, at 550 and 650 °C, the pole figures of NBTO grown on YAO exhibit additional reflections, which are related to different texture components. As a result, only at 600 °C, an undisturbed epitaxial growth is observed (as visible in figure 4.2 (c)). In comparison, no other texture components were detected in films grown on LAO substrates across the temperature range investigated. In general, the epitaxial relationship is NBTO (001) [100] || LSCO (001) [100] || LAO (001) [100] (using the pseudo-cubic notation for the rhombohedral single crystal). The substrate dependence might be explained by differences in the lattice parameters of the single crystals utilized and will be discussed in more detail below. Figure 4.2 (d) shows the phi-scans of the NBTO samples. The full width at half-maximum (FWHM) values of the peaks are summarized in table 4.2 as well as the in-plane and out-of-plane lattice parameters.

Table 4.2 - FWHM values and in-plane and out-of-plane lattice parameters for samples deposited on YAO and LAO substrates at different temperatures.

Substrate	Temperature (°C)	FWHM (°)	In-plane (Å)	Out-of-plane (Å)
YAO	550	3.6 ± 0.1	3.84	3.96
	600	2.5 ± 0.1	3.87	3.99
	650	1.5 ± 0.1	3.85	3.96
LAO	550	1.5 ± 0.1	3.87	3.93
	600	2.5 ± 0.1	3.83	4.02
	650	1.9 ± 0.1	3.84	4.01

The FWHM values of the films are significantly larger than the values of the single crystalline substrates (typically 0.6° for LAO). This orientation spread of the grains might be due to the lattice mismatch, structural distortions, or residual stresses. It can also reveal an increase in the structural disorder and number of defects of a material, by the widening of the peak [208]. In the case of YAO substrates, an increasing temperature results in a reduction of the FWHM value, which may indicate a reduction in the number of defects. Nonetheless, the existence of extra reflections in the pole figure indicates different texture components in these films, which are not desired for the current study. On LAO substrates, on the other hand, no clear trend is observable, as the FWHM values are smallest at low temperatures, larger at 600 °C, and smaller again at 650 °C.
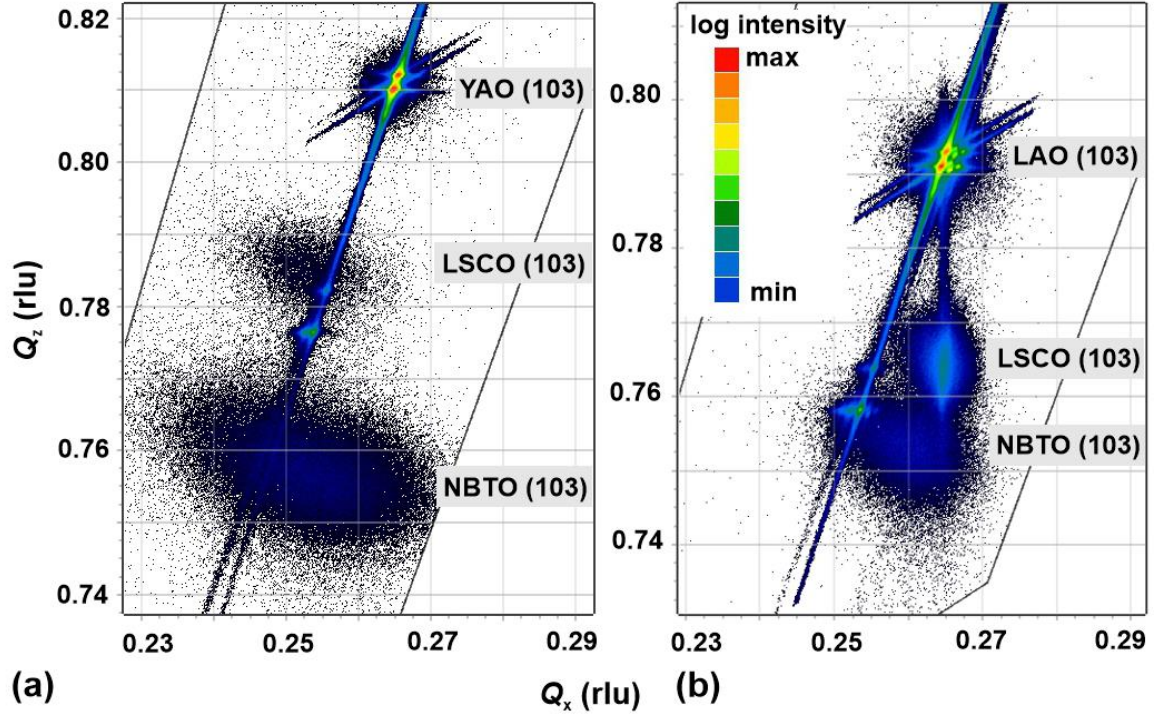
Figure 4.3 - RSM maps for NBTO films grown on: (a) YAO at 600 °C and (b) LAO at 550 °C using a LSCO buffer layer.

Furthermore, RSM measurements were performed on the deposited samples. Figure 4.3. compares the results of an epitaxial film on YAO deposited at 600 °C with the sample on LAO deposited at 550 °C. For YAO, these RSM maps indicate that the LSCO buffer layer grows already relaxed due to a larger lattice misfit of about 3.4 % (see figure 4.3 (a), where LSCO has a different Q_x value than the substrate peak). In contrast, this buffer layer grows strained on LAO having a significantly smaller misfit of around 2.1 % (compare figure 4.3 (b), where the LAO and the LSCO exhibit similar Q_x values). As a result, more defects and/or a subgrain structure may be expected at the LSCO surface on YAO if compared to the LAO surface, as also indicated by the widening of the buffer layer peak in reciprocal space. This may have in turn an effect on the nucleation of the following NBTO layer, resulting in a larger temperature window for undisturbed epitaxial growth on LAO. As a result, films deposited at 550 °C on LAO were preferred for the following investigations of NBTO-based materials. From the RSM data, the NBTO in-plane lattice constant was determined to be 3.87 Å for LAO, corresponding to a tetragonal distortion of c/a = 1.1, whereas a value of 3.84 Å was obtained on YAO, equivalent to a c/a = 1.03. It should be

noted that the diffraction spots of the NBTO (103) peak are significantly broadened in the RSM maps, which indicates small coherent scattering sizes (i.e., small grain size and/or a large number of defects), as well as strain and compositional gradients.
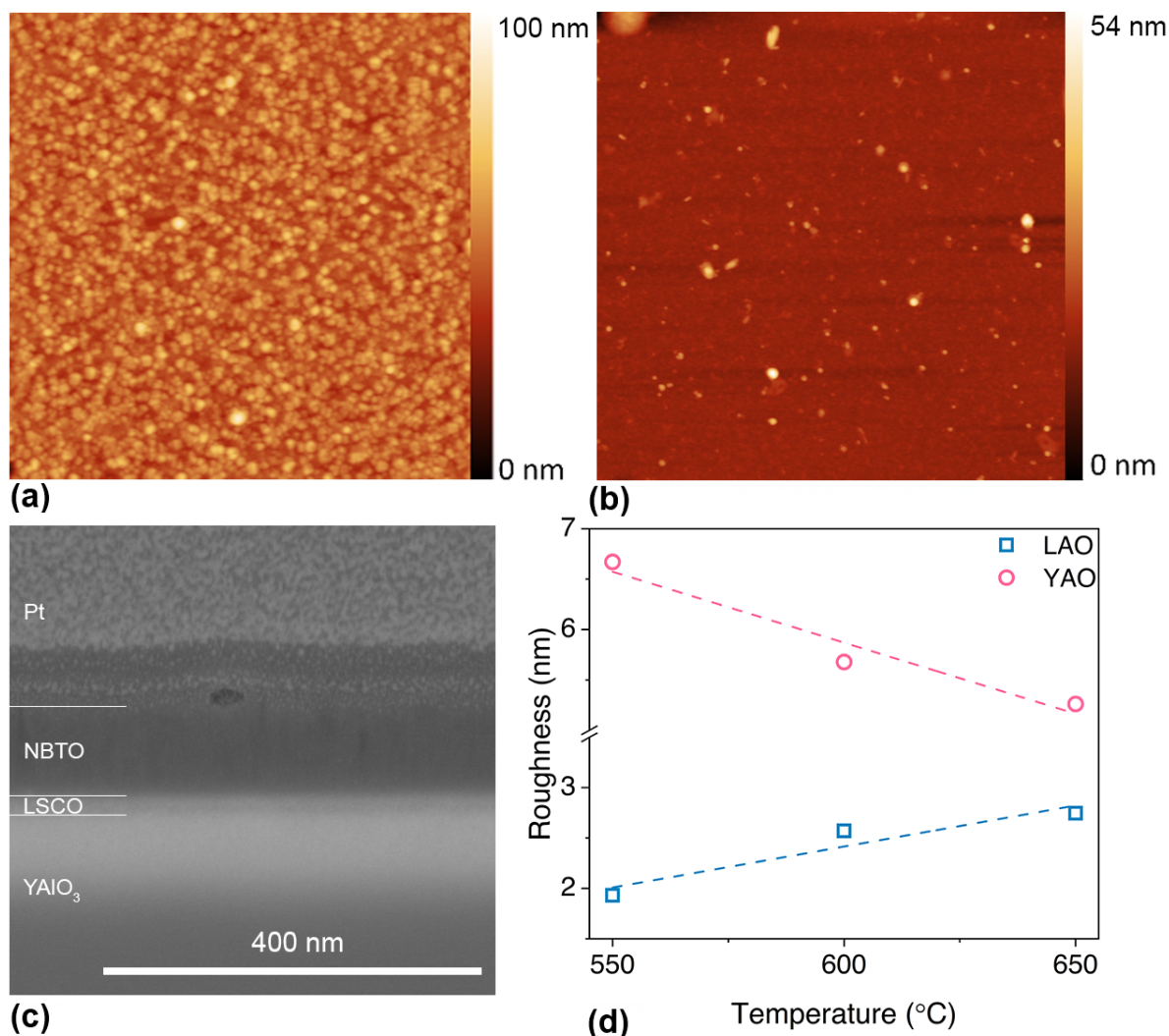
Figure 4.4 - AFM images with a size of 5 μm by 5 μm of about 150-nm-thick NBTO layers grown at 550 °C on: (a) YAO and (b) LAO; (c) FIB cross section of the NBTO layer grown on YAO/LSCO substrate; (d)Surface roughness of the samples deposited on YAO and LAO at different temperatures.

Finally, we investigated the effect of substrate and temperature on surface morphology. AFM scans were performed on films of comparable thickness produced on YAO and LAO substrates. The film on YAO has a heterogeneous structure with a small grain size and a high density of emerging, almost quadratic grains with a size of around 50 nm (figure 4.4 (a)), and a root mean square (rms)

roughness of 6.7 nm. The sample on the LAO substrate has a lower roughness, with a rms value of 1.9 nm (figure 4.4 (b)). Again, emerging grains with a height of up to 50 nm are observed on the surface. The rough surface was validated using a FIB cross-section, as seen in figure 4.4 (c) for one sample, where columnar structures extending the whole thickness of the sample may be seen. The roughness of the samples deposited on both substrates at temperatures ranging from 550 to 650 °C is shown in figure 4.4 (d). While an increasing temperature results in a decrease in layer roughness on YAO substrates, the opposite behavior is observed for films on LAO substrates. A higher-resolution AFM scan was performed to examine the surface morphology in greater detail, as seen in figure 4.5. (a).
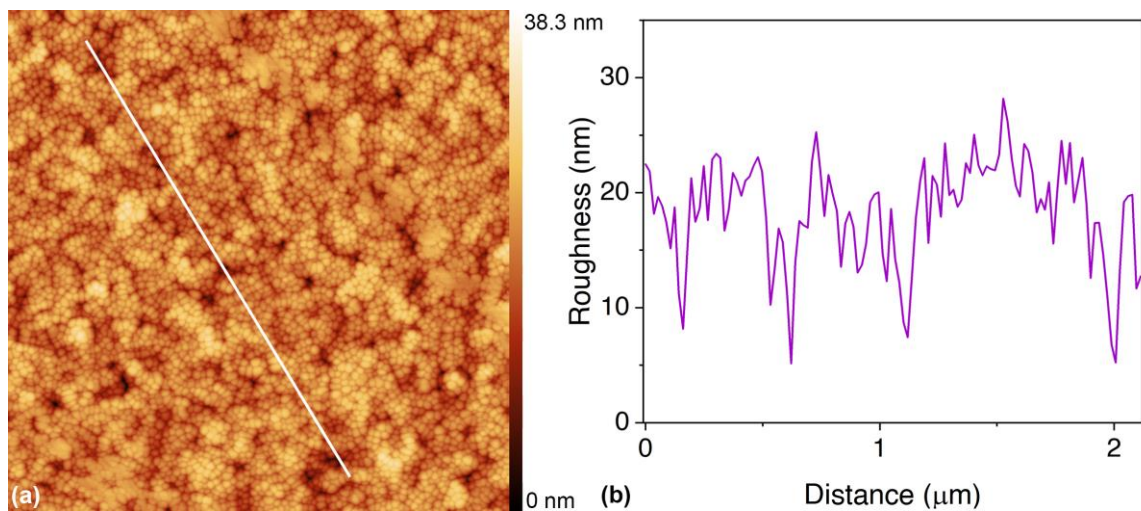
Figure 4.5 - AFM scan and consequent surface roughness profile of: (a) AFM image (2 μm by 2 μm) of a NBTO sample grown at 550 °C on LAO; (b) Roughness profile taken along white line shown in subfigure (a).

The AFM scan reveals a significant degree of roughness, with a mean value of 3.8 nm. It is heterogeneous in structure, with small grains agglomerated into larger islands. Pores are also visible in figure 4.5(a) and are connected to the columnar structure in figure 4.4 (c). Figure 4.5 (b) depicts a profile of the surface roughness. The approximate depth of the pores and the size of the agglomerates are seen here. Due to the fact that only the surface is scanned and that the tip has a pyramidal shape, the proper depth of the pores cannot be determined unequivocally. Nonetheless, the surface profile (figure 4.5 (b)) reveals pores with a depth of more than 10 nm, which will have an effect on the interface between

the top electrode and the BSTO layer, resulting in an inhomogeneous electric field distribution and leakage currents, which have an impact on the samples' electrical characteristics.

The volatile nature of Na and Bi might lead to changes in stoichiometry. Therefore, an excess of these elements was added in the form of Na_2CO_3 and Bi_2O_3 to compensate for its loss during the high-temperature sintering and the PLD deposition. Additionally, NBTO exhibits both strong residual polarization and a high coercive field value [209]. This latter disadvantage has spurred a lot of investigations to lower the coercive field in bulk and thin films [210, 211]. Manganese (Mn) doping of NBTO has been shown to minimize leakage current, therefore increasing the polarization performance by decreasing oxygen vacancy levels and consequently the contribution of electron holes [212-216]. Thus, targets with an excess of Bi and Na as well as targets doped with Mn were evaluated to see whether such targets result in enhanced characteristics. The resulting XRD pattern is shown in figure 4.6 (a).
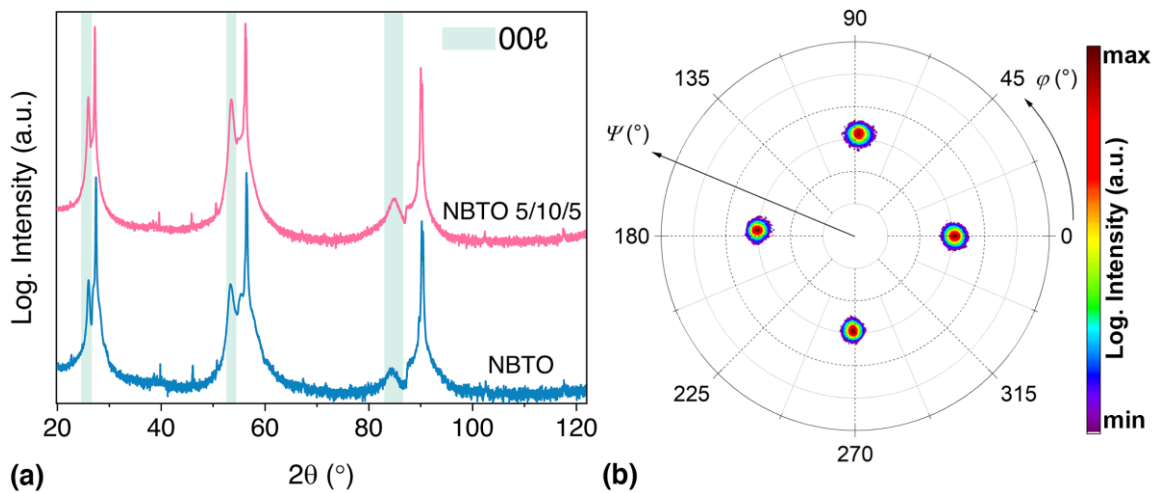
Figure 4.6 - Structural characterization of the doped NBTO film: (a)XRD scans of the NBTO and NBTO 5/10/5 deposited on LAO at 600 °C; (b) Pole figure measurements of the (110) NBTO peak for films grown on and LAO at 600 °C.

For the doped NBTO thin film only (00ℓ) peaks are apparent for a deposition temperature of 600 °C implying an epitaxial growth, with an out-of-plane lattice parameter of 3.97 Å. The in-plane lattice parameter of 3.85 Å implies a tetragonal distortion of c/a = 1.03. The FWHM (not shown) has a value of 2.5 ± 0.1 ° equal to the NBTO sample deposited at 600 °C. Pole figures (figure 4.6 (b))

exhibit a fourfold symmetry with strong peaks at $\Psi = 45°$, suggesting that the orientation was in general transferred epitaxially from the single crystal to the doped NBTO thin film via the LSCO buffer layer. Unfortunately, it was not possible to determine the exact stoichiometry for thin films due to the influence of the substrate and the small amount of materials.

4.2.2. Epitaxial $Na_{0.38}Bi_{0.38}Sr_{0.18}Ba_{0.06}TiO_3$ thin films

Based on the results obtained with pure NBTO films, epitaxial $Na_{0.38}Bi_{0.38}Sr_{0.18}Ba_{0.06}TiO_3$ (NBSBTO) layers were grown at various deposition temperatures on LSCO buffered LAO substrates. The XRD patterns reveal again mostly (00ℓ) peaks of the NBSBTO film that are close to the peaks of the substrate (figure 4.7). In contrast to the results of the target measurement (figure 4.1), only a single (002) peak is visible, indicating that Sr (and Ba) were incorporated into the NBTO crystal structure during the PLD process. Again, the buffer layer reflections partially overlap with the strong substrate peak due to the comparable lattice parameters of LSCO and LAO, therefore the peaks are barely distinguishable. The out-of-plane lattice parameters are 3.95 ± 0.03 Å marginally smaller than those of pure NBTO films.
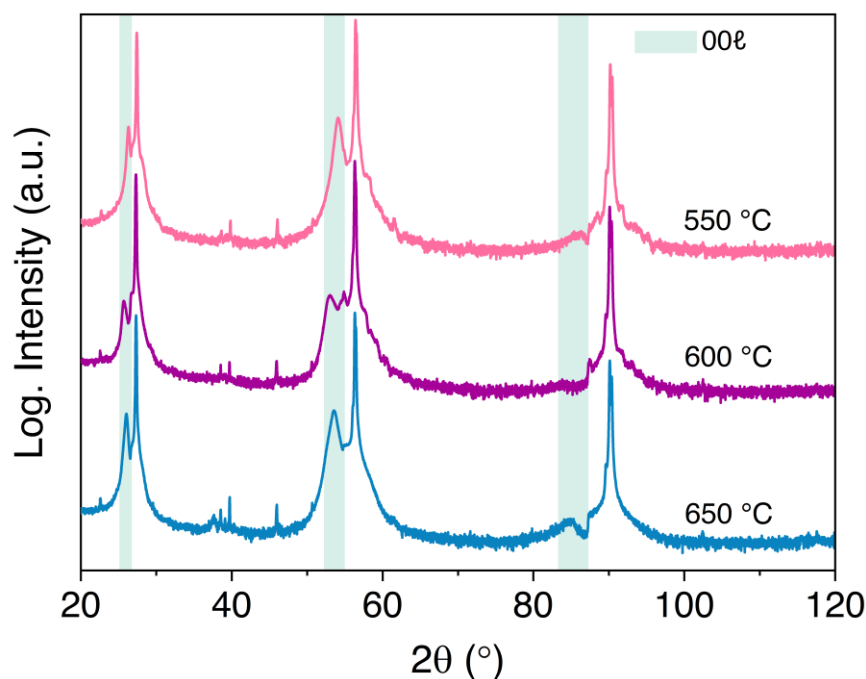
Figure 4.7 - XRD scans of NBSBTO grown on LAO substrates at different temperatures.

The epitaxial relationship between the NBSBTO layer and the single crystalline substrate was investigated using pole figure measurements (figure 4.8 (a)). As with pure NBTO, all (110) pole figures exhibit a four-fold symmetry, showing that the orientation was transferred epitaxially from the LAO single crystal to the LSCO buffer layer and then to the NBSBTO thin film. There is no other texture component of this material detectable for all deposition temperatures investigated. The phi-scans show a wide peak for the sample deposited at 600 °C, narrowing at 550 °C and being the narrowest at 650 °C.
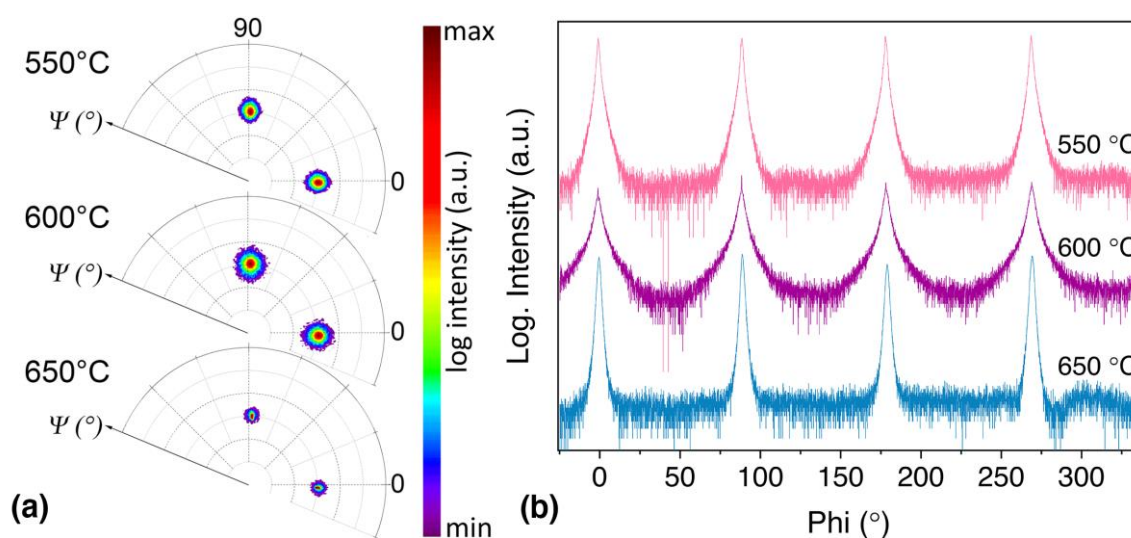
Figure 4.8 - Structural characterization of NBSBTO samples: (a) Pole figure measurements of the (110) NBSBTO peak for films grown on LAO substrates at different deposition temperatures; (b) Phi-scans of the NBSBTO samples deposited on LAO at different temperatures.

Additionally, the effect of film thickness was investigated for NBSBTO layers. Figure 4.9 (a) illustrates XRD scans of three distinct films for a 2θ range close to the (001) substrate peak. The two thinner films were deposited at a rate of approximately 0.15 nm s^{-1} in the same manner as the other films discussed previously. In comparison, the NBSBTO film with a thickness of around 1 µm was grown substantially faster, at a rate of approximately 1 nm s^{-1}. The films with a thickness of 75 nm (c = 3.93 ± 0.01 Å) and 250 nm (c = 3.94 ± 0.01 Å) exhibit (00ℓ) peaks with a minor increase in the lattice parameter (i.e., smaller 2θ values). Using the same deposition rate, similar results were obtained for different thicknesses up to 400 nm (scans not shown). In comparison, the 1 µm thick film

exhibits a significantly larger out-of-plane lattice parameter (c = 4.00 ± 0.03 Å) and an extra (110) peak.
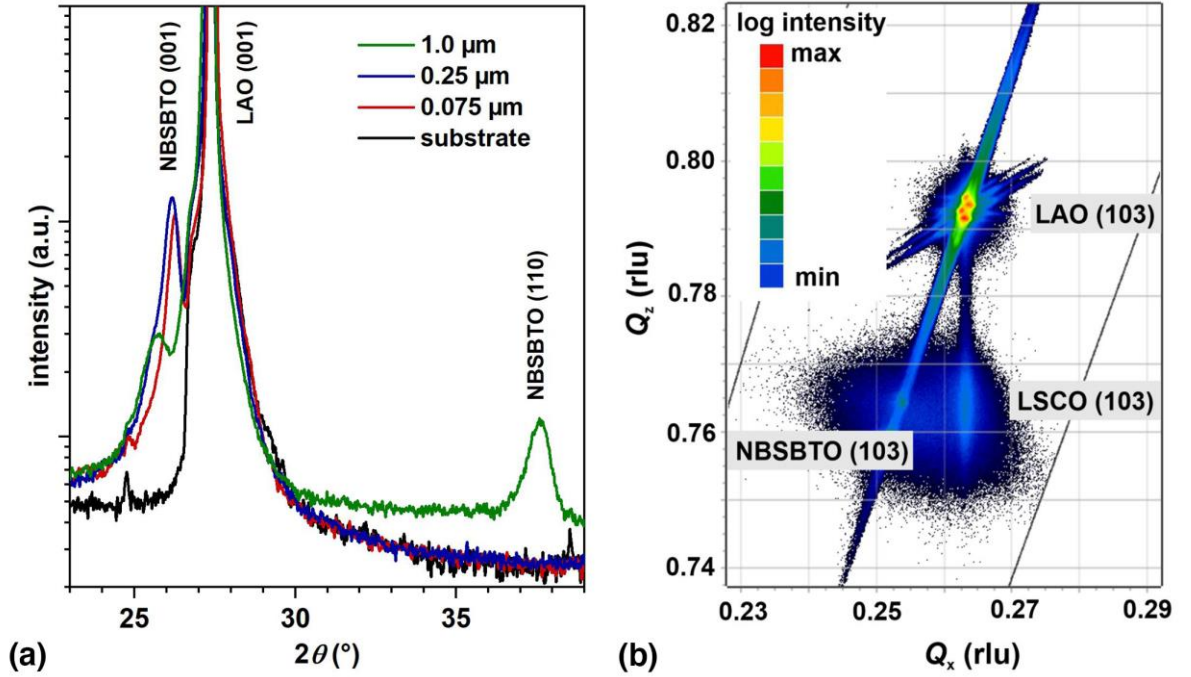
Figure 4.9 - Structural characterization of NBSBTO films: (a) XRD scans of NBSBTO film with different thicknesses grown on LSCO-buffered LAO substrates; (b) RSM map of the (103) peaks for a 400 nm thick NBSBTO layer grown on LSCO buffered LAO at 550 °C.

Once more, RSM was used to determine the in-plane lattice parameters of NBSBTO films; one example is shown in figure 4.9 (b). Similar measurements were performed on samples deposited at higher temperatures. The LSCO layer's strained growth was confirmed for all temperatures by observing similar Q_x values to those seen for the single crystal peak. The NBSBTO in-plane lattice constant is around 3.85 Å somewhat bigger than those of the substrate (c = 3.79 Å), while its out-of-plane lattice constant is 3.94 Å. The difference between the in-plane and out-of-plane lattice parameters with c/a = 1.02 confirms once again the tetragonal distortion of the unit cell, as observed for pure NBTO films.
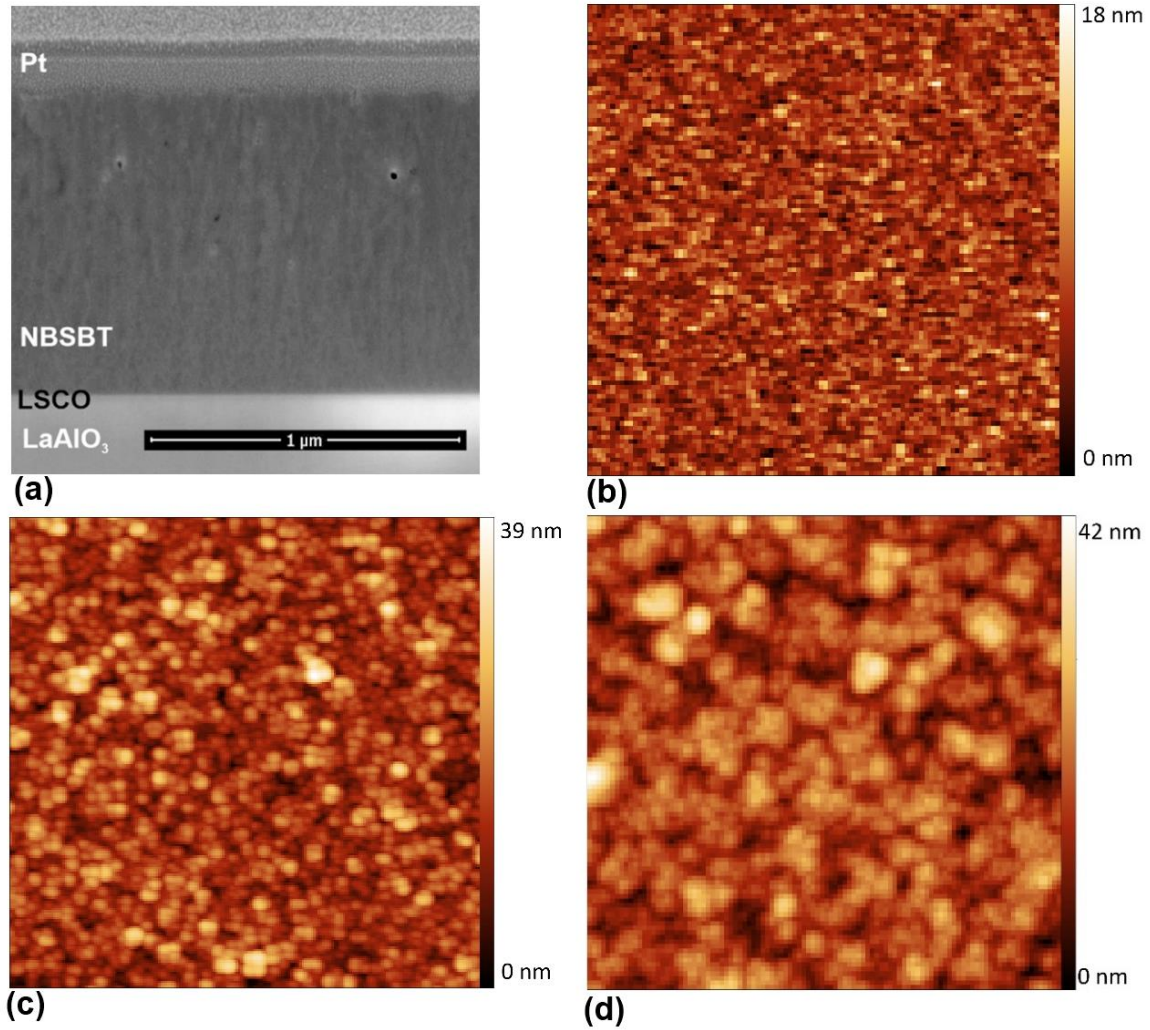
Figure 4.10 - Morphology of the NBSBTO samples: (a) Cross-section SEM image of the NBSBTO sample with 1 μm thickness; AFM scan with a size of 2 μm by 2 μm for NBSBTO grown at 550 °C with a thickness of: (b) 75 nm, (c) 400 nm, and (d) 1 μm.

SEM pictures of NBSBTO film cross-sections were utilized to determine their thickness and to characterize their overall morphology. All samples exhibit a dense structure with columnar grains and some extra pores that extend the full thickness of the film (see figure 4.10 (a) for the 1 μm thick sample). Columnar structures are frequently observed in thin films and may be the result of island nucleation and growth. AFM scans of films with varying thicknesses were used to investigate the surface morphology. Having a thickness of around 75 nm, the film exhibits a uniform and fine structure with a grain size of approximately 10 ± 0.8 nm (figure 4.10 (b)). As the film thickness increases, bigger grains are detected, as illustrated in figure 4.10 (c) and (d), with an average size of around

20 ± 1.3 nm for 400 nm and a grain size of about 23 ± 1.6 nm for 1 µm thin film. Additionally, with the thickest layer, agglomerates of smaller grains with a size of up to 200 nm and bigger pores are apparent. This might be related to the misorientation observed in the XRD scan regarding the (110) peak. Simultaneously, the rms roughness increases from 2.6 nm over 5.8 nm to 6.5 nm for the samples shown. The growing particle size and roughness imply that grains become coarser as they grow in thickness, with some grains being overtaken by others.
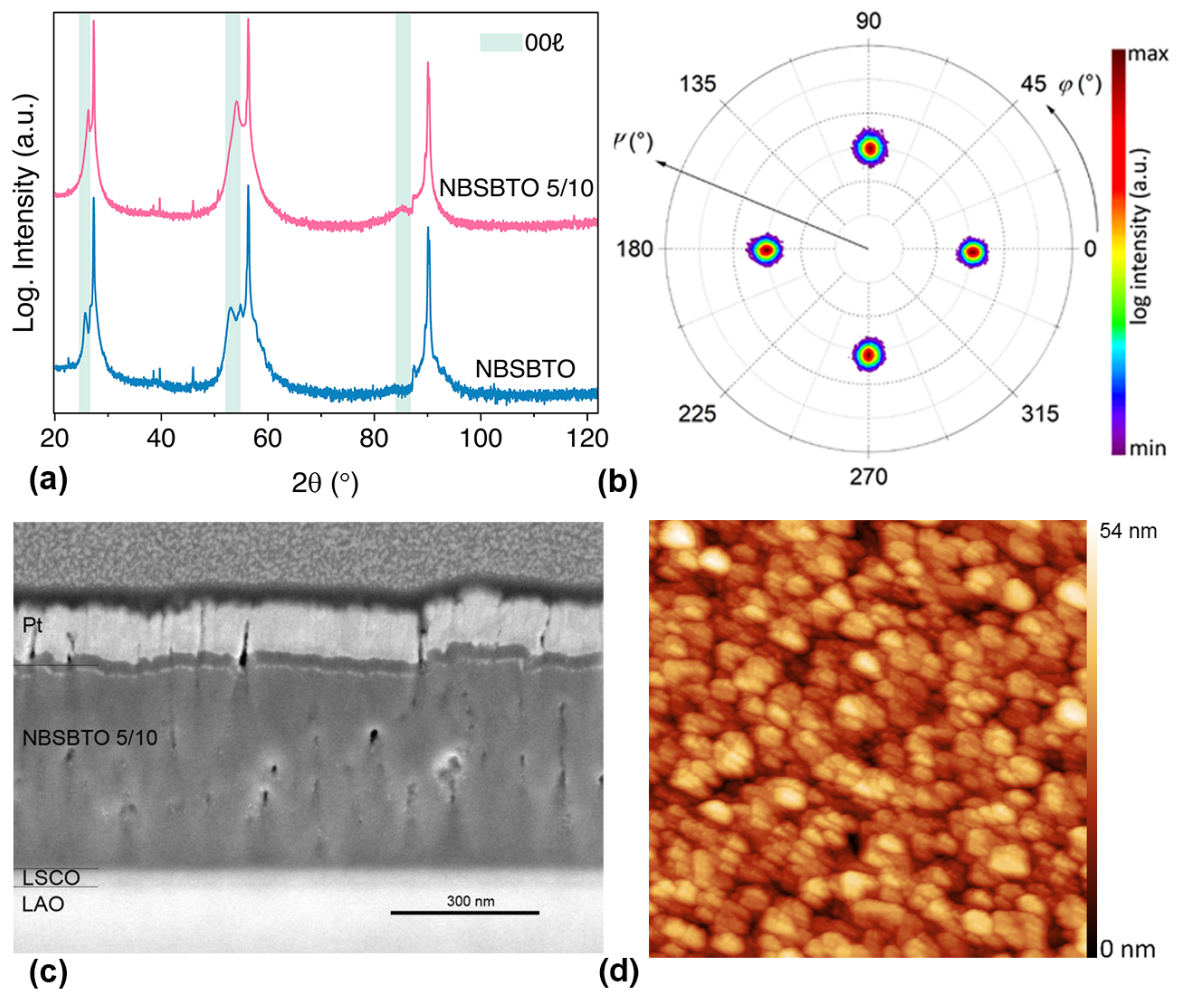
Figure 4.11 - Structural and morphological characterization of the doped NBSBTO: (a) XRD scans of the NBSBTO and NBSBTO 5/10 deposited on LAO at 600 °C; (b) Pole figure measurements of the (110) NBSBTO 5/10 for films grown with the same conditions; (c) cross-section of an, approximately, 400 nm doped NBSBTO thin film; (d) AFM scan of a 2 µm by 2 µm of a doped NBSBTO thin film.

To compensate for the loss during the high-temperature sintering and the PLD deposition, again Bi_2O_3 and Na_2CO_3 were added to a second NBSBTO

target, which was used afterward for the film deposition. The XRD patterns once again show exclusively (00ℓ) peaks of the NBSBTO 5/10 film as seen in figure 4.11 (a). With an in-plane lattice parameter of 3.83 Å and an out-of-plane lattice parameter of 3.94 Å, a tetragonal distortion of about 1.03 is found. As with pure NBSBTO deposited at the same temperature, the (110) pole figure shown in figure 4.11 (b) exhibits fourfold symmetry, indicating that the orientation was epitaxially transferred from the LAO single crystal to the LSCO buffer layer and then to the NBSBTO 5/10 thin film. Figure 4.11 (c) depicts a cross-section SEM of a thin film with a thickness of about 400 nm. It contains a large number of defects. Even at the interface between the dielectric layer and the top layer, the presence of pores is easily noticeable. Additionally, a significant degree of surface roughness is seen, which is corroborated by the AFM scan in figure 4.11 (d), which has a rms of 7.24 nm.

Although the high roughness and emerging grains may make it difficult to evaluate dielectric and ferroelectric characteristics, a preliminary electrical characterization was performed for the NBTO and NBSBTO-based thin films.

4.3. Electrical properties of NBTO-based thin films

The dielectric and ferroelectric properties of NBTO-based thin films are critical for the characterization of the electrocaloric effect. Thus, polarization hysteresis, leakage current, and permittivity were investigated in order to characterize the grown films.

4.3.1. $Na_{0.5}Bi_{0.5}TiO_3$-based thin films

After preparing Pt contacts, the polarization hysteresis loops $P(E)$ and leakage currents were measured at different temperatures for chosen samples when an electric field of up to 375 kV cm^{-1} was applied. Exemplary results for an NBTO layer grown at 550 °C on an LSCO/LAO substrate are presented in figure 4.12 (a) and (b).
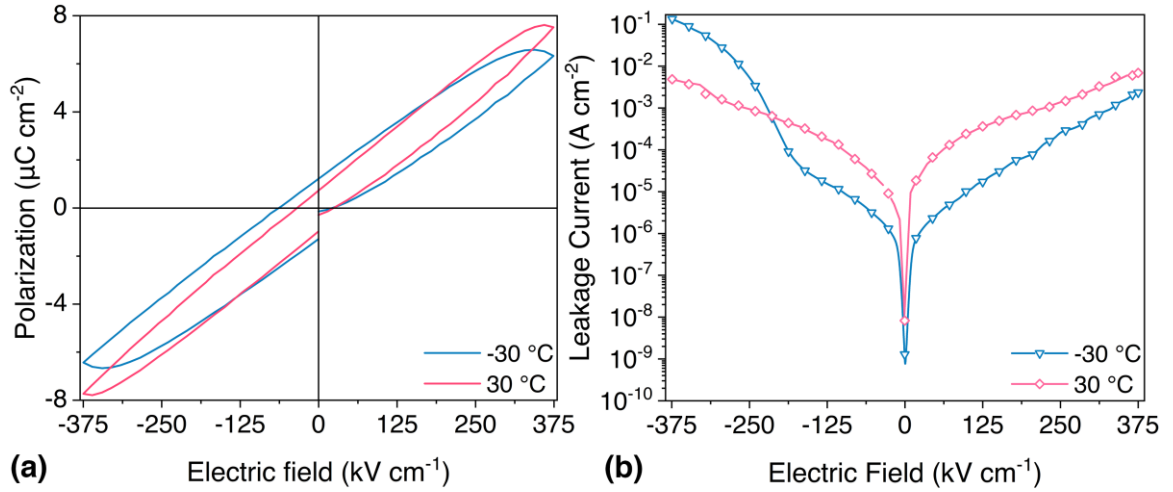
Figure 4.12 - Electrical measurements at different temperatures for a NBTO layer grown on a LAO/LSCO substrate at 550 °C. (a) *P(E)* measurement with a frequency of 1 kHz; (b) leakage current measurement.

For NBTO samples deposited at 550 °C, the polarization was measured at -30°C and 30°C, to compare the value of the maximum polarization and the shape of the hysteresis loops. The polarization loops are asymmetrical and do not show any ferroelectric behavior, making redundant the comparison of maximum polarization. Due to this asymmetric behavior, it was not possible to obtain the coercive field and remnant polarization. Leakage current measurements were taken to verify this. The results are shown in figure 4.12 (b). For all temperatures and both polarities, the results suggest an exponential rise in current density with an applied electric field. For a temperature of -30 °C, at the positive branch, a maximum leakage current of 5.1×10^{-4} A cm^{-2} was observed for a field of 350 kV cm^{-1}, but for the negative branch, the leakage current increased to 1.3×10^{-1} A cm^{-2}. Similar behavior is observed when films are deposited at a higher temperature or on the YAO substrate. These samples show a significantly larger resistive contribution. The high surface roughness with protruding grains, extra pores (not shown), and a significant number of defects, such as oxygen vacancies, might account for the high leakage currents.

In summary, epitaxial growth of pure NBTO layers was achieved, where the use of LAO substrates resulted in the widest parameter window. However, all deposited samples showed a significant roughness and high leakage currents, which hindered a dielectric analysis and resulted in poor ferroelectric

characteristics. As a result, we concentrated on doped NBTO films in order to determine if the addition of BaTiO$_3$ and SrTiO$_3$ leads to enhanced thin film characteristics for this material.

4.3.2. Epitaxial Na$_{0.38}$Bi$_{0.38}$Sr$_{0.18}$Ba$_{0.06}$TiO$_3$ thin films

As described in Section 2.9, doping NBTO with BTO and STO enhances the dielectric characteristics. Temperature-dependent permittivity measurements were done to corroborate this.

All samples have been subjected to temperature-dependent dielectric tests in order to determine their permittivity. Unfortunately, the majority of samples again exhibit substantial leakage currents at elevated temperatures, preventing a comprehensive study. Nonetheless, some results were acquired for the approximately 1 μm thick film in order to compare them to data collected on bulk material that had been treated similarly to the target [217]. Figure 4.13 shows both datasets.
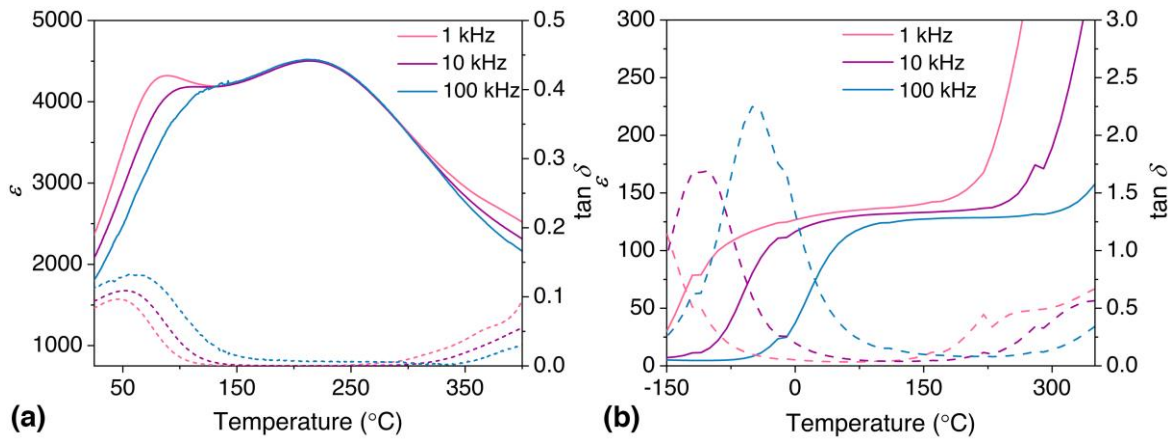
Figure 4.13 - Relative permittivity and loss tan δ of: (a) bulk NBSBTO at different frequencies (data adapted from [217]); (b) 1 μm NBSBTO sample grown on LAO.

For temperatures below 130 °C, the permittivity of the bulk material is temperature-dependent. The tan δ demonstrates a frequency dependency with a local maximum at low frequencies that moves to room-temperature at higher frequencies (see figure 4.13 (a)). In other publications, this tan δ peak is referred to as the depolarization temperature (T_d) [157, 158]. By contrast, at about 220 °C, the temperature of maximum permittivity (T_m) exhibits negligible frequency

dependency, whereas tan δ approaches a minimum. It should be noted, that also other groups got comparable results [218].

The temperature dependence of the permittivity for the predominantly epitaxial film with a thickness of about 1 μm is shown in figure 4.13 (b). In general, permittivity values are significantly lower, as is frequently observed for thin films. At low temperatures, tan δ exhibits a frequency-dependent peak similar to that of the bulk material. The values, however, are significantly higher, and the maximum is moved to lower temperatures with a greater frequency shift. This behavior might imply that T_d has shifted to lower temperatures, either as a result of the tetragonal distortion or owing to stoichiometric changes. An increase in tan δ is noticed at higher temperatures, which may be due to large leakage currents. As a result, the permittivity increases abnormally at high temperatures (the onset is seen in figure 4.13 (b)). As with bulk materials, the permittivity has a low-frequency dependency between 50 and 200 °C, but across a narrower temperature range. Even though the qualitative temperature and frequency dependence of the dielectric characteristics appears to be comparable for bulk and thin film materials, the thin film results should be interpreted cautiously due to a significant resistive contribution to leakage measurements.

The effect of temperature on the electric field-dependent polarization hysteresis *P(E)* and the leakage current is seen in figure 4.14 (a) and (b) for the same sample. Polarization and leakage current measurements were made at -100 °C and 30 °C, respectively, using a 1 kHz frequency. At low temperatures, the sample exhibits a distinctive s-shape and closed polarization loop, which is typical for thin film materials [106]. The highest polarization was 8.3 μC cm^{-2}, the remnant polarization was 1.2 μC cm^{-2}, and the coercive field was 58 kV cm^{-1}. Whereas low-temperature polarization measurements imply symmetric hysteresis loops, room-temperature polarization measurements reveal an asymmetric behavior. The unusual shape may be attributed mostly to resistive contributions, i.e., electrical pathways across the film resulting in loop deformation [195]. As a result, this data cannot be used for indirect ECE

characterization due to the requirement for polarization measurements in function of applied temperature over a wider temperature range.
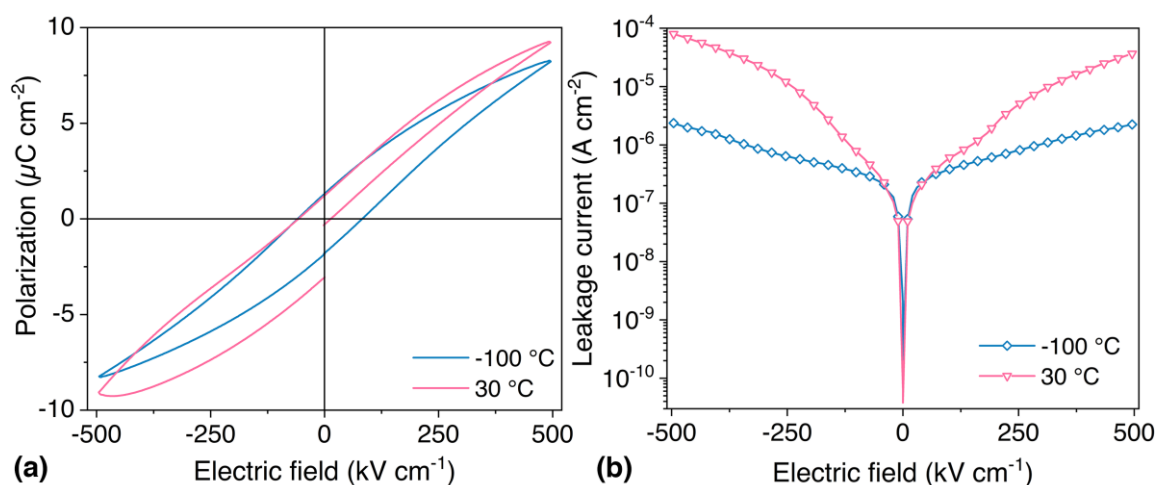
Figure 4.14 - Electric characterization of the 1 μm NBSBTO sample at -100 °C and at room temperature. (a) *P(E)* measurements; (b) leakage current measurement.

Finally, leakage current measurements were made to ascertain the effect of resistive contributions on reported polarization loops. For a temperature of -100 °C, currents in the order of roughly 10^{-6} A cm^{-2} were recorded. However, when the sample is tested at room-temperature, the values considerably rise. This is consistent with the temperature-dependent polarization loops exhibiting an increasing resistive contribution. Similar results were obtained with somewhat higher values for thinner NBSBTO films, indicating that leakage currents decrease with increasing thickness. The observed behavior might be explained by the samples' high defect density, which creates conducting pathways between the two electrodes. The significant surface roughness and porosity found at the surface and in cross-sections, in particular, may contribute to this resistive behavior. The columnar grain boundaries may exert an extra impact. Our results for polarization and leakage current are comparable to those reported in the literature [151], albeit at lower temperatures and with higher electric fields.

4.4. Chapter conclusions

By adjusting the deposition conditions, epitaxial NBTO-based thin films were produced on LSCO-buffered YAO and LAO substrates. The presence of

extra texture components in films grown on YAO implies that epitaxial growth of NBTO on these crystals occurs over a very restricted temperature range. In comparison, LAO substrates appear to be more suited, as just one epitaxial texture component was detected across the temperature range investigated. RSM measurements revealed a strained LSCO and a relaxed NBTO layer with an (001) orientation and an extra tetragonal distortion. Even for thin films, however, considerable roughness with protruding grains was found. Measurements of polarization hysteresis and leakage current revealed a low film resistivity, hindering future ferroelectric and dielectric investigations. NBSBTO films produced on LAO exhibited similar structural characteristics. Cross-sectional pictures indicated the presence of a columnar structure throughout the film thickness, but increasing thickness resulted in increased surface roughness and grain size. At -100 °C, electric field-dependent polarization loops showed ferroelectric activity with a maximum polarization of 8.3 µC cm^{-2} at 500 kV cm^{-1}. However, room-temperature experiments indicated a considerable resistive contribution to the polarization loops, preventing the ECE from being evaluated. In summary, while epitaxial development of NBTO-based thin films has been proven, additional microstructure tuning is necessary to minimize roughness and leakage currents at increased temperatures. Additional Mn doping or stoichiometric adjustments did not enhance these features.

5. Electrocaloric temperature changes in epitaxial Ba$_{1-x}$Sr$_x$TiO$_3$ thin films

The primary objective of chapter 5 is to examine the relationship between structural parameters and the electrocaloric impact in lead-free epitaxial Ba$_{1-x}$Sr$_x$TiO$_3$ (BSTO) thin film architectures. Thus, pulsed laser deposition was used to create BSTO thin films with Sr concentrations ranging from $x = 0$ to $x = 0.3$ on SrRuO$_3$ buffered SrTiO$_3$ single crystalline substrates. The resulting structural and electrical properties are discussed in the following.

5.1. Structural characterization

5.1.1. Influence of the Sr content

Based on the literature [190, 219], the effect of Sr concentration on the structural characteristics of BTO thin films was investigated. Figure 5.1(a) shows the XRD patterns of the resultant BSTO thin films with a thickness of roughly 200 nm for compositions ranging from $x = 0$ to $x = 0.3$. Both, the STO single crystal and the BSTO thin films exhibit narrow (00ℓ) peaks. Due to their comparable crystal structure and lattice parameter (STO: $a = 3.905$ Å; SRO: $a = 3.910$ Å), the SRO peaks are indistinguishable from the substrate peaks. The 2θ angle of the BSTO peaks increases as the Sr concentration increases, indicating a reduction in the out-of-plane lattice parameter from 4.06 Å for pure BTO to 4.02 Å for $x = 0.3$, as previously reported [175]. Additional texture measurements were taken to investigate the layers' in-plane alignment. Pole figures revealed a single texture component in all BSTO films, identical to the one presented in figure 5.1(b), which was obtained from the thickest film with $x = 0.3$. The fourfold symmetry of the (220) BSTO poles at 45° indicates that the SRO buffer transfers the orientation of the STO single crystal substrate to the ferroelectric layer, resulting in a cube-on-cube epitaxial relationship. Additionally, no twinning (i.e., no additional spots

in the pole figure due to a secondary texture component) was observed in thicker films, which is frequently found in pure BTO layers [190, 220].
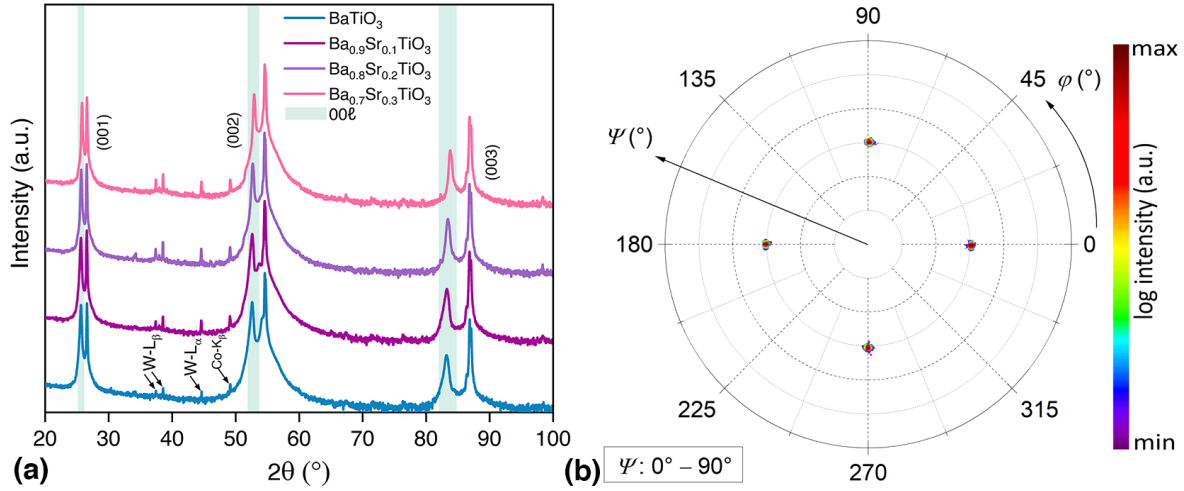
Figure 5.1 - Structural characterization of $Ba_{1-x}Sr_xTiO_3$ thin films: (a) θ-2θ scans in dependence of the Sr content for the deposited thin films, BSTO (00ℓ) peaks are marked with a green bar; (b) Pole figure of the (220) lattice planes for a BSTO epitaxial thin film (x = 0.3) having a thickness of about 680 nm.

To analyze the in-plane lattice parameters for all samples, detailed RSM measurements of the (103) and (-103) poles were performed. Figure 5.2 (a) illustrates such a map, in which all layers of the grown architecture are visible. Due to the limited thickness of the SRO buffer, the related peak is stretched along the Q_z axis, whereas a similar Q_x value as for the STO substrate peak suggests coherent growth, which is characteristic for SRO as typically a step-flow growth is observed [192, 221, 222]. In comparison, the BSTO layer exhibits different Q_x and Q_z values, indicating a relaxed growth state caused by the substantial lattice misfit toward the substrate (about 3 % for pure BTO and still 1.9 % for BSTO with x = 0.3). The BSTO (103) peaks are considerably widened in reciprocal space, which may be due to the layer's fine grain structure, strain, and/or mosaicity. Nonetheless, the lattice parameters may be calculated from the peak maxima; the results are given in figure 5.2 (b). As expected, the in-plane and out-of-plane lattice parameters are dependent on the Sr concentration. Without exception, all films exhibit a tetragonal distortion in contrast to the cubic structure of the bulk BSTO with x = 0.3 at room-temperature [175]. The difference between the in-plane and out-of-plane parameters remains almost constant; hence, the tetragonal distortion may be caused in part by the substrate and film having

differing thermal expansion coefficients during cooldown. The tetragonal distortion is similarly affected by oxygen concentration and Ba/Ti ratio. For films deposited at higher oxygen pressures, the in-plane lattice parameter is larger than the out-of-plane [223]. With regard to the Ba/Ti ratio, the tetragonal distortion is highest at Ba/Ti = 1, diminishes with increasing ratio, and is almost constant for Ba/Ti ratios ≥ 1.01 [224]. Unfortunately, it was not possible to determine the stoichiometry of the film with simple EDX measurements in the SEM as the substrate as well as the buffer containing Ti and Sr.
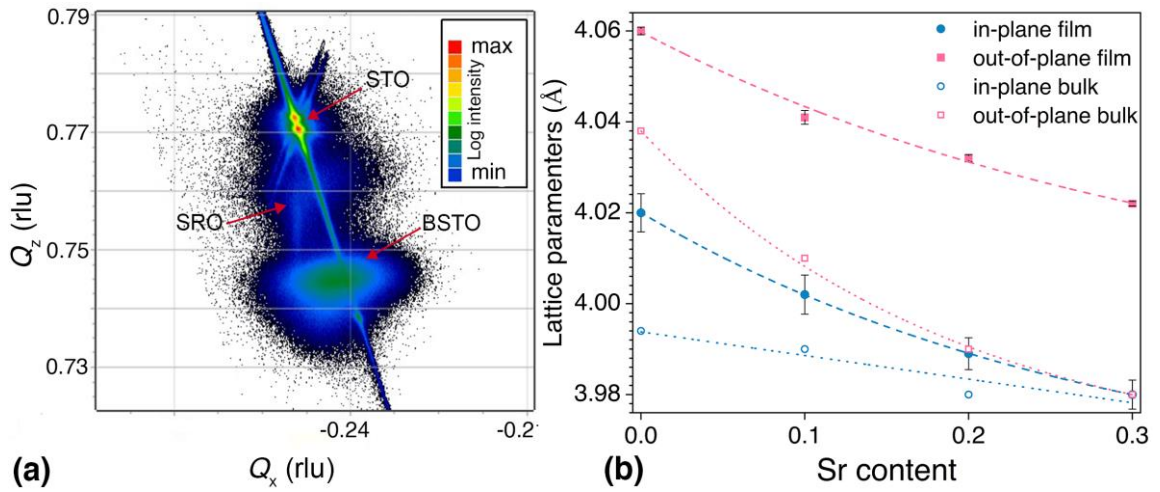
Figure 5.2 - Reciprocal space mapping and in-plane and out-of-plane lattice parameter of: (a) the (-103) peaks for a BSTO film (x = 0.1) on a STO/SRO substrate with 200 nm thickness; (b) In-plane and out-of-plane lattice parameters of about 200 nm thick BSTO thin films in dependence on the Sr content. The a and c lattice constant of bulk materials were added for comparison.

The influence of the film thickness on the structural characteristics of BSTO layers was studied by choosing the concentration x = 0.3 because it exhibits the highest ECE performance (maximum $|\Delta T|$ of 0.7 K at 50 °C for an E of 350 kV cm^{-1}) for the Sr doped layers (see section 5.7 (a)). To investigate the effect of this parameter on the structural and functional characteristics, films having a thickness of around 100 nm to 700 nm were deposited. In general, comparable characterization approaches to those described previously were used to study the crystal structure.
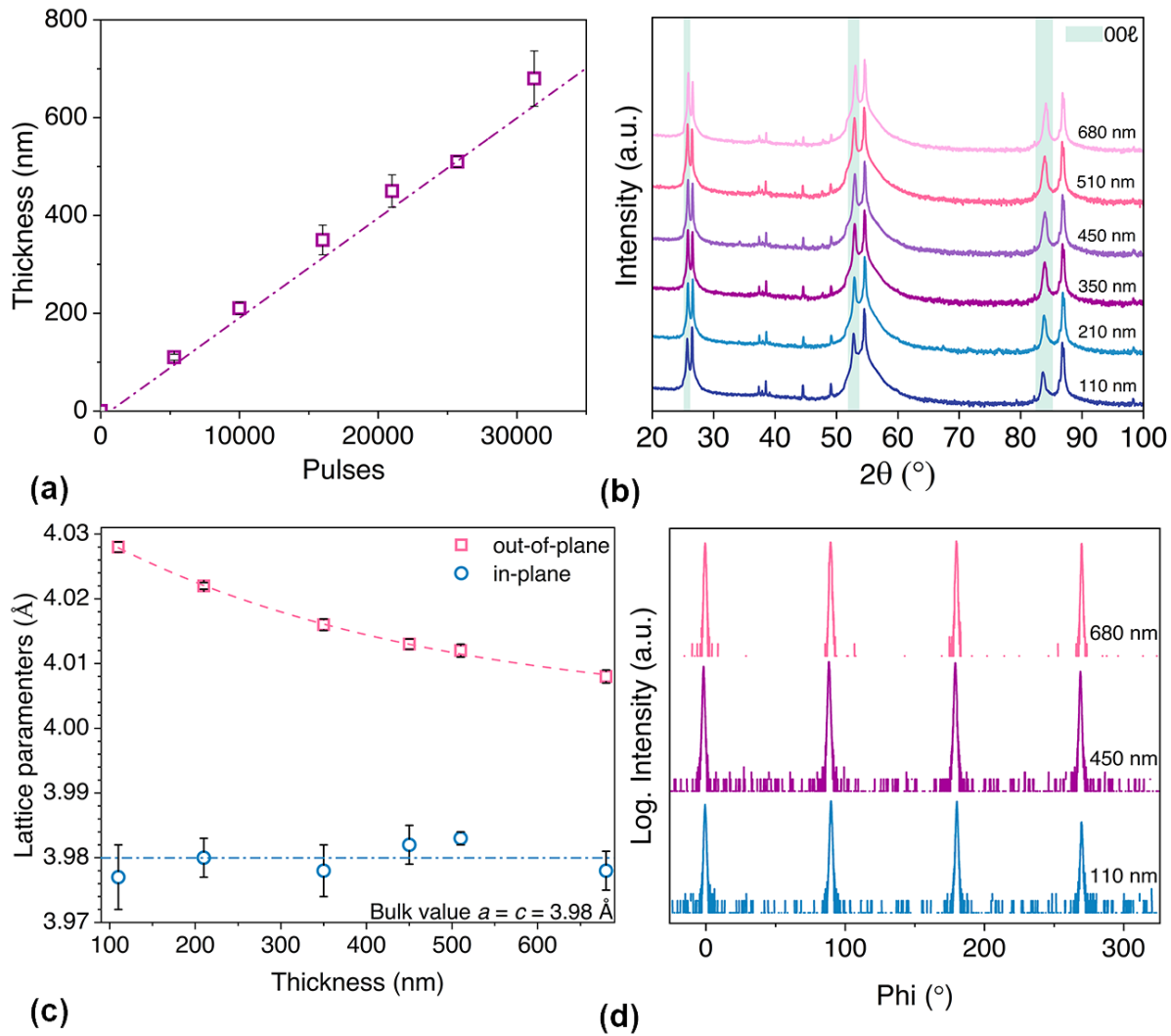
Figure 5.3 - Dependence of the structural properties on thickness for BSTO films with *x* = 0.3: (a) Influence of the thickness on the number of pulses; (b) *θ* - *2θ* scans; (c) in-plane and out-of-plane lattice parameters determined by RSM; (d) Phi-scans for 100 nm, 450 nm and 680 nm thick samples.

The relationship between the film thickness determined by FIB cuts and the number of pulses employed in the deposition is shown in figure 5.3 (a). The data indicate a linear dependence of thickness on the number of pulses. This implies a steady deposition rate at all times, which is in contrast to the deposition of NBTO-based thin films. Standard XRD (figure 5.3 (b)) analysis finds distinct (00ℓ) peaks in all samples with a slight *2θ* angle shift to higher values, suggesting that the out-of-plane lattice parameter decreases with increasing thickness. Pole figure measurements (not shown, compare figure 5.1(b) for the thickest layer) reveal that all samples exhibit an undisturbed epitaxial growth. The in-plane and

74

out-of-plane lattice parameters were determined again using RSM; the results are presented in figure 5.3 (c). While the in-plane lattice parameter does not vary much with sample thickness, the out-of-plane lattice parameter exhibits a distinct trend. As a result, the tetragonal distortion decreases as the thickness increases. In general, this variation of the in-plane and out-of-plain lattice parameters might result from the clamping of the ferroelectric layer to the substrate. With increasing Sr content, the unit cell presents a more relaxed state. Again, no twinning is seen even at the thickest layer, indicating that the oxygen background pressure employed is appropriate for the epitaxial growth of BSTO thin films. Figure 5.3 (d) presents phi-scans of three selected samples, whereas table 5.1 summarizes the FWHM values for all measured layers and the in-plane and out-of-plane lattice parameters:

Table 5.1 - FWHM values and in-plane and out-of-plane lattice parameters for BSTO with x = 0.3 thin films with distinctive thickness.

Thickness (nm)	FWHM (°)	In-plane (Å)	Out-of-plane (Å)
110	1.01 ± 0.1	3.977	4.028
210	1.05 ± 0.1	3.98	4.022
350	1.0 ± 0.1	3.978	4.016
450	0.93 ± 0.1	3.982	4.013
510	1.06 ± 0.1	3.983	4.012
680	0.99 ± 0.1	3.978	4.008

Atomic force microscopy with a scan size of 4 µm^2 was used to study the surface morphology of the thin films with a thickness of 200 nm. The results are presented in figure 5.4. The smooth surface of the 200 nm thick BTO film is interrupted by a number of small protruding grains with an average grain size of around 80 nm and a height of about 5 nm. This results in a root mean square (rms) of 1.2 nm, which is consistent with previously reported data [190, 219]. When Ba is substituted for Sr, the protruding grains becomes smaller, resulting in a film structure with visible terraces and a decreased rms value. Whereas for

BSTO (x = 0.1), some extra grains are discernible, resulting in a rms value of around 1 nm, the roughness of BSTO with $x > 0.1$ falls significantly to values < 0.25 nm, with a rms of 0.19 nm for the BSTO (x = 0.2) thin films and 0.18 nm for the BSTO with x = 0.3 films.
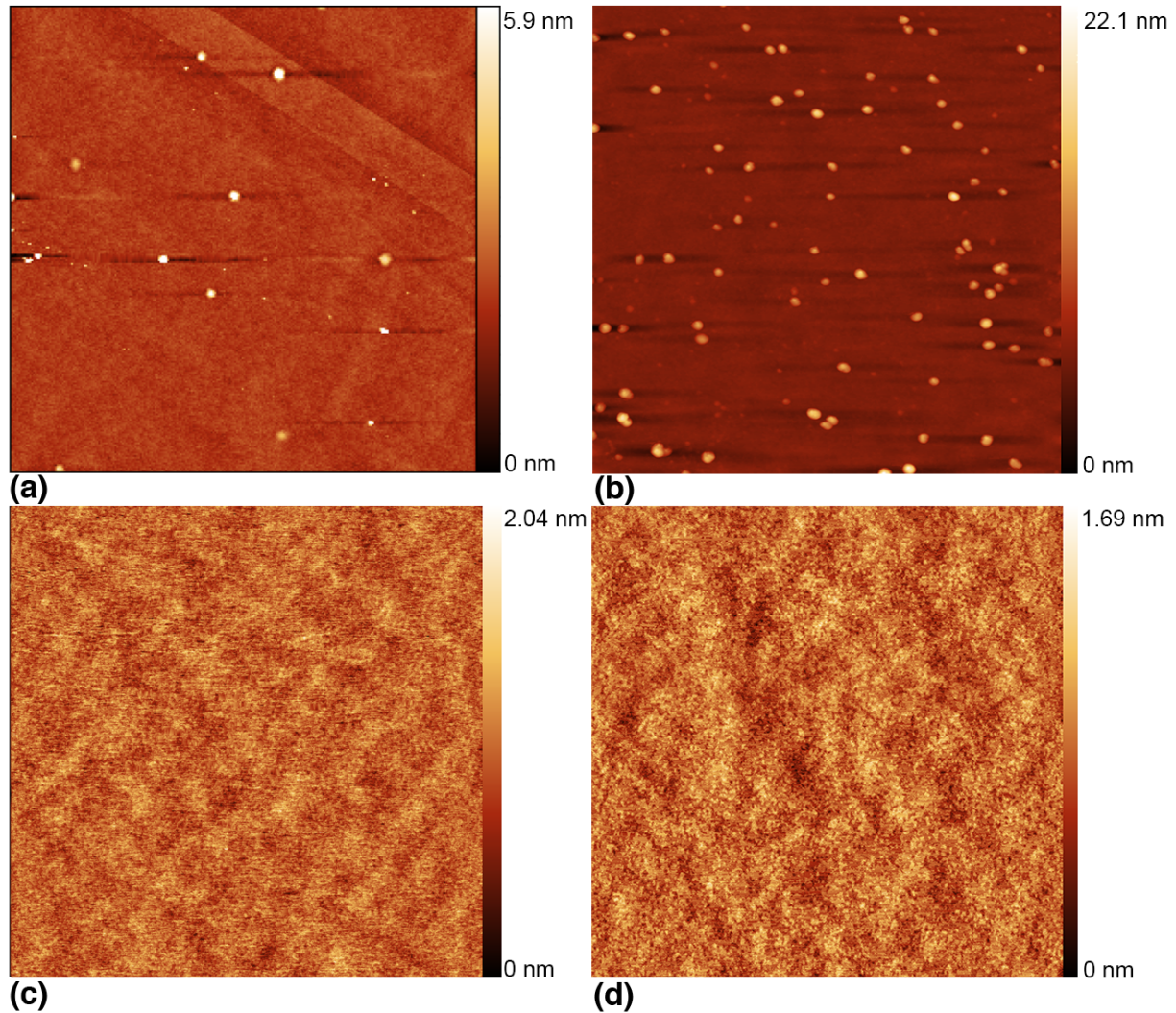
Figure 5.4 - Analysis of the surface roughness by AFM (size 2 µm × 2 µm) for BSTO films with different Sr contents: (a) pure BTO; (b) x = 0.1; (c) x = 0.2; (d) x = 0.3.

For all thicknesses of the BSTO layers with x = 0.3, smooth films with a terrace-like microstructure were found (figure 5.5 for a BSTO thin film with 110 nm (a) and 680 nm (b)). Terraces of this type may develop on the STO substrate and are replicated on the film surface as a result of layer-by-layer or step-flow growth. The overall morphology of BSTO films was determined using SEM images of cross-sections (figure 5.5 (c)). All samples have a dense structure, no visible columnar structures (in contrast to the NBTO samples in figure 4.10), and

a clean interface transition in all layers. Figure 5.5 (d) summarizes the sample roughness at all thicknesses. Each sample has a very smooth surface, with a rms difference of only 0.12 nm across a thickness range of around 600 nm. As a result, there is a significantly lower rms value, as presented by Zhou et al. [225], who deposited comparable BSTO layers using PLD on a $(LaAlO_3)_{0.3}(Sr_2AlTaO_6)_{0.7}$ (LSAT) single crystal substrate with a greater lattice misfit. The same can be seen for Zr containing thin films, having a rms ≤ 1 nm [219].
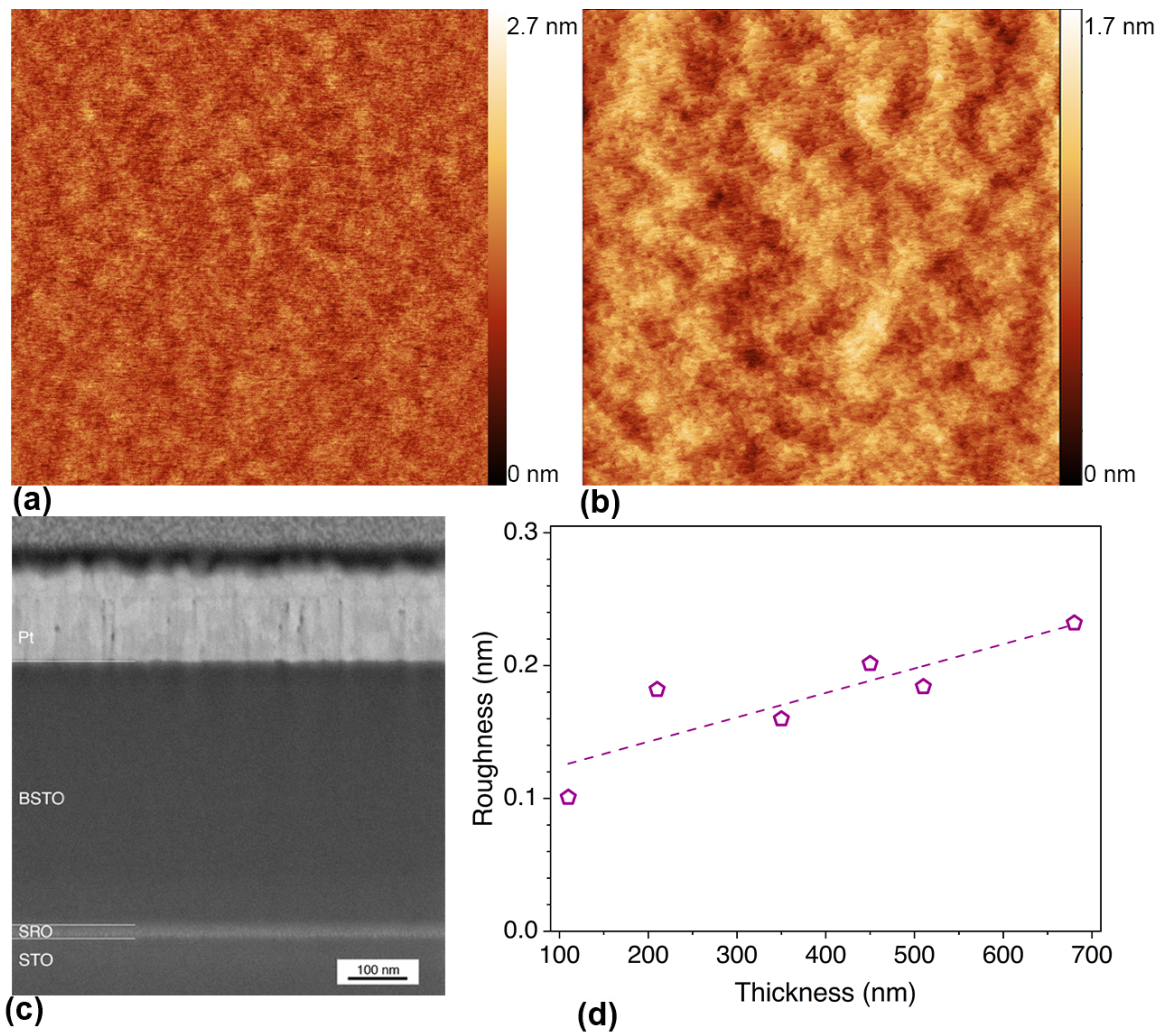
Figure 5.5 - Analysis of the surface roughness by AFM (size 2 μm × 2 μm) and layer structure by FIB: (a) AFM image of the 110 nm thick BSTO film; (b) AFM image of the 680 nm thick BSTO film; (c) Cross-section of a BSTO thin film with $x = 0.3$ having an approximate thickness of 440 nm; (d) Influence of thickness on the surface roughness for all studied films.

5.2. Electrical characterization

The study's primary objective was to evaluate the electrocaloric performance of the chosen materials. As a result, a thorough electrical characterization of BSTO films with varying Sr concentrations and film thicknesses was conducted. The permittivity (ε_r) as a function of temperature was analyzed at frequencies ranging from 100 Hz to 100 kHz in order to study the phase transition of the deposited thin films. Figure 5.6 (a) and (c) summarizes the results for the dependence of the permittivity on temperature for different Sr content and thickness for BSTO with $x = 0.3$, respectively. For proper ferroelectric materials, it is expected that ε_r will exhibit a local maximum near a phase transition. However, a large peak is apparent in all measurements, which is characteristic of diffuse phase transitions. Additionally, when the frequency increases, the temperature of maximum permittivity (T_m) increases, which is a feature of relaxor ferroelectrics (figure 5.6 (e)). Finally, larger ε_r values are obtained for lower frequencies, and a minor tan δ loss increase with temperature, which is consistent with previous work on BSTO ceramics [27, 180].
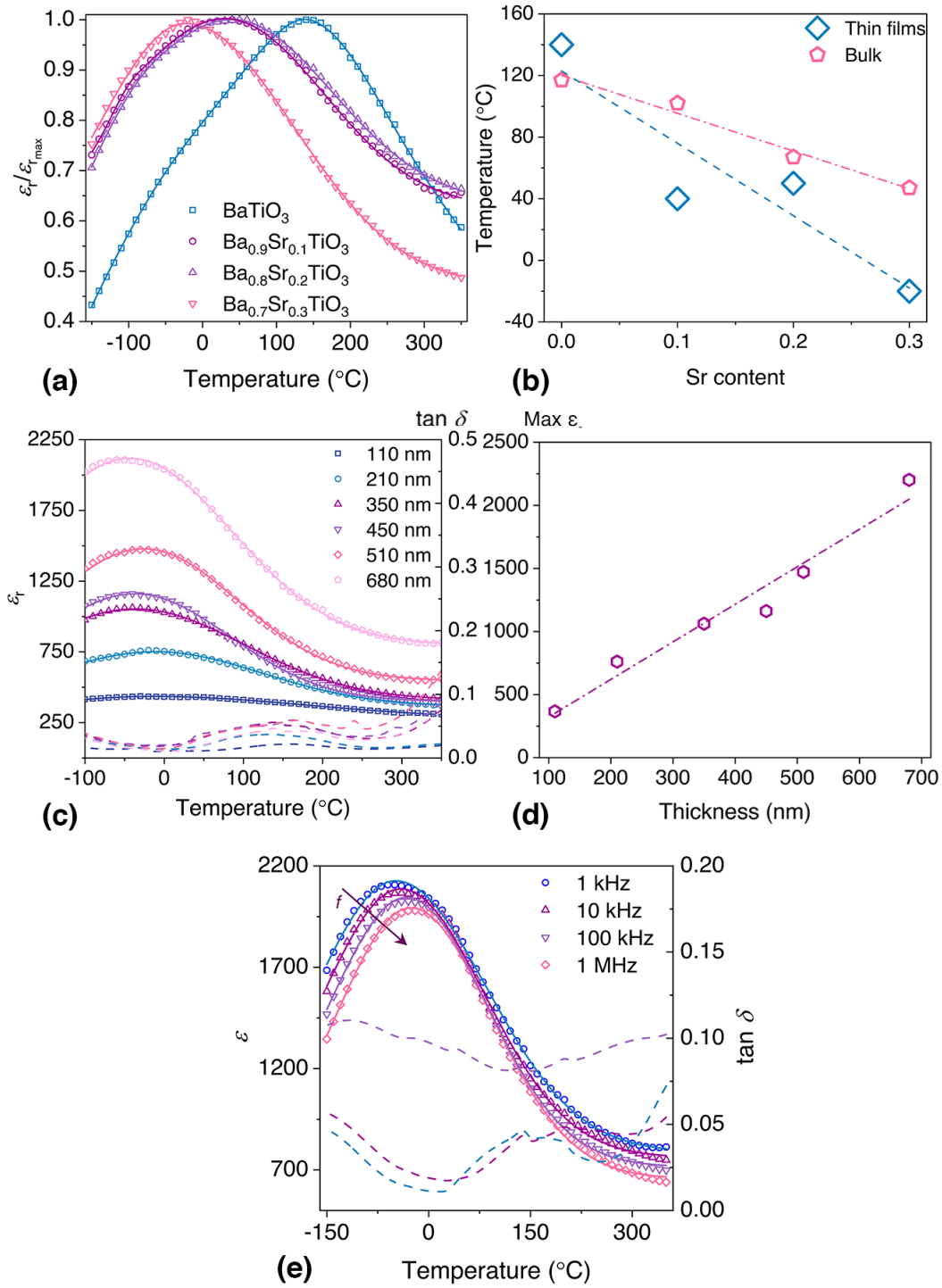
Figure 5.6 - Study of the permittivity on BSTO samples by Sr content and sample thickness: (a) Normalized relative permittivity ε_r vs temperature measured at 1 kHz for about 200 nm thick BSTO films with different Sr content; (b) Temperature of maximum permittivity vs Sr concentration for the samples in comparison to bulk values [170]; (c) Relative permittivity ε_r and loss tan δ vs temperature measured at 1 kHz for $Ba_{0.7}Sr_{0.3}TiO_3$ samples with different thickness; (d) Linear correlation between the maximum value of permittivity and sample thickness; (e) Influence of the frequency on the temperature of maximum permittivity for the sample with a thickness of 680 nm.

Figure 5.6 (a) depicts the permittivity dependency on Sr content for BSTO films with a thickness of roughly 200 nm. Since the measured maximum permittivity of Sr-doped samples is lower than that of pure BTO sample ($\varepsilon_r \approx 1900$ F m^{-1}), the values were normalized to make comparisons easier. As already mentioned, there is only one broad single peak evident for all BSTO concentrations, indicating a diffuse phase transition. Such behavior could be caused by substrate clamping [219]. A second phase transition as observed for bulk ceramics might explain the additional shoulder at lower temperatures for the BTO layer and the BSTO films with low Sr concentration. As shown in figure 5.6 (b), T_m decreases with increasing Sr content from about 140°C for pure BTO to nearly identical values for $x = 0.1$ and $x = 0.2$, and a value of about -20 °C for $x = 0.3$. As described in chapter 2, T_C decreases with Sr content also in bulk BSTO ceramics [27, 180], which is explained by a volume change in the BSTO unit cell due to the introduction of Sr content [226]. Similar to their bulk equivalents, a decrease in T_C was reported for BSTO films with increasing Sr content [170, 227]. Although the temperature of maximum permittivity drops with increasing Sr concentration for both thin films and bulk, the decrease is smaller for bulk [170] while the difference is fairly large when compared with the results obtained for thin films, presented in this study. Figure 5.6 (c) indicates how the permittivity ε_r increases with thickness for BSTO samples with $x = 0.3$. With increasing film thickness, all samples show again a broad peak with a maximum that shifts slightly to lower temperatures. The dependence of the maximum permittivity on the sample thickness is plotted in figure 5.6 (d) and shows an almost linear correlation for the range studied. Different groups found a similar thickness dependence for BSTO thin films [228-230]. Such scaling effects can have a variety of causes, although they are most commonly described in relation to electrical and mechanical boundary conditions, as well as grain size changes [231, 232]. On the one hand, inactive "dead" layers near the electrodes have a smaller impact on the dielectric characteristics of thicker films. Mechanical boundary conditions, on the other hand, result in compressive tension owing to clamping on the STO substrate, which may be alleviated in thicker layers due to relaxation effects. Figure 5.6 (e) shows the influence of frequency on T_m of the BSTO thin film with a thickness of 680 nm. The increase of T_m with frequency is

characteristic of a relaxor ferroelectric as well as the reduction of the maximum of permittivity.
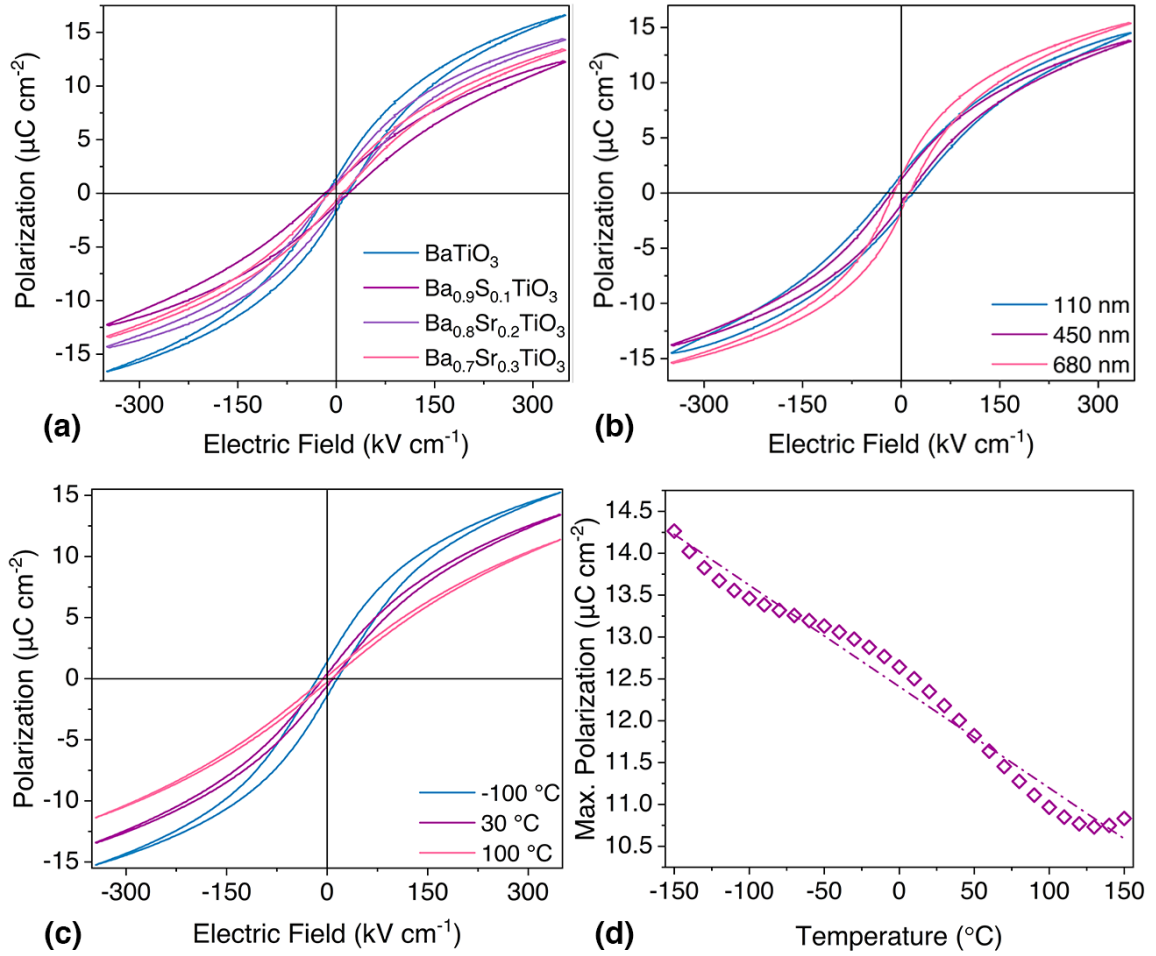
Figure 5.7 - Polarization hysteresis of BSTO films in dependence of: (a) Sr content at room temperature; (b) film thickness for samples with *x* = 0.3; (c) temperature for a 200 nm thick sample with *x* = 0.3; (d) Dependence of the maximum polarization at 350 kV cm^{-1} on temperature for a 210 nm thin film with *x* = 0.3.

Figure 5.7 shows the results of selected polarization measurements obtained for films with different Sr concentrations, measurement temperatures, and sample thicknesses, respectively. The values of the coercive field and the remanent polarization are summarized in table 5.2:

Table 5.2 - Remanent polarization, coercive field, and maximum of polarization for BSTO thin films with different Sr concentrations (200 nm thick), different temperatures (x = 0.3, 200 nm thick) and film thickness (x = 0.3) at 350 kV cm^{-1}.

	Remanent polarization (µC cm^{-2})	Coercive field (kV cm^{-1})	Max. Polarization (µC cm^{-2})
Sr content			
BTO	1.4	13.3	16.6
BSTO 90/10	0.9	17.8	12.3
BSTO 80/20	1.0	11.0	14.4
BSTO 70/30	0.7	11.0	13.4
Thickness (nm)			
110	1.6	21.3	14.5
210	0.4	6.9	13.4
350	0.6	6.5	14.1
450	1.0	12.6	13.8
510	1.1	14.1	13.9
680	1.1	8.8	15.4
Temperature (°C)			
-100	1.4	14.3	15.2
30	0.4	6.9	13.4
100	0.2	5.1	11.4

The polarization hysteresis loops (figure 5.7 (a) to (c)) display the characteristics of a thin ferroelectric relaxor film with a slim s-shaped form [231]. The maximum polarization diminishes with increasing Sr content (figure 5.7 (a)), as well as the remanent polarization and the coercive field (table 5.2). This phenomenon might be explained by the change in the grain size, densification,

and morphology of Sr-containing ceramics [233, 234]. Additionally, the ferroelectric transition temperature comes closer to room-temperature, with increasing Sr content, which leads to a reduced polarization. The results obtained for the polarization at different film thicknesses are shown in figure 5. 7 (b) and are consistent with the theoretical study of Ban et al. [235]. It was stated in their publication that considering the compressive nature of a STO substrate, the polarization of BSTO with x = 0.3 should decrease with increasing sample thickness due to the relaxation of compressive stresses caused by misfit dislocations associated with the increasing thickness. This decrease in polarization would be more accentuated for thinner samples and gradually become constant with increasing thickness. The remanent polarization and the coercive field decrease with increasing film thickness, presenting lower values on the samples with 210 nm and 350 nm. The change in polarization for varying temperatures is seen in figure 5.7 (c) for a 200 nm thick film. The polarization rises as the temperature decreases, which is expected from the standard $P(T)$ phase diagram indicating that an increasing temperature eventually destroys the ordered arrangement of the permanent dipoles, which is similar to the results of other groups [27, 178]. Simultaneously, the hysteresis loop grows narrower, suggesting that the films are gradually transitioning from the ferroelectric to the paraelectric phase [27]. Here, the remanent polarization and the coercive field decrease with increasing temperature. The maximum polarization in dependence on temperature is shown in figure 5.7 (d) for a sample of 210 nm. As expected, it shows a decrease in the maximum polarization with increasing temperature.

5.3. Electrocaloric characterization

In the final step, the indirect method based on Maxwell relations [132] was used to analyze the adiabatic temperature change $|\Delta T|$ due to the ECE effect. Using a 350 kV cm^{-1} applied electric field as a starting value, the $P(E, T)$ dependence during field removal, which corresponds to the positive upper branch of the polarization hysteresis loop, was determined. $P(E)$ loops were measured with a 10 K step size from 150 °C to -150 °C to reduce the impact of fatigue. Polarization and hysteresis decrease with increasing temperature for all samples, regardless of the applied electric field (compare figure 5.7 (a)). After that, the $P(E)$

measurements at constant temperatures were used to receive *P(T)* curves for various electric fields.

As proposed by Mischenko et al [18], $\partial P/\partial T$ values were computed using fourth-order polynomial fits of these *P(T)* data to be applied for the calculation of |ΔT| according to equation 2.4. The evaluation employed an increasing heat capacity $c_p(T)$ with values ranging from 2.1 J m^{-3} K^{-1} at -100 °C to 3.05 J m^{-3} K^{-1} at 120 °C. These values were determined from polycrystalline BTO film by $c_p(T)$ measurements [202], with anomalies at T_C omitted. At the same time, any effect of the electric field on the specific heat was ignored. As the BTO and BSTO thin films studied here have a diffuse phase transition, this simplification is feasible. No peak-like anomalies were identified in $c_p(E = 0, T)$ data for similar epitaxial BTO thin films over the temperature range from room-temperature to 550 K [236]. Strukov et al. studied $c_p(E = 0, T)$ for different thicknesses of polycrystalline BTO films and discovered that anomalies in the specific heat at T_C are less noticeable in thinner films [202]. As a result, if $c_p(E = 0, T)$ only has a diffuse maximum around T_m, the further broadening of the specific heat maximum with an increased electric field will be less meaningful. Despite modest changes in the density of BSTO with increasing Sr concentration, a comparable $c_p(T)$ dependence was assumed in the computations for all film compositions for simplicity. Although the assumptions made above may cause some uncertainty in the resulting |ΔT| values, we believe they are a reasonable approximation for estimating the electrocaloric response.
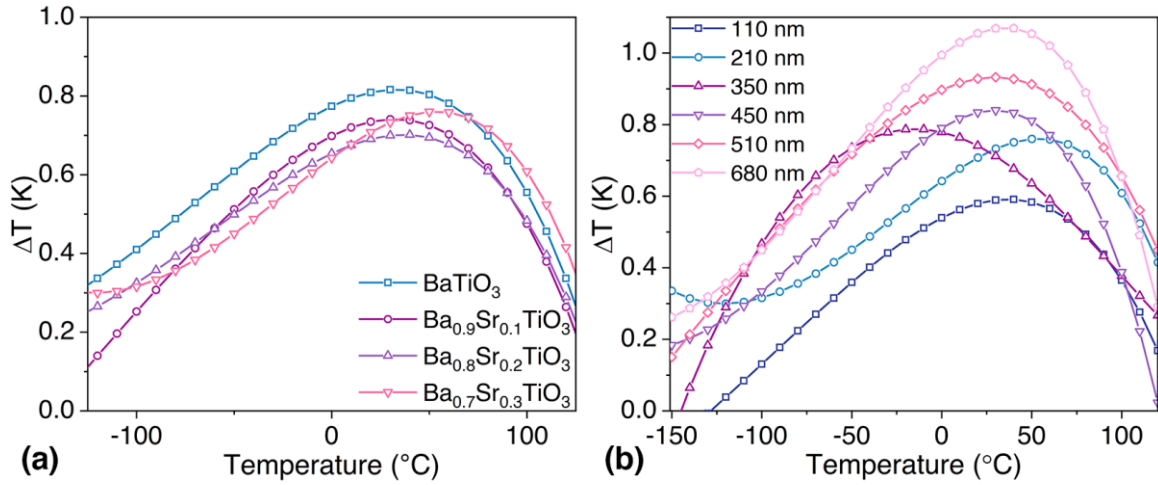
Figure 5.8 - Adiabatic temperature change of BTO and BSTO thin films: (a) Dependence of $|\Delta T|$ on the temperature for the different Sr concentrations for a ΔE of 350 kV cm^{-1}; (b) $|\Delta T|$ dependence of BSTO with $x = 0.3$ for the different film's thicknesses using ΔE of 350 kV cm^{-1}.

Figures 5.8 (a) and (b) show the estimated temperature changes for different Sr concentrations and film thicknesses as a function of temperature. A broad $|\Delta T|$ maximum was found for all samples, as expected for second-order or diffuse phase transitions [14, 236]. Peak values between 30 °C and 50 °C were found in most films, with no clear dependence on Sr concentration or sample thickness. Furthermore, no apparent relationship between the $|\Delta T|$ curves and the temperature dependence of $\varepsilon_r(T)$ was discovered. The pure BTO film has the highest $|\Delta T|$ of around 0.8 K in comparison to the Sr-containing samples (figure 5.8 (a)) when an electric field of 350 kV cm^{-1} is applied; nevertheless, the differences are minor. They might be connected to the phase transition itself, i.e. a more diffuse transition with a higher Sr content resulting in a lower $|\Delta T/\Delta E|$ value [21, 236], as demonstrated by the widened $\varepsilon_r(T)$ dependency (see figure 5.6 (a)). BSTO ceramics with comparable Sr concentrations exhibited similar behavior [27, 179, 180]. The ECE response of the BSTO film with $x = 0.3$ is equivalent to that of the pure BTO film. At the same time, as previously mentioned, the surface roughness has considerably decreased. As a result, we focused on this composition for a thorough examination of the effects of film thickness (figure 5.8 (b)) and electrical field strength (figure 5.9 (a)) on ECE characteristics. Under a 350 kV cm^{-1} electric field, the temperature change $|\Delta T|$ rises with increasing thickness, reaching approximately 1.1 K for the 680 nm thick

film. The increased $|\Delta T|$ with increasing thickness might be owing to the clamping effect [237], which has a smaller impact as thickness increases, but it could also be due to a potential change in the strain state [238], where a changing c/a ratio plays a role.
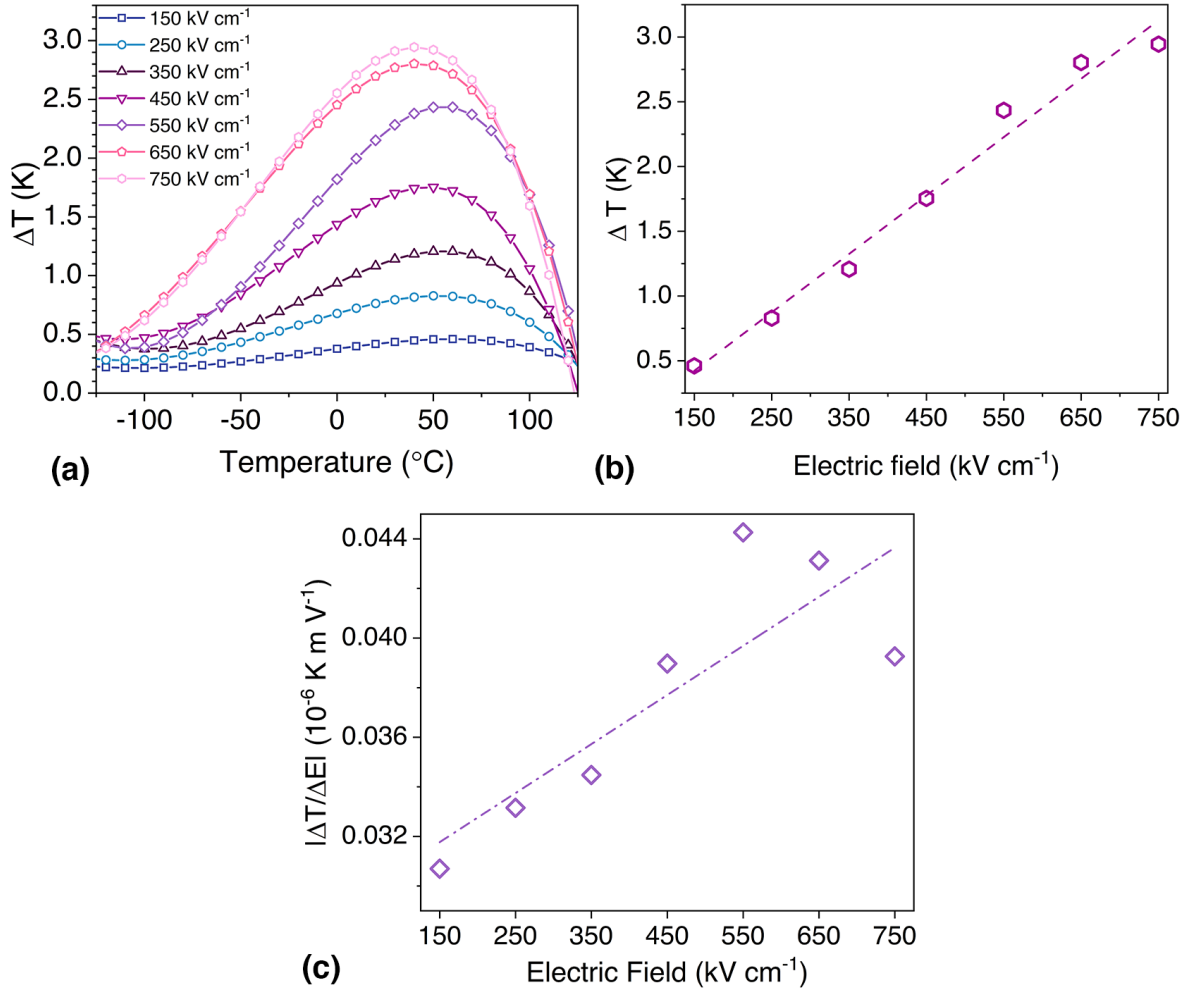
Figure 5.9 - Adiabatic temperature change of *x* = 0.3 film: (a) $|\Delta T|$ in dependence on the applied electric field; (b) Linear correlation between the applied electric field and the adiabatic variation of temperature regarding film thickness; (c) dependence of the magnitude of the electrocaloric effect on the applied electric field.

Figure 5.9 (a) shows how greater electric fields were used to achieve larger temperature changes for the same material. In this scenario, $|\Delta T|$ grows with the applied electrical field (figure 5.9 (b)), reaching a maximum of 2.9 K for E = 750 kV cm^{-1}, equivalent to an ECE strength ($|\Delta T/\Delta E|$) of 0.04 × 10^{-6} K m V^{-1} as seen in figure 5.9 (c).

BTO is widely used for electrocaloric characterization. Pure bulk BTO single crystal showed a $|\Delta T|$ of 0.9 K at a temperature of 129 °C for an applied electric field of 12 kV cm^{-1} [21] via the direct method. Bai et al. [20], using a direct calorimetric measurement on a multilayer thick film, determined a $|\Delta T|$ of 7.1 K at 80 °C for an electric field of 800 kV cm^{-1}. Regarding the ECE in BTO thin films, Wang et al. [239] revealed a $|\Delta T|$ of 0.75 K at 97 °C, for a 300 nm thick film, under an applied electric field of 217 kV cm^{-1}, using the indirect method. Comparatively, a $|\Delta T|$ of 0.8 K under 350 kV cm^{-1} was found in this work for a 200 nm thick BTO film at room-temperature. Sanlialp et al. [133] reported results of a direct ECE measurement on BTO with Zr doping using a modified differential calorimeter, getting $|\Delta T|$ values of 0.54 K at 80 °C and 0.34 K at 33 °C under an electric field of 20 kV cm^{-1} for bulk $Ba(Zr_{0.2}TiO_{0.8})O_3$ and $Ba(Zr_{0.12}Ti_{0.88})O_3$, respectively. Furthermore, Engelhardt et al. [219] observed with the indirect method a $|\Delta T|$ of 0.3 K at 150 °C for epitaxial $Ba(Zr_{0.2}TiO_{0.8})O_3$ thin films under an electric field of 170 kV cm^{-1}.

For $Ba_{1-x}Sr_xTiO_3$ bulk materials, a $|\Delta T|$ of 0.39 K at 76 °C has been shown by Bai et al. [179] for $x = 0.2$ under an applied electrical field of 20 kV cm^{-1} using the indirect method. In the same article, a maximum $|\Delta T|$ of 0.36 K was found for $x = 0.3$ at ambient temperature. As previously stated in chapter 2.10, the ferroelectric phase transition occurs at room-temperature for $x = 0.3$. Giving that significant entropy changes are found close to the phase transition temperature [178], which leads to large $|\Delta T|$, this finding confirms that the ferroelectric phase transition occurs near room-temperature when $x = 0.3$. Using the direct method, this author demonstrated a $|\Delta T|$ of 0.16 K at 33 °C and 0.18 K at 25 °C for $x = 0.3$ and $x = 0.35$, respectively. These results were obtained under an electric field of 10 kV cm^{-1}. Concerning thin films, Lisenkov et al. [182] simulated the intrinsic ECE in $Ba_{0.5}Sr_{0.5}TiO_3$. A $|\Delta T|$ of 17 K was reported at a temperature of -23 °C, in this case, while considering that an electric field of 500 kV cm^{-1} was applied. Liu [178] calculated the adiabatic variation of temperature by the indirect method for $0.1 \le x \le 0.3$. under 350 kV cm^{-1}. Contrary to the results presented in this work, the obtained $|\Delta T|$ decreases with increasing Sr content. For samples with a thickness of 300 nm, a $|\Delta T|$ of 1.9 K, 1.75 K, and 1.56 K, for $x = 0.1$, $x = 0.2$, and

$x = 0.3$, respectively, was calculated. As expected, the temperature where $|\Delta T|$ is maximum also decreases with increasing Sr content as expected.

5.4. Chapter conclusions

PLD was used to successfully prepare epitaxial BTO and $Ba_{1-x}Sr_xTiO_3$ thin films with varying thicknesses on STO substrates. The crystal structure of all layers was tetragonal for all compositions, with decreasing lattice constants as Sr concentration increased. The layers' surfaces are smooth with low roughness values and evidence of layer-by-layer or step flow development in the form of terrace-like steps. Electric measurements indicate that at lower temperatures, there are fewer leakage currents and higher maximum polarization values. Generally, the polarization hysteresis loops of BSTO films get smaller as the temperature increases, indicating a relaxor-like behavior. Permittivity measurements for all samples reveal wide peaks with a decreasing temperature of maximum permittivity as Sr concentration increases, indicating a diffuse phase transition. Due to the reduced impact of electrical and mechanical boundary conditions, thicker films result in greater permittivity values. At 350 kV cm^{-1}, the adiabatic temperature change is not greatly affected by Sr concentration but increases significantly with increasing layer thickness. At an applied electric field of 750 kV cm^{-1}, a $|\Delta T|$ value of 2.9 K was obtained for a 680 nm thick BSTO layer with $x = 0.3$, demonstrating the feasibility of such materials for more thorough electrocaloric investigations.

6. Conclusions

The major aim of this research was to investigate the relationship between an epitaxial thin film microstructure and the electrocaloric effect. Two lead-free ferroelectric materials were studied in this work. $Na_{0.5}Bi_{0.5}TiO_3$-based thin films were grown on different substrates and deposition conditions to test their feasibility for electrocaloric studies. Epitaxial $Ba_{1-x}Sr_xTiO_3$ thin films with different Sr contents were deposited on STO substrates to study their electrocaloric performance. Various characterization methods were used to investigate the crystal structure and morphology, whereas permittivity, polarization, and leakage current were measured to estimate the electrocaloric properties.

Using stoichiometric targets, NBTO layers were grown with pulsed laser deposition on LSCO-buffered (001)-oriented YAO, LAO, and STO single crystals. Comparing the different films, a substantial influence of the substrate on growth was observed. On STO, the NBTO peak is scarcely discernible with XRD due to an almost identical c lattice parameter. The NBTO layer grown on YAO exhibits a minor (110) peak, while the layer formed on LAO exhibits only (00ℓ) peaks. Subsequently, the deposition temperature was optimized for epitaxial growth of the NBTO layer on LAO and YAO. On YAO, an epitaxial growth was only found at 600 °C, whereas an additional (110) oriented texture component was found in NBTO at 550 °C as well as at 650 °C. In contrast, epitaxial growth was observed on LAO at all deposition temperatures studied.

All YAO and LAO films had a larger out-of-plane lattice constant than the target, implying a tetragonal distortion. Texture analysis revealed fourfold symmetry of the NBTO (110) peak, indicating that the orientation was transmitted epitaxially from the substrate to the functional layer. Whereas no additional peaks were observed in the pole figure for the films on LAO, only the layer deposited at 600 °C exhibits an undisturbed epitaxial growth on YAO. The RSM analysis showed that the LSCO buffer, as well as the NBTO layer, are grown in a relaxed state on YAO due to the significant lattice mismatch. In contrast, the LSCO buffer layer is strained on LAO because of a relatively small misfit of about 1.3 %, whereas the NBTO layer is also relaxed in this case. As a result, the surface of the LSCO buffer might have a significantly higher defect density on YAO if

compared with the layer on LAO. This in turn might have an influence on the NBTO nucleation, resulting in a larger temperature range for epitaxial growth on LAO. AFM scans of NBTO films deposited on YAO showed a heterogeneous surface with high roughness decreasing with increasing deposition temperature and a high density of small grains. In comparison, the samples on LAO had a lower roughness but increased with higher deposition temperatures. Nevertheless, a heterogeneous morphology with small grains aggregating into conglomerates and the presence of pores was noticeable in higher-resolution AFM scans. Cross-sectional scans revealed the presence of columnar structures in the NBTO layer that extend over the whole layer thickness. Also here, the presence of pores was visible throughout the thickness of the layer. Adding an excess of Bi_2O_3 and Na_2CO_3 and doping with MnO_2 to the target material did not disturb the epitaxial growth on LAO using the same deposition conditions as for the pure NBTO layer. Compared to NBTO, a smaller tetragonal distortion was obtained, but roughness and porosity remained similar.

Using a modified NBSBTO target and similar deposition conditions, additional films were prepared. The XRD patterns of the samples mostly exhibit (00ℓ) peaks at all temperatures, indicating that Ba and Sr were integrated into the NBTO crystal structure during the deposition process since no separate NBTO and STO phase peaks are visible. Texture measurements confirm the epitaxial growth of the NBSBTO layer. Additionally, the influence of film thickness was examined. As thickness increases, a shift to a lower 2θ is noticeable, resulting in a slight rise in the out-of-plane lattice parameters. Films prepared with a higher deposition rate and a thickness of about 1 µm revealed an additional (110) peak in the XRD scans. RSM investigations confirmed that the unit cell is tetragonally deformed at all temperatures and thicknesses. Cross-section scans indicated a dense structure with columnar grains and pores extending the whole thickness of the film. Increased sample thickness results in an increased surface roughness and particle size. The addition of Bi_2O_3 and Na_2CO_3, revealed a slight variation of the tetragonal distortion when compared with pure NBSBTO. Nonetheless, only (00ℓ) peaks were found hinting at an epitaxial growth, which was confirmed by texture measurements. Cross-section SEM revealed a layer filled with pores and suggested a rough surface that was confirmed by AFM scans.

Polarization measurements on the pure NBTO film exhibited an asymmetrical hysteresis loop up to a field of 375 kV cm^{-1}, but no clear ferroelectric behavior. Leakage current measurements revealed large leakage currents for both polarities, with the negative branch exhibiting the most leakage. This is likely a result of the high surface roughness, the existence of pores, and the presence of many defects, such as oxygen vacancies.

The permittivity of NBSBTO films was determined using temperature-dependent dielectric tests and compared to bulk material processed identically. The permittivity values were found to be significantly lower than the values of the bulk counterpart [217]. At low temperatures, tan δ is frequency-dependent, similarly to bulk; however, tan δ is significantly higher than the bulk equivalent. This might suggest that the depolarization temperature has decreased, either because of the tetragonal distortion or as a result of stoichiometric alterations. Due to the substantial resistive contribution of leakage current, no clear conclusion about the permittivity of the NBSBTO thin films can be drawn. The change of deposition conditions, mainly oxygen pressure and substrate temperature during deposition, might help to address such a high resistive contribution.

The influence of temperature on the electric field-dependent polarization was examined to determine the NBSBTO thin films' ferroelectric properties. An asymmetrical hysteresis loop was measured at ambient temperature. Apart from the large losses, which were primarily found on the negative branch, the sample exhibits ferroelectric behavior, which is more pronounced at lower temperatures. At the same time, leakage measurements reveal significantly lower leakage currents if compared with undoped NBTO films.

In summary, while epitaxial growth was achieved for NBTO-based thin films, the high surface roughness and defect density prohibited electrocaloric investigations on the grown films mainly due to high leakage currents at ambient temperatures. Therefore, significant modifications of the deposition parameters are required to optimize the microstructure, i.e. to decrease roughness and leakage currents at elevated temperatures. Unfortunately, the first test with additional doping of Mn or stoichiometric modifications had no effect on these properties. Despite the ECE was already proven in bulk NBTO-based materials [36, 66, 70, 161, 163], no electrocaloric investigation on thin films was possible in

this study. Nonetheless, the contribution of this study to the epitaxial growth of NBTO-based thin films is linked to the influence of substrate and deposition parameters. The optimization of these parameters, namely background oxygen pressure, laser fluence, and deposition rate may enable epitaxial growth to occur over a broader temperature range and help improve the electrical properties of NBTO thin films. Oxygen pressure exerts a substantial influence on the structural and electrical characteristics of thin films. Therefore, oxygen vacancies may occur because of oxygen fluctuation during deposition, which may lead to the appearance of secondary phases. The laser fluence has a considerable influence on the particle size and density of thin films, whilst the deposition rate helps to maintain the target stoichiometry and minimize volatile material deficiencies such as Na and Bi. Thus, for electrocaloric studies of NBTO-based thin films, the choice of a more suitable substrate, with an ideal combination of substrate temperature, oxygen background pressure, laser fluence, and deposition rate is essential. Moreover, additional doping materials or stoichiometric changes may be desirable.

Sr-doped $BaTiO_3$ was chosen as the second material system for study in this work. By pulsed laser deposition, $Ba_{1-x}Sr_xTiO_3$ layers with compositions ranging from $x = 0$ to $x = 0.3$ were deposited on SRO-buffered (001) oriented STO single crystals. XRD scans of all samples exhibit narrow (00ℓ) peaks and an increase of the 2θ angle with increasing Sr content, indicating a decrease of the out-of-plane lattice parameter, as expected [175]. Pole figure measurements showed a single epitaxial texture component for all samples. The SRO buffer transmits the orientation of the STO single crystal substrate to the ferroelectric layer, resulting in a cube-on-cube epitaxial relationship. RSM measurements revealed a comparable Q_x value for the SRO peak as for the STO substrate peak indicating coherent growth, which is typical of SRO due to a step-flow growth [192, 221, 222]. In comparison, the Q_x and Q_z values of the BSTO layer differ, pointing to a relaxed growth state induced by a significant lattice misfit that diminishes with increasing Sr concentration. The BSTO (103) peaks are significantly widened in reciprocal space, which may be related to the fine grain structure, strain, and mosaicity of the layer. With increasing Sr concentration, the in-plane and out-of-plane lattice parameters decrease. Nonetheless, a tetragonal

distortion was found for all samples even for a composition of x = 0.3, where a cubic structure is observed in bulk [175].

The influence of layer thickness on the structural properties of BSTO was studied by using a composition of x = 0.3. In contrast to NBTO films, a linear dependence was found between thickness and number of pulses up to a thickness of 700 nm. Standard XRD revealed distinct (00ℓ) peaks with a minor 2θ angle shift to higher values, implying that the out-of-plane lattice parameter decreases with increasing thickness. Pole figure analysis revealed no additional texture component apart from the epitaxial one. While the in-plane lattice parameter does not show significant variation with sample thickness, the out-of-plane lattice parameter gets smaller resulting in a decreased tetragonal distortion for larger thicknesses. In general, this change in lattice parameters may be due to the clamping to the substrate, which is reduced with a larger thickness. Again, there was no evidence of twinning even in the thickest layer, showing that the oxygen background pressure used is appropriate for the epitaxial growth of BSTO thin films.

AFM scans revealed a low surface roughness for all films, where the pure BTO sample showed a higher roughness compared to those with Sr doping. Smooth films, with a terrace-like structure, were found for a concentration of x = 0.3, which might be the result of a layer-by-layer or step-flow growth. The rms value increases only slightly with sample thickness up to a rms value of 0.23 nm for the 680 thick films. These values are significantly lower than those found in the literature [225]. Contrary to the NBTO films, no visible columnar structures and a clean interface between all layers was observed in SEM cross-sections.

Permittivity measurements revealed diffuse phase transitions for all Sr concentrations, which might originate from the substrate clamping. The temperature of maximum permittivity decreases with increasing Sr content reaching negative values for x = 0.3. Studies on thicker layers with x = 0.3 revealed the same broad permittivity peaks indicating a diffuse phase transition and a linear relationship between thickness and maximum permittivity. Furthermore, the frequency dependence of the temperature of maximum permittivity is a sign of a relaxor ferroelectric behavior.

Polarization measurements showed symmetric hysteresis loops with a narrow s-shaped structure typical for a thin ferroelectric relaxor film. The

maximum polarization decreases with increasing Sr content, which might be explained by the fact that Sr-containing ceramics undergo changes in grain size, density, and morphology. The maximum polarization increases with increasing thickness due to the relaxation of compressive stresses induced by misfit dislocations. As the temperature decreases, the polarization increases and the hysteresis loops get narrower, indicating that the films are progressively transitioning from the paraelectric to the ferroelectric phase.

The indirect method is based on a thermodynamic analysis of field and temperature-dependent polarization measurements. Pure BTO revealed a slightly higher adiabatic temperature change (0.8 K) than Sr-containing samples, of which $x = 0.3$ showed the highest $|\Delta T|$ at 0.76 K under an electric field of 350 kV cm^{-1}. The influence of film thickness on the ECE might be due to the clamping effect, which has a smaller impact as the thickness increases. This is corroborated by the results, where $|\Delta T|$ increased with increasing film thickness. By applying higher electric fields, the obtained $|\Delta T|$ increased in a linear relation with the electric field. At 750 kV cm^{-1}, a $|\Delta T|$ of 2.9 K was reached, for the 680 nm sample. This corresponds to an ECE strength of 0.04×10^{-6} K m V^{-1}. The determined electrocaloric properties are comparable to those of other BSTO thin films and higher than those of bulk BSTO [27, 52, 179, 183].

This dissertation makes the following contributions to the fields of solid-state cooling and electrocaloric effect research:

- Valuable information concerning the growth of NBTO and BSTO thin films is provided. In-depth structural analyses have been critical in clarifying the growth mechanisms that occurred during the fabrication of these films.

- The substrate selection, in conjunction with optimum deposition conditions, was found crucial for investigating the relationship between the microstructure of studied epitaxial thin films and the electrocaloric effect.

- Polarization measurements demonstrated that external factors such as leakage currents might cause deformations of the hysteresis loops, resulting in an inaccurate calculation of the ECE. Furthermore, the $P(E)$ loops utilized for assessment should be symmetrical to the coordinate origin which is not the case for NBTO-based samples. As a result, the

samples should have the lowest possible residual conductivity over the full temperature range examined.

- It was also shown that the deposition conditions for the BSTO samples are optimized, resulting in epitaxial growth for all Sr concentrations with a low defect density and smooth surfaces. Moreover, it was demonstrated that epitaxial growth is achievable for samples measuring up to 700 nm.

- Furthermore, it was revealed that the samples can withstand a magnitude of the applied electric field up to 750 kV cm^{-1}, resulting in a larger $|\Delta T|$ that can also increase with increasing sample thickness.

Sequential deposition of all layers and subsequent microstructure may lead to an enhanced interface between layers and a lesser number of defects, as well as a decrease in the influence of the "dead" layer, resulting in a larger magnitude of the electrocaloric effect. To avoid the disadvantages of the indirect method, the direct measurement of $|\Delta T|$ is the next milestone for ECE in thin films. The fast dissipation of heat caused by the ECE in the film into the substrate is one of the major hurdles to the direct characterization of thin films. This obstacle can be addressed if devices with high sensitivity and time resolution are developed.

Bibliography

1.   Information NCfE. State of the Climate: Global Climate Report for Annual 2020 National Centers for Environmental Information [Available from: https://www.ncdc.noaa.gov/sotc/global/202013.

2.   Allen MR, Dube OP, Solecki W, Aragón-Durand F, Cramer W, Humphreys S, et al. Framing and context. Global warming of. 2018;1(5).

3.   Edenhofer O. Climate change 2014: mitigation of climate change: Cambridge University Press; 2015. 110705821X

4.   Rogelj J, Shindell D, Jiang K, Fifita S, Forster P, Ginzburg V, et al. Mitigation pathways compatible with 1.5 °C in the context of sustainable development. Global warming of 15° C: Intergovernmental Panel on Climate Change (IPCC); 2018. p. 93-174.

5.   Solomon S, Manning M, Marquis M, Qin D. Climate change 2007-the physical science basis: Working group I contribution to the fourth assessment report of the IPCC: Cambridge university press; 2007. 0521705967

6.   Dupont J-L, Domanski P, Lebrun P, Ziegler F. The role of refrigeration in the global economy. Informatory Note on Refrigeration Technologies. 2019.

7.   Mota-Babiloni A, Barbosa JR, Makhnatch P, Lozano JA. Assessment of the utilization of equivalent warming impact metrics in refrigeration, air conditioning and heat pump systems. Renewable and Sustainable Energy Reviews. 2020;129:109929.

8.   Coulomb D, Dupont J-L, Morlet V. The impact of the refrigeration sector on climate change. Informatory Note on Refrigeration Technologies. 2017.

9.   Correia T, Zhang Q. Electrocaloric Effect: An Introduction. Correia T, Zhang Q, editors. Berlin, Heidelberg: Springer Berlin Heidelberg; 2014. 1-15 p. 978-3-642-40264-7

10.   Liu Y, Scott JF, Dkhil B. Some strategies for improving caloric responses with ferroelectrics. APL Materials. 2016;4(6):064109.

11.   Liu Y, Scott JF, Dkhil B. Direct and indirect measurements on electrocaloric effect: Recent developments and perspectives. Applied Physics Reviews. 2016;3(3):031102.

12.   Scott JF. Electrocaloric Materials. Annual Review of Materials Research. 2011;41(1):229-40.

13.   Greco A, Masselli C. Electrocaloric Cooling: A Review of the Thermodynamic Cycles, Materials, Models, and Devices. Magnetochemistry. 2020;6(4):67.

14.   Moya X, Kar-Narayan S, Mathur ND. Caloric materials near ferroic phase transitions. Nature Materials. 2014;13:439.

15.   Ožbolt M, Kitanovski A, Tušek J, Poredoš A. Electrocaloric refrigeration: Thermodynamics, state of the art and future perspectives. International Journal of Refrigeration. 2014;40:174-88.

16.   Kobeko   P,   Kurtschatov   J.   Dielektrische   eigenschaften   der seignettesalzkristalle.   Zeitschrift   für   Physik   A   Hadrons   and   Nuclei. 1930;66(3):192-205.

17.   Aprea C, Greco A, Maiorino A, Masselli C, editors. Electrocaloric refrigeration: an innovative, emerging, eco-friendly refrigeration technique. Journal of Physics: Conference Series; 2017: IOP Publishing.

18.   Mischenko A, Zhang Q, Scott J, Whatmore R, Mathur N. Giant electrocaloric effect in thin-film $PbZr_{0.95}Ti_{0.05}O_3$. Science. 2006;311(5765):1270-1.

19.   Panda PK. Review: environmental friendly lead-free piezoelectric materials. Journal of Materials Science. 2009;44(19):5049-62.

20.   Bai Y, Zheng G-P, Ding K, Qiao L, Shi S-Q, Guo D. The giant electrocaloric effect and high effective cooling power near room-temperature for $BaTiO_3$ thick film. Journal of Applied Physics. 2011;110(9):094103.

21.   Moya X, Stern-Taulats E, Crossley S, González-Alonso D, Kar-Narayan S, Planes A, et al. Giant Electrocaloric Strength in Single crystal $BaTiO_3$. Advanced Materials. 2013;25(9):1360-5.

22.   Zhang L, Zhao C, Zheng T, Wu J. Large electrocaloric effect in $(Bi_{0.5}Na_{0.5})TiO_3$-based relaxor ferroelectrics. ACS Applied Materials & Interfaces. 2020;12(30):33934-40.

23.   Magalhaes B, Engelhardt S, Molin C, Gebhardt SE, Nielsch K, Hühne R. Electrocaloric temperature changes in epitaxial $Ba_{1-x}Sr_xTiO_3$ films. Journal of Alloys and Compounds. 2022;891:162041.

24.   Chen H, Ren T-L, Wu X-M, Yang Y, Liu L-T. Giant electrocaloric effect in lead-free thin film of strontium bismuth tantalite. Applied Physics Letters. 2009;94(18):182902.

25.   Lu S-G, Rožič B, Zhang Q, Kutnjak Z, Neese B. Enhanced electrocaloric effect in ferroelectric poly (vinylidene-fluoride/trifluoroethylene) 55/45 mol% copolymer at ferroelectric-paraelectric transition. Applied Physics Letters. 2011;98(12):122906.

26.   Liu P, Wang J, Meng X, Yang J, Dkhil B, Chu J. Huge electrocaloric effect in Langmuir–Blodgett ferroelectric polymer thin films. New Journal of Physics. 2010;12(2):023035.

27.   Dai G, Wang S, Huang G, Chen G, Lu B, Li D, et al. Direct and indirect measurement of large electrocaloric effect in barium strontium titanate ceramics. International Journal of Applied Ceramic Technology. 2020;17(3):1354-61.

28.   Kar-Narayan S, Crossley S, Moya X, Kovacova V, Abergel J, Bontempi A, et al. Direct electrocaloric measurements of a multilayer capacitor using scanning thermal microscopy and infra-red imaging. Applied Physics Letters. 2013;102(3):032903.

29.   Hautzenlaub JF. Electric and dielectric behaviour of potassium dihydrogen phosphate. Massachusetts Institute of Technology; 1943.

30.   Karchevskii AI. Electrocaloric effect in polycrystalline $BaTiO_3$. Sov Phys-Solid State. 1962;3(2249).

31.   Radebaugh R, Lawless WN, Siegwarth JD, Morrow AJ. Feasibility of electrocaloric refrigeration for the 4–15 K temperature range. Cryogenics. 1979;19(4):187-208.

32.   Thacher PD. Electrocaloric Effects in Some Ferroelectric and Antiferroelectric $Pb(Zr,Ti)O_3$ Compounds. Journal of Applied Physics. 1968;39(4):1996-2002.

33.   Shebanovs L, Borman K, Lawless WN, Kalvane A. Electrocaloric Effect in Some Perovskite Ferroelectric Ceramics and Multilayer Capacitors. Ferroelectrics. 2002;273(1):137-42.

34.   Neese B, Chu B, Lu S-G, Wang Y, Furman E, Zhang QM. Large Electrocaloric Effect in Ferroelectric Polymers Near Room-temperature. Science. 2008;321(5890):821.

35.   Digital Science. (2018 -) Dimensions [Software] Available from: https://app.dimensions.ai/. [Accessed January 2022], under licence agreement.

36.   Bai Y, Zheng G-P, Shi S-Q. Abnormal electrocaloric effect of $Na_{0.5}Bi_{0.5}TiO_3$–$BaTiO_3$ lead-free ferroelectric ceramics above room-temperature. Materials Research Bulletin. 2011;46(11):1866-9.

37.   Axelsson A-K, Le Goupil F, Dunne L, Manos G, Valant M, Alford NM. Microscopic interpretation of sign reversal in the electrocaloric effect in a ferroelectric $PbMg_{1/3}Nb_{2/3}O_3$-30$PbTiO_3$ single crystal. Applied Physics Letters. 2013;102(10):102902.

38.   Li B, Wang J, Zhong X, Wang F, Zeng Y, Zhou Y. The coexistence of the negative and positive electrocaloric effect in ferroelectric thin films for solid-state refrigeration. EPL (Europhysics Letters). 2013;102(4):47004.

39.   Goupil FL, Berenov A, Axelsson A-K, Valant M, Alford NM. Direct and indirect electrocaloric measurements on ⟨001⟩ -$PbMg_{1/3}Nb_{2/3}O_3$-30$PbTiO_3$ single crystals. Journal of Applied Physics. 2012;111(12):124109.

40.   Lu S-G, Zhang Q, Kutnjak Z. The electrocaloric effect (ECE) in ferroelectric polymer films. Thin Film Growth: Elsevier; 2011. p. 364-83.

41.   Lang SB. Cryogenic refrigeration utilizing the electrocaloric effect in pyroelectric lithium sulfate monohydrate. Ferroelectrics. 1976;11(1):519-23.

42.   Rožič B, Kosec M, Uršič H, Holc J, Malič B, Zhang Q, et al. Influence of the critical point on the electrocaloric response of relaxor ferroelectrics. Journal of Applied Physics. 2011;110(6):064118.

43.   Kutnjak Z, Rožič B, Pirc R. Electrocaloric effect: theory, measurements, and applications. Wiley encyclopedia of electrical and electronics engineering. 2015.

44.   He J, Chen J, Wang JT, Hua B. Inherent regenerative losses of a ferroelectric Ericsson refrigeration cycle. International Journal of Thermal Sciences. 2003;42(2):169-75.

45.   He J, Chen J, Zhou Y, Wang JT. Regenerative characteristics of electrocaloric Stirling or Ericsson refrigeration cycles. Energy conversion and management. 2002;43(17):2319-27.

46.   Moya X, Mathur N. Caloric materials for cooling and heating. Science. 2020;370(6518):797-803.

47.   Dan'Kov SY, Tishin A, Pecharsky V, Gschneidner K. Magnetic phase transitions and the magnetothermal properties of gadolinium. Physical Review B. 1998;57(6):3478.

48.   Wada H, Tanabe Y. Giant magnetocaloric effect of $MnAs_{1-x}Sb_x$. Applied physics letters. 2001;79(20):3302-4.

49.   Tegus O, Brück E, Buschow K, De Boer F. Transition-metal-based magnetic refrigerants for room-temperature applications. Nature. 2002;415(6868):150-2.

50.   Dung NH, Ou ZQ, Caron L, Zhang L, Thanh DTC, De Wijs GA, et al. Mixed magnetism for refrigeration and energy conversion. Advanced Energy Materials. 2011;1(6):1215-9.

51.   Hu F-x, Shen B-g, Sun J-r, Wu G-h. Large magnetic entropy change in a Heusler alloy $Ni_{52.6}Mn_{23.1}Ga_{24.3}$ single crystal. Physical Review B. 2001;64(13):132412.

52.   Liu XQ, Chen TT, Wu YJ, Chen XM. Enhanced Electrocaloric Effects in Spark Plasma- Sintered $Ba_{0.65}Sr_{0.35}TiO_3$- Based Ceramics at Room-temperature. Journal of the American Ceramic Society. 2013;96(4):1021-3.

53.   Correia TM, Young JS, Whatmore RW, Scott JF, Mathur ND, Zhang Q. Investigation of the electrocaloric effect in a $PbMg_{2/3}Nb_{1/3}O_3$-$PbTiO_3$ relaxor thin film. Applied Physics Letters. 2009;95(18):182904.

100

54.   Li X, Qian X-S, Gu H, Chen X, Lu S, Lin M, et al. Giant electrocaloric effect in ferroelectric poly (vinylidenefluoride-trifluoroethylene) copolymers near a first-order ferroelectric transition. Applied Physics Letters. 2012;101(13):132903.

55.   Xiao F, Fukuda T, Kakeshita T. Significant elastocaloric effect in a Fe-31.2 Pd (at.%) single crystal. Applied Physics Letters. 2013;102(16):161914.

56.   Quarini J, Prince A. Solid state refrigeration: Cooling and refrigeration using crystalline phase changes in metal alloys. Proceedings of the Institution of Mechanical Engineers, Part C: Journal of Mechanical Engineering Science. 2004;218(10):1175-9.

57.   Brown L. The thermal effect in pseudoelastic single crystals of β-CuZnSn. Metallurgical and Materials Transactions A. 1981;12(8):1491-4.

58.   Rodriguez C, Brown L. The thermal effect due to stress-induced martensite formation in β-CuAlNi single crystals. Metallurgical and Materials Transactions A. 1980;11(1):147-50.

59.   Cui J, Wu Y, Muehlbauer J, Hwang Y, Radermacher R, Fackler S, et al. Demonstration of high efficiency elastocaloric cooling with large ΔT using NiTi wires. Applied Physics Letters. 2012;101(7):073904.

60.   Mañosa L, González-Alonso D, Planes A, Bonnot E, Barrio M, Tamarit J-L, et al. Giant solid-state barocaloric effect in the Ni–Mn–In magnetic shape-memory alloy. Nature materials. 2010;9(6):478-81.

61.   Yuce S, Barrio M, Emre B, Stern-Taulats E, Planes A, Tamarit J-L, et al. Barocaloric effect in the magnetocaloric prototype Gd5Si2Ge2. Applied Physics Letters. 2012;101(7):071906.

62.   Mañosa L, Gonzalez-Alonso D, Planes A, Barrio M, Tamarit J-L, Titov IS, et al. Inverse barocaloric effect in the giant magnetocaloric La–Fe–Si–Co compound. Nature communications. 2011;2(1):1-5.

63.   Aprea C, Greco A, Maiorino A, Masselli C. A comparison between different materials in an active electrocaloric regenerative cycle with a 2D numerical model. International Journal of Refrigeration. 2016;69:369-82.

64.   Liu ZK, Li X, Zhang QM. Maximizing the number of coexisting phases near invariant critical points for giant electrocaloric and electromechanical responses in ferroelectrics. Applied Physics Letters. 2012;101(8):082904.

65.   Qian X-S, Ye H-J, Zhang Y-T, Gu H, Li X, Randall CA, et al. Giant Electrocaloric Response Over A Broad Temperature Range in Modified $BaTiO_3$ Ceramics. Advanced Functional Materials. 2014;24(9):1300-5.

66.   Tang J, Wang F, Zhao X, Luo H, Luo L, Shi W. Influence of the composition-induced structure evolution on the electrocaloric effect in $Bi_{0.5}Na_{0.5}TiO_3$-based solid solution. Ceramics International. 2015;41(4):5888-93.

67.   Uddin S, Zheng G-P, Iqbal Y, Ubic R, Yang J. Unification of the negative electrocaloric effect in $Bi_{1/2}Na_{1/2}TiO_3$-$BaTiO_3$ solid solutions by $Ba_{1/2}Sr_{1/2}TiO_3$ doping. Journal of Applied Physics. 2013;114(21):213519.

68.   Hiruma Y, Nagata H, Takenaka T. Phase diagrams and electrical properties of $(Bi_{1/2}Na_{1/2})TiO_3$-based solid solutions. Journal of Applied Physics. 2008;104(12):124106.

69.   Zhang ST, Kounga AB, Jo W, Jamin C, Seifert K, Granzow T, et al. High-strain lead- free antiferroelectric electrostrictors. Advanced materials. 2009;21(46):4716-20.

70.   Cao W, Li W, Xu D, Hou Y, Wang W, Fei W. Enhanced electrocaloric effect in lead-free NBT-based ceramics. Ceramics International. 2014;40(7):9273-8.

71.   Valant M. Electrocaloric materials for future solid-state refrigeration technologies. Progress in Materials Science. 2012;57(6):980-1009.

72.   Agarwal V, Srivastava V. Thickness dependence of breakdown field in thin films. Thin solid films. 1971;8(5):377-81.

73.   Forlani F, Minnaja N. Thickness influence in breakdown phenomena of thin dielectric films. physica status solidi (b). 1964;4(2):311-24.

74.   Newnham RE. Properties of materials: anisotropy, symmetry, structure: Oxford University Press on Demand; 2005. 0198520751

75.   Sebald G, Seveyrat L, Guyomar D, Lebrun L, Guiffard B, Pruvost S. Electrocaloric and pyroelectric properties of $0.75Pb(Mg_{1/3}Nb_{2/3})O_3$–$0.25PbTiO_3$ single crystals. Journal of applied physics. 2006;100(12):124112.

76.   Marathe M, Renggli D, Sanlialp M, Karabasov MO, Shvartsman VV, Lupascu DC, et al. Electrocaloric effect in $BaTiO_3$ at all three ferroelectric transitions: Anisotropy and inverse caloric effects. Physical Review B. 2017;96(1):014102.

77.   Alpay SP, Mantese J, Trolier-McKinstry S, Zhang Q, Whatmore RW. Next-generation electrocaloric and pyroelectric materials for solid-state electrothermal energy interconversion. Mrs Bulletin. 2014;39(12):1099-111.

78.   Crossley S. Electrocaloric materials and devices. University of Cambridge; 2013.

79.   Lu SG, Zhang Q. Electrocaloric Materials for Solid- State Refrigeration. Advanced Materials. 2009;21(19):1983-7.

80.   Damjanovic D. Ferroelectric, dielectric and piezoelectric properties of ferroelectric thin films and ceramics. Reports on Progress in Physics. 1998;61(9):1267.

81.   Whatmore R. Ferroelectric Materials. Springer Handbook of Electronic and Photonic Materials: Springer; 2017. p. 1-.

102

82. Valasek J. Piezo-electric and allied phenomena in Rochelle salt. Physical review. 1921;17(4):475.

83. Kao KC. Ferroelectrics, piezoelectrics and pyroelectrics. Dielectric phenomena in solids. 2004;4:213-82.

84. Haertling GH. Ferroelectric ceramics: history and technology. Journal of the American Ceramic Society. 1999;82(4):797-818.

85. Buixaderas E, Kamba S, Petzelt J. Lattice dynamics and central-mode phenomena in the dielectric response of ferroelectrics and related materials. Ferroelectrics. 2004;308(1):131-92.

86. Dawber M, Rabe KM, Scott JF. Physics of thin-film ferroelectric oxides. Reviews of Modern Physics. 2005;77(4):1083-130.

87. Setter N, Damjanovic D, Eng L, Fox G, Gevorgian S, Hong S, et al. Ferroelectric thin films: Review of materials, properties, and applications. Journal of Applied Physics. 2006;100(5):051606.

88. Rabe KM, Dawber M, Lichtensteiger C, Ahn CH, Triscone J-M. Modern Physics of Ferroelectrics:Essential Background. Physics of Ferroelectrics: A Modern Perspective. Berlin, Heidelberg: Springer Berlin Heidelberg; 2007. p. 1-30. 978-3-540-34591-6

89. Tagantsev AK, Cross LE, Fousek J. Domains in ferroic crystals and thin films: Springer; 2010.

90. Lines ME, Glass AM. Principles and applications of ferroelectrics and related materials: Oxford university press; 2001. 019850778X

91. Arlt G. Twinning in ferroelectric and ferroelastic ceramics: stress relief. Journal of materials Science. 1990;25(6):2655-66.

92. Matthias B, Von Hippel A. Domain structure and dielectric response of barium titanate single crystals. Physical Review. 1948;73(11):1378.

93. Burfoot JC, Taylor GW. Polar dielectrics and their applications: Univ of California Press; 1979. 0520037499

94. Newnham RE. Structure-property relations: Springer Science & Business Media; 2012. 364250017X

95. Cao W. The strain limits on switching. Nature materials. 2005;4(10):727-8.

96. Xu Y. Ferroelectric materials and their applications: Elsevier; 2013. 1483290956

97. Strukov BA, Levanyuk AP. Ferroelectric phenomena in crystals: physical foundations: Springer Science & Business Media; 2012. 3642602932

98.   Huang S, Sun L, Feng C, Chen L. Relaxor behavior of layer structured $SrBi_{1.65}La_{0.35}Nb_2O_9$. American Institute of Physics; 2006.

99.   Craciun F. Strong variation of electrostrictive coupling near an intermediate temperature of relaxor ferroelectrics. Physical Review B. 2010;81(18):184111.

100.   Samara GA. The relaxational properties of compositionally disordered ABO_3 perovskites. Journal of Physics: Condensed Matter. 2003;15(9):R367.

101.   Shvartsman VV, Lupascu DC. Lead- free relaxor ferroelectrics. Journal of the American Ceramic Society. 2012;95(1):1-26.

102.   Dai X, Xu Z, Li J-F, Viehland D. Effects of lanthanum modification on rhombohedral $Pb(Zr_{1-x}Ti_x)O_3$ ceramics: Part I. Transformation from normal to relaxor ferroelectric behaviors. Journal of materials research. 1996;11(3):618-25.

103.   Dai X, Xu Z, Li J-F, Viehland D. Effects of lanthanum modification on rhombohedral $Pb(Zr_{1-x}Ti_x)O_3$ ceramics: Part II. Relaxor behavior versus enhanced antiferroelectric stability. Journal of materials research. 1996;11(3):626-38.

104.   Zhu W, Yan M. Effect of Mn-doping on the morphotropic phase boundary of PZN-BT-PT system. Journal of materials science letters. 2001;20(16):1527-9.

105.   González-Abreu Y, Peláiz-Barranco A, Araújo E, Júnior AF. Dielectric relaxation and relaxor behavior in bilayered perovskites. Applied Physics Letters. 2009;94(26):262903.

106.   Liu G, Zhang S, Jiang W, Cao W. Losses in ferroelectric materials. Materials Science and Engineering: R: Reports. 2015;89:1-48.

107.   Setter N, Cross L. The role of B- site cation disorder in diffuse phase transition behavior of perovskite ferroelectrics. Journal of Applied Physics. 1980;51(8):4356-60.

108.   Cross LE. Relaxor ferroelectrics. Ferroelectrics. 1987;76(1):241-67.

109.   Cross LE. Relaxorferroelectrics: an overview. Ferroelectrics. 1994;151(1):305-20.

110.   Bokov A, Ye Z-G. Recent progress in relaxor ferroelectrics with perovskite structure. Progress in Advanced Dielectrics. 2020:105-64.

111.   Cowley R, Gvasaliya S, Lushnikov S, Roessli B, Rotaru G. Relaxing with relaxors: a review of relaxor ferroelectrics. Advances in Physics. 2011;60(2):229-327.

112.   Kleemann W. Random fields in relaxor ferroelectrics—a jubilee review. Journal of Advanced Dielectrics. 2012;2(02):1241001.

113.   Ahn CW, Hong C-H, Choi B-Y, Kim H-P, Han H-S, Hwang Y, et al. A brief review on relaxor ferroelectrics and selected issues in lead-free relaxors. Journal of the Korean Physical Society. 2016;68(12):1481-94.

114.   Kleemann W, Dec J, Miga S. Superdipole glass ground state of relaxor ferroelectrics. Ferroelectrics. 2016;499(1):72-5.

115.   Burns G, Dacol F. Glassy polarization behavior in ferroelectric compounds Pb $(Mg_{1/3}Nb_{2/3})O_3$ and Pb $(Zn_{1/3}Nb_{2/3})O_3$. Solid state communications. 1983;48(10):853-6.

116.   Delgado M, Colla EV, Griffin P, Weissman MB, Viehland D. Field dependence of glassy freezing in a relaxor ferroelectric. Physical Review B. 2009;79(14):140102.

117.   Höchli U, Knorr K, Loidl A. Orientational glasses. Advances in Physics. 1990;39(5):405-615.

118.   Westphal V, Kleemann W, Glinchuk M. Diffuse phase transitions and random-field-induced domain states of the "relaxor"ferroelectric $PbMg_{1/3}Nb_{2/3}O_3$. Physical Review Letters. 1992;68(6):847.

119.   Kutnjak Z, Pirc R, Blinc R. Field-cooled static nonlinear response of relaxor ferroelectrics. Applied physics letters. 2002;80(17):3162-4.

120.   Pirc R, Blinc R, Kutnjak Z. Nonlinear dielectric response of relaxor ferroelectrics. Physical Review B. 2002;65(21):214101.

121.   Ma Y. Electrocaloric Effect of Ferroelectrics and Relaxors. Technische Universität Darmstadt; 2018.

122.   Bobnar V, Kutnjak Z, Pirc R, Levstik A. Electric-field–temperature phase diagram of the relaxor ferroelectric lanthanum-modified lead zirconate titanate. Physical Review B. 1999;60(9):6420.

123.   Kutnjak Z, Vodopivec B, Blinc R. Anisotropy of electric field freezing of the relaxor ferroelectric $Pb(Mg_{1/3}Nb_{2/3})O_3$. Physical Review B. 2008;77(5):054102.

124.   Lu S-G, Rožič B, Zhang Q, Kutnjak Z, Li X, Furman E, et al. Organic and inorganic relaxor ferroelectrics with giant electrocaloric effect. Applied Physics Letters. 2010;97:162904-.

125.   Tong T, Karthik J, Martin LW, Cahill DG. Secondary effects in wide frequency range measurements of the pyroelectric coefficient of $Ba_{0.6}Sr_{0.4}TiO_3$ and $PbZr_{0.2}Ti_{0.8}O_3$ epitaxial layers. Physical Review B. 2014;90(15):155423.

126.   Yao H, Ema K, Garland CW. Nonadiabatic scanning calorimeter. Review of scientific instruments. 1998;69(1):172-8.

127.   Rožič B, Malič B, Uršič H, Holc J, Kosec M, Neese B, et al. Direct measurements of the giant electrocaloric effect in soft and solid ferroelectric materials. Ferroelectrics. 2010;405(1):26-31.

128.   Lu S, Rožič B, Zhang Q, Kutnjak Z, Pirc R, Lin M, et al. Comparison of directly and indirectly measured electrocaloric effect in relaxor ferroelectric polymers. Applied Physics Letters. 2010;97(20):202901.

129.   Sanlialp M, Shvartsman VV, Faye R, Karabasov MO, Molin C, Gebhardt S, et al. Quasi-adiabatic calorimeter for direct electrocaloric measurements. Review of Scientific Instruments. 2018;89(3):034903.

130.   Wiseman GG. Electrocaloric effect in potassium dihydrogen phosphate. IEEE Transactions on Electron Devices. 1969;16(6):588-93.

131.   Sebald G, Seveyrat L, Capsal J-F, Cottinet P-J, Guyomar D. Differential scanning calorimeter and infrared imaging for electrocaloric characterization of poly (vinylidene fluoride-trifluoroethylene-chlorofluoroethylene) terpolymer. Applied Physics Letters. 2012;101(2):022907.

132.   Kutnjak Z, Rožič B. Indirect and Direct Measurements of the Electrocaloric Effect. In: Correia T, Zhang Q, editors. Electrocaloric Materials: New Generation of Coolers. Berlin, Heidelberg: Springer Berlin Heidelberg; 2014. p. 147-82. 978-3-642-40264-7

133.   Sanlialp M, Molin C, Shvartsman VV, Gebhardt S, Lupascu DC. Modified differential scanning calorimeter for direct electrocaloric measurements. IEEE transactions on ultrasonics, ferroelectrics, and frequency control. 2016;63(10):1690-6.

134.   Guyomar D, Sebald G, Guiffard B, Seveyrat L. Ferroelectric electrocaloric conversion in 0.75(PbMg$_{1/3}$Nb$_{2/3}$O$_3$)–0.25 (PbTiO$_3$) ceramics. Journal of Physics D: Applied Physics. 2006;39(20):4491.

135.   Bai Y, Zheng G, Shi S. Direct measurement of giant electrocaloric effect in BaTiO$_3$ multilayer thick film structure beyond theoretical prediction. Applied Physics Letters. 2010;96(19):192902.

136.   Jia Y, Sungtaek Ju Y. Direct characterization of the electrocaloric effects in thin films supported on substrates. Applied Physics Letters. 2013;103(4):042903.

137.   Matsushita Y, Nochida A, Yoshimura T, Fujimura N. Direct measurements of electrocaloric effect in ferroelectrics using thin-film thermocouples. Japanese Journal of Applied Physics. 2016;55(10S):10TB04.

138.   Kar-Narayan S, Mathur N. Direct and indirect electrocaloric measurements using multilayer capacitors. Journal of Physics D: Applied Physics. 2010;43(3):032002.

139.   Kar-Narayan S, Crossley S, Mathur ND. Electrocaloric Multilayer Capacitors. In: Correia T, Zhang Q, editors. Electrocaloric Materials: New Generation of Coolers. Berlin, Heidelberg: Springer Berlin Heidelberg; 2014. p. 91-105. 978-3-642-40264-7

140.	Qiu JH, Jiang Q. Effect of misfit strain on the electrocaloric effect in epitaxial SrTiO$_3$ thin films. The European Physical Journal B. 2009;71(1):15.

141.	Qiu J, Jiang Q. Misfit strain dependence of electrocaloric effect in epitaxial Pb(Zr$_{1-x}$Ti$_x$)O$_3$ thin films. Journal of Applied Physics. 2008;103(8):084105.

142.	Zhang X, Wang JB, Li B, Zhong XL, Lou XJ, Zhou YC. Sizable electrocaloric effect in a wide temperature range tuned by tensile misfit strain in BaTiO$_3$ thin films. Journal of Applied Physics. 2011;109(12):126102.

143.	Marathe M, Ederer C. Electrocaloric effect in BaTiO$_3$: a first-principles-based study on the effect of misfit strain. Applied Physics Letters. 2014;104(21):212902.

144.	Sanlialp M, Shvartsman VV, Acosta M, Dkhil B, Lupascu DC. Strong electrocaloric effect in lead-free 0.65Ba(Zr$_{0.2}$Ti$_{0.8}$)O$_3$-0.35(Ba$_{0.7}$Ca$_{0.3}$)TiO$_3$ ceramics obtained by direct measurements. Applied Physics Letters. 2015;106(6):062901.

145.	Correia TM, Kar-Narayan S, Young JS, Scott JF, Mathur ND, Whatmore RW, et al. PST thin films for electrocaloric coolers. Journal of Physics D: Applied Physics. 2011;44(16):165407.

146.	Novak N, Kutnjak Z, Pirc R. High-resolution electrocaloric and heat capacity measurements in barium titanate. EPL (Europhysics Letters). 2013;103(4):47001.

147.	Marathe M, Grünebohm A, Nishimatsu T, Entel P, Ederer C. First-principles-based calculation of the electrocaloric effect in BaTiO$_3$: A comparison of direct and indirect methods. Physical Review B. 2016;93(5):054110.

148.	Smolensky G. New ferroelectrics of complex composition. IV. Sov Phys-Solid State. 1961;2:2651-4.

149.	Fähler S, Rößler UK, Kastner O, Eckert J, Eggeler G, Emmerich H, et al. Caloric Effects in Ferroic Materials: New Concepts for Cooling. Advanced Engineering Materials. 2012;14(1- 2):10-9.

150.	Daryapurkar A, Kolte J, Apte P, Gopalan P. Structural and electrical properties of sodium bismuth titanate (Na$_{0.5}$Bi$_{0.5}$TiO$_3$) thin films optimized using the Taguchi approach. Ceramics International. 2014;40(1):2441-50.

151.	Daryapurkar AS, Kolte J, Gopalan P. Influence of oxygen gas pressure on phase, microstructure and electrical properties of sodium bismuth titanate thin films grown using pulsed laser deposition. Thin Solid Films. 2015;579:44-9.

152.	Kutnjak Z, Petzelt J, Blinc R. The giant electromechanical response in ferroelectric relaxors as a critical phenomenon. Nature. 2006;441:956.

153.	Xiaoming L, Xiaoli T. Giant Strains in Non-Textured (Bi$_{1/2}$Na$_{1/2}$)TiO$_3$-Based Lead-Free Ceramics. Advanced Materials. 2016;28(3):574-8.

154. Isupov VA. Ferroelectric $Na_{0.5}Bi_{0.5}TiO_3$ and $K_{0.5}Bi_{0.5}TiO_3$ Perovskites and Their Solid Solutions. Ferroelectrics. 2005;315(1):123-47.

155. Priya S, Nahm S. Lead-free piezoelectrics: Springer Science & Business Media; 2011. 1441995986

156. Lu S-G, Zhang Q. Large electrocaloric effect in relaxor ferroelectrics. Journal of Advanced Dielectrics. 2012;2(03):1230011.

157. Cao WP, Li WL, Dai XF, Zhang TD, Sheng J, Hou YF, et al. Large electrocaloric response and high energy-storage properties over a broad temperature range in lead-free NBT-ST ceramics. Journal of the European Ceramic Society. 2016;36(3):593-600.

158. Hiruma Y, Imai Y, Watanabe Y, Nagata H, Takenaka T. Large electrostrain near the phase transition temperature of $(Bi_{0.5}Na_{0.5})TiO_3$–$SrTiO_3$ ferroelectric ceramics. Applied Physics Letters. 2008;92(26):262904.

159. Xiao DQ, Lin DM, Zhu JG, Yu P. Studies on new systems of BNT-based lead-free piezoelectric ceramics. Journal of Electroceramics. 2008;21(1):34-8.

160. Takenaka T, Maruyama K-iMK-i, Sakata KSK. (Bi1/2Na1/2) TiO3-BaTiO3 system for lead-free piezoelectric ceramics. Japanese journal of applied physics. 1991;30(9S):2236.

161. Le Goupil F, Bennett J, Axelsson A-K, Valant M, Berenov A, Bell AJ, et al. Electrocaloric enhancement near the morphotropic phase boundary in lead-free NBT-KBT ceramics. Applied Physics Letters. 2015;107(17):172903.

162. Le Goupil F, McKinnon R, Koval V, Viola G, Dunn S, Berenov A, et al. Tuning the electrocaloric enhancement near the morphotropic phase boundary in lead-free ceramics. Scientific Reports. 2016;6:28251.

163. Birks E, Dunce M, Peräntie J, Hagberg J, Sternberg A. Direct and indirect determination of electrocaloric effect in $Na_{0.5}Bi_{0.5}TiO_3$. Journal of Applied Physics. 2017;121(22):224102.

164. Jiang X, Luo L, Wang B, Li W, Chen H. Electrocaloric effect based on the depolarization transition in $(1−x)Bi_{0.5}Na_{0.5}TiO_3$–$xKNbO_3$ lead-free ceramics. Ceramics international. 2014;40(2):2627-34.

165. Le Goupil F, Alford NM. Upper limit of the electrocaloric peak in lead-free ferroelectric relaxor ceramics. APL Materials. 2016;4(6):064104.

166. Li F, Chen G, Liu X, Zhai J, Shen B, Zeng H, et al. Phase–composition and temperature dependence of electrocaloric effect in lead–free $Bi_{0.5}Na_{0.5}TiO_3$–$BaTiO_3$–$(Sr_{0.7}Bi_{0.2}\square_{0.1})TiO_3$ ceramics. Journal of the European Ceramic Society. 2017;37(15):4732-40.

167. Kumar A, Kumar R, Singh K, Singh S. Enhanced Electrocaloric Effect and Energy Storage Density in Lead- Free $0.8Na_{0.5}Bi_{0.5}TiO_3$- $0.2SrTiO_3$ Ceramics. physica status solidi (a). 2019;216(4):1800786.

168.   Kandula KR, Patri T, Asthana S. Nd^{3+} and Nb^{5+} co- substitution inducing a large electrocaloric response in $Na_{0.5}Bi_{0.5}TiO_3$ lead- free ceramics. physica status solidi (b). 2019;256(8):1900001.

169.   Li G, Li J, Li F, Li Y, Liu X, Jiang T, et al. Electrocaloric effect in BNT-based lead-free ceramics by local-structure and phase-boundary evolution. Journal of Alloys and Compounds. 2020;817:152794.

170.   Zhou X. Dielectric properties of barium strontium titanate (BST) thin films and phase shifters based on BST thin films. Hong Kong Polytechnic University; 2008.

171.   Kingon AI, Maria J-P, Streiffer S. Alternative dielectrics to silicon dioxide for memory and logic devices. Nature. 2000;406(6799):1032-8.

172.   Whatmore RW, Landi S, Shaw CP, Kirby PB. Pyroelectric arrays using ceramics and thin films integrated radiation collectors: Design fabrication and testing. Ferroelectrics. 2005;318(1):11-22.

173.   Zhong S, Alpay S, Ban Z-G, Mantese J. Effective pyroelectric response of compositionally graded ferroelectric materials. Applied Physics Letters. 2005;86(9):092903.

174.   Pithan C, Hennings D, Waser R. Progress in the synthesis of nanocrystalline $BaTiO_3$ powders for MLCC. International Journal of Applied Ceramic Technology. 2005;2(1):1-14.

175.   Adachi M, Akishige Y, Asahi T, Deguchi K, Gesi K, Hasebe K, et al. $SrTiO_3$-$BaTiO_3$, 1C-a28: Datasheet from Landolt-Börnstein - Group III Condensed Matter · Volume 36A1: "Oxides" in SpringerMaterials (https://doi.org/10.1007/10426842_134). In: Shiozaki Y, Nakamura E, Mitsui T, editors.: Springer-Verlag Berlin Heidelberg.

176.   Zhang G, Zhang X, Huang H, Wang J, Li Q, Chen LQ, et al. Toward wearable cooling devices: highly flexible electrocaloric $Ba_{0.67}Sr_{0.33}TiO_3$ nanowire arrays. Advanced Materials. 2016;28(24):4811-6.

177.   Ding K, Zheng G-P. Scaling for the refrigeration effects in lead-free barium titanate based ferroelectric ceramics. Journal of Electroceramics. 2014;32(2):169-74.

178.   Liu BL, Wang JB, Zhong XL, Huang K, Li B, Wang F, et al. Enhanced electrocaloric effect in a $Ba_{(1-x)}Sr_xTiO3$ compositionally graded film. RSC Advances. 2014;4(47):24533-7.

179.   Bai Y, Han X, Ding K, Qiao L-J. Combined effects of diffuse phase transition and microstructure on the electrocaloric effect in $Ba_{1-x}Sr_xTiO_3$ ceramics. Applied Physics Letters. 2013;103(16):162902.

180.   Srikanth KS, Patel S, Vaish R. Electrocaloric behavior and temperature dependent scaling of dynamic hysteresis of $Ba_xSr_{1-x}TiO_3$ (x = 0.7, 0.8 and 0.9) bulk ceramics. Journal of the Australian Ceramic Society. 2018;54(3):439-50.

181.   Bai Y, Han F, Xie S, Li J, Qin S, Li J, et al. Thickness dependence of electrocaloric effect in high-temperature sintered $Ba_{0.8}Sr_{0.2}TiO_3$ ceramics. Journal of Alloys and Compounds. 2018;736:57-61.

182.   Lisenkov S, Ponomareva I. Intrinsic electrocaloric effect in ferroelectric alloys from atomistic simulations. Physical Review B. 2009;80(14):140102.

183.   Yamada T, Matsuo S, Kamo T, Funakubo H, Yoshino M, Nagasaki T. Experimental study of effect of strain on electrocaloric effect in (001)-epitaxial $(Ba,Sr)TiO_3$ thin films. Japanese Journal of Applied Physics. 2017;56(10S):10PF5.

184.   Schneider CW, Lippert T. Laser ablation and thin film deposition. Laser processing of materials: Springer; 2010. p. 89-112.

185.   Ma C, Chen C. Pulsed Laser Deposition for Complex Oxide Thin Film and Nanostructure. Advanced Nano Deposition Methods. 2016:19.

186.   Willmott PR, Huber JR. Pulsed laser vaporization and deposition. Reviews of Modern Physics. 2000;72(1):315-28.

187.   Strikovski M, Kim J, Kolagani SH. Plasma energetics in pulsed laser and pulsed electron deposition. Springer Handbook of Crystal Growth. 2010:1193-211.

188.   Miriyala K, Ramadurai R. Microstructural influence on ferroelectric domain pattern and piezoelectric properties of $Na_{0.5}Bi_{0.5}TiO_3$ thin films. Ceramics International. 2018;44(12):14556-62.

189.   Ma C, Chen C. Pulsed laser deposition for complex oxide thin film and nanostructure. Advanced Nano Deposition Methods. 2016:1-31.

190.   Engelhardt S, Mietschke M, Molin C, Gebhardt S, Fähler S, Nielsch K, et al. Structural and ferroelectric properties of epitaxial $BaZr_xTi_{1-x}O_3$ thin films. Journal of Physics D: Applied Physics. 2016;49(49):495303.

191.   Jones C, Battle P, Lightfoot P, Harrison W. The structure of $SrRuO_3$ by time-of-flight neutron powder diffraction. Acta Crystallographica Section C: Crystal Structure Communications. 1989;45(3):365-7.

192.   Engelhardt S. Epitaktische $BaTiO_3$-basierte Schichten für elektrakalorische Untersuchungen. Technische Universität Dresden; 2019.

193.   Klein A. Interface Properties of Dielectric Oxides. Journal of the American Ceramic Society. 2016;99(2):369-87.

194.   Streiffer SK, Basceri C, Parker CB, Lash SE, Kingon AI. Ferroelectricity in thin films: The dielectric response of fiber-textured $(Ba_xSr_{1-x})Ti_{1+y}O_{3+z}$ thin films grown by chemical vapor deposition. Journal of Applied Physics. 1999;86(8):4565-75.

195.   Schenk T, Yurchuk E, Mueller S, Schroeder U, Starschich S, Böttger U, et al. About the deformation of ferroelectric hystereses. Applied Physics Reviews. 2014;1(4):041103.

196.   Evans JT. Characterizing ferroelectric materials. Proc IEEE ISAF. 2011:1-123.

197.   Pintilie L, Vrejoiu I, Hesse D, LeRhun G, Alexe M. Ferroelectric polarization-leakage current relation in high quality epitaxial Pb(Zr,Ti)O$_3$ films. Physical review B. 2007;75(10):104103.

198.   Stolichnov I, Tagantsev A, Setter N, Cross JS, Tsukada M. Control of leakage conduction of high-fatigue-endurance (Pb,La)(Zr,Ti)O$_3$ film ferroelectric capacitors with Pt/SrRuO$_3$ electrodes. Applied Physics Letters. 1999;75(12):1790-2.

199.   Saqib M, Khan SA, Rahman SA, Kim WY. Polarization Reversal Characteristics of Ferroelectric-Schottky Diode Hybrid Structure. Journal of nanoscience and nanotechnology. 2020;20(7):4303-6.

200.   Hatta I, Ikushima A. Temperature dependence of the heat capacity in BaTiO$_3$. Journal of the Physical Society of Japan. 1976;41(2):558-64.

201.   Hatta I, Ikushima AJ. Studies on phase transitions by AC calorimetry. Japanese Journal of Applied Physics. 1981;20(11):1995.

202.   Strukov BA, Davitadze ST, Kravchun SN, Taraskin SA, Goltzman M, Lemanov VV, et al. Specific heat and heat conductivity of BaTiO$_3$ polycrystalline films in the thickness range 20–1100 nm. Journal of Physics: Condensed Matter. 2003;15(25):4331-40.

203.   Sawai S, Tanaka H, Morimoto K, Hisano K, Yamamoto T. Simultaneous measurements of specific heat capacity and dielectric constant of ferroelectric Ba$_{1-x}$Sr$_x$TiO$_3$. Ferroelectrics. 2000;242(1):59-69.

204.   Shanon R. Revised effective ionic and systematic studies of interatomic distances in halides and chalcogenides. Acta Crystallogr A. 1976;32:751-67.

205.   Wang C, Cheng B, Wang S, Lu H, Zhou Y, Chen Z, et al. Effects of oxygen pressure on lattice parameter, orientation, surface morphology and deposition rate of (Ba$_{0.02}$Sr$_{0.98}$)TiO$_3$ thin films grown on MgO substrate by pulsed laser deposition. Thin solid films. 2005;485(1-2):82-9.

206.   Selvamani R, Singh G, Sathe V, Tiwari V, Gupta P. Dielectric, structural and Raman studies on (Na$_{0.5}$Bi$_{0.5}$TiO$_3$)$_{(1-x)}$(BiCrO$_3$)$_x$ ceramic. Journal of Physics: Condensed Matter. 2011;23(5):055901.

207.   Horwitz JS, Chang W, Kim W, Qadri SB, Pond JM, Kirchoefer SW, et al. The effect of stress on the microwave dielectric properties of Ba$_{0.5}$Sr$_{0.5}$TiO$_3$ thin films. Journal of electroceramics. 2000;4(2):357-63.

208.   Vashista M, Yusufzai MZK. Correlation between full width at half maximum (FWHM) of XRD peak with mechanical properties. International Journal of Metallurgy and Alloys. 2015;1(1):15-23.

209.   Gallegos-Melgar A, Espinosa-Arbelaez DG, Flores-Ruiz FJ, Lahmar A, Dellis JL, Lemée N, et al. Ferroelectric properties of manganese doped $(Bi_{1/2}Na_{1/2})TiO_3$ and $(Bi_{1/2}Na_{1/2})TiO_3$–$BaTiO_3$ epitaxial thin films. Applied Surface Science. 2015;359:923-30.

210.   Chen M, Xu Q, Kim BH, Ahn BK, Ko JH, Kang WJ, et al. Structure and electrical properties of $(Na_{0.5}Bi_{0.5})_{1-x}Ba_xTiO_3$ piezoelectric ceramics. Journal of the European Ceramic Society. 2008;28(4):843-9.

211.   Xu C, Lin D, Kwok KW. Structure, electrical properties and depolarization temperature of $(Bi_{0.5}Na_{0.5})TiO_3$–$BaTiO_3$ lead-free piezoelectric ceramics. Solid State Sciences. 2008;10(7):934-40.

212.   Jin C, Wang F, Leung CM, Tang Y, Wang T, Yao Q, et al. Growth and electric properties of (100)-oriented Mn-doped $(Bi_{0.5}Na_{0.5})TiO_3$-$BaTiO_3$ thin film by pulsed laser deposition. Applied Physics A. 2014;115(4):1375-9.

213.   Jin C, Wang F, Leung CM, Yao Q, Tang Y, Wang T, et al. Enhanced ferroelectric and piezoelectric response in Mn-doped $Bi_{0.5}Na_{0.5}TiO_3$–$BaTiO_3$ lead-free film by pulsed laser deposition. Applied Surface Science. 2013;283:348-51.

214.   Hejazi M, Taghaddos E, Safari A. Reduced leakage current and enhanced ferroelectric properties in Mn-doped $Bi_{0.5}Na_{0.5}TiO_3$-based thin films. Journal of Materials Science. 2013;48(9):3511-6.

215.   Wang DY, Chan NY, Li S, Choy SH, Tian HY, Chan HLW. Enhanced ferroelectric and piezoelectric properties in doped lead-free $(Bi_{0.5}Na_{0.5})_{0.94}Ba_{0.06}TiO_3$ thin films. Applied Physics Letters. 2010;97(21):212901.

216.   Sakamoto W, Makino N, Lee B-Y, Iijima T, Moriya M, Yogo T. Influence of volatile element composition and Mn doping on the electrical properties of lead-free piezoelectric $(Bi_{0.5}Na_{0.5})TiO_3$ thin films. Sensors and Actuators A: Physical. 2013;200:60-7.

217.   Hundt C. Bleifreie Perowskite für die Elektrokalorik: Bismut-Natrium-Titanat. Diploma. Technical University Dresden; 2019.

218.   Rémondière F, Wu A, Vilarinho PM, Mercurio JP. Piezoforce microscopy study of lead-free perovskite $Na_{0.5}Bi_{0.5}TiO_3$ thin films. Applied Physics Letters. 2007;90(15):152905.

219.   Engelhardt S, Molin C, Gebhardt S, Fähler S, Nielsch K, Hühne R. $BaZr_xTi_{1-x}O_3$ Epitaxial Thin Films for Electrocaloric Investigations. Energy Technology. 2018;6(8):1526-34.

220.   Fahey KP, Clemens BM, Wills LA. Nonorthogonal twinning in thin film oxide perovskites. Applied Physics Letters. 1995;67(17):2480-2.

112

221.   Choi J, Eom C-B, Rijnders G, Rogalla H, Blank DH. Growth mode transition from layer by layer to step flow during the growth of heteroepitaxial SrRuO$_3$ on (001) SrTiO$_3$. Applied physics letters. 2001;79(10):1447-9.

222.   Rijnders G, Blank DH, Choi J, Eom C-B. Enhanced surface diffusion through termination conversion during epitaxial SrRuO$_3$ growth. Applied physics letters. 2004;84(4):505-7.

223.   Zhu X, Meng Q, Yong L, He Y, Cheng B, Zheng D. Influence of oxygen pressure on the structural and dielectric properties of laser-ablated Ba$_{0.5}$Sr$_{0.5}$TiO$_3$ thin films epitaxially grown on (001) MgO for microwave phase shifters. Journal of Physics D: Applied Physics. 2006;39(10):2282.

224.   Chang C-Y, Wang R-L, Huang C-Y. Effects of Ba/Ti ratio on tetragonality, Curie temperature, and dielectric properties of solid-state-reacted BaTiO3 powder. Journal of Materials Research. 2012;27(23):2937-42.

225.   Zhou XY, Wang DY, He LX, Li Y, Wang Y, Chan HLW, et al. Influence of temperature on the in-plane dielectric properties of Barium Strontium Titanate thin films. Integrated Ferroelectrics. 2005;77(1):157-64.

226.   Zhang L, Zhong WL, Wang YG, Zhang PL. The cell volume effect in barium strontium titanate. Solid State Communications. 1997;104(5):263-6.

227.   Gatea HA, Naji IS. The effect of Ba/Sr ratio on the Curie temperature for ferroelectric barium strontium titanate ceramics. Journal of Advanced Dielectrics. 2020;10(05):2050021.

228.   Parker CB, Maria J-P, Kingon AI. Temperature and thickness dependent permittivity of (Ba,Sr)TiO$_3$ thin films. Applied Physics Letters. 2002;81(2):340-2.

229.   Koebernik G, Haessler W, Pantou R, Weiss F. Thickness dependence on the dielectric properties of BaTiO$_3$/SrTiO$_3$-multilayers. Thin Solid Films. 2004;449(1):80-5.

230.   Lookman A, Bowman RM, Gregg JM, Kut J, Rios S, Dawber M, et al. Thickness independence of true phase transition temperatures in barium strontium titanate films. Journal of Applied Physics. 2004;96(1):555-62.

231.   Vendik OG, Zubko SP. Ferroelectric phase transition and maximum dielectric permittivity of displacement type ferroelectrics (Ba$_x$Sr$_{1-x}$TiO$_3$). Journal of Applied Physics. 2000;88(9):5343-50.

232.   Ihlefeld JF, Harris DT, Keech R, Jones JL, Maria J-P, Trolier-McKinstry S. Scaling Effects in Perovskite Ferroelectrics: Fundamental Limits and Process-Structure-Property Relations. Journal of the American Ceramic Society. 2016;99(8):2537-57.

233.   Patil D, Lokare S, Devan R, Chougule S, Kanamadi C, Kolekar Y, et al. Studies on electrical and dielectric properties of Ba$_{1-x}$Sr$_x$TiO$_3$. Materials chemistry and physics. 2007;104(2-3):254-7.

234.   Li H-R, Chen C-X, Zheng R-K. Effects of Sr substitution on the structural, dielectric, ferroelectric, and piezoelectric properties of Ba(Zr,Ti)O$_3$ lead-free ceramics. Journal of Materials Science: Materials in Electronics. 2015;26(5):3057-63.

235.   Ban Z-G, Alpay SP. Phase diagrams and dielectric response of epitaxial barium strontium titanate films: A theoretical analysis. Journal of Applied Physics. 2002;91(11):9288-96.

236.   Peräntie J, Correia T, Hagberg J, Uusimäki A. Electrocaloric Effect in Relaxor Ferroelectric-Based Materials. In: Correia T, Zhang Q, editors. Electrocaloric Materials: New Generation of Coolers. Berlin, Heidelberg: Springer Berlin Heidelberg; 2014. p. 47-89. 978-3-642-40264-7

237.   Akcay G, Alpay SP, Mantese JV, Jr. GAR. Magnitude of the intrinsic electrocaloric effect in ferroelectric perovskite thin films at high electric fields. Applied Physics Letters. 2007;90(25):252909.

238.   Akcay G, Alpay SP, Jr. GAR, Scott JF. Influence of mechanical boundary conditions on the electrocaloric properties of ferroelectric thin films. Journal of Applied Physics. 2008;103(2):024104.

239.   Wang L, Wang J, Li B, Zhong X, Wang F, Song H, et al. Enhanced room-temperature electrocaloric effect in barium titanate thin films with diffuse phase transition. RSC Advances. 2014;4(42):21826-9.

List of Publications:

- Magalhaes B, Engelhardt S, Molin C, Gebhardt SE, Nielsch K, Hühne R. Electrocaloric temperature changes in epitaxial $Ba_{1-x}Sr_xTiO_3$ films. Journal of Alloys and Compounds. 2022;891:162041.

- Magalhaes B, Engelhardt S, Molin C, Gebhardt SE, Nielsch K, Hühne R. Structural and Electric Properties of Epitaxial $Na_{0.5}Bi_{0.5}TiO_3$-Based Thin Films. Coatings. 2021;11(6):651.

- Martins PM, Ferreira C, Silva A, Magalhães B, Alves MM, Pereira L, et al. TiO_2/graphene and TiO_2/graphene oxide nanocomposites for photocatalytic applications: A computer modeling and experimental study. Composites Part B: Engineering. 2018;145:39-46.

- Teixeira S, Magalhães B, Martins PM, Kühn K, Soler L, Lanceros Méndez S, et al. Reusable Photocatalytic Optical Fibers for Underground, Deep-Sea, and Turbid Water Remediation. Global Challenges. 2018;2(3):1700124.

- Dias J, Lopes A, Magalhães B, Botelho G, Silva MM, Esperança J, et al. High performance electromechanical actuators based on ionic liquid/poly (vinylidene fluoride). Polymer Testing. 2015;48:199-205.

Statement of authorship

I hereby certify that I have authored the following dissertation:

Lead-free oxide epitaxial layers for electrocaloric studies

without unauthorized assistance from third parties and without using anything other than the indicated

Ideas derived directly or indirectly from outside sources are labeled as such. Dr. Ruben Hühne assisted me in the selection and evaluation of the material, as well as in the preparation of the text. There were no other people engaged in the current work's intellectual development. I did not, for example, seek the services of a commercial doctoral advisor. I have not received any monetary compensation from third parties for activities relating to the content of the dissertation.

This dissertation has not been submitted to any other examination authority, either in English, German, or any other language, in the same or comparable form, nor has it been published. The doctorate regulations of the Technische Universität Dresden, Faculty of Mechanical Engineering are recognized.

Dresden, 31 of May 2022

_____

Bruno Martins Magalhães

Acknowledgments